Experimentally informed *in silico* design of 3D-printed Calcium Phosphate scaffolds for dental bone regeneration

Bingbing Liang

Thesis submitted in partial fulfilment of the
requirements for the degree of Doctor of Philosophy
(PhD) in Engineering Science

September 2024

Doctoral College of Aerospace and Mechanical Engineering

Faculty of Applied Sciences

Experimentally informed *in silico* design of 3D-printed Calcium Phosphate scaffolds for dental bone regeneration

Bingbing Liang

Supervisor: Prof. Dr. Ir. Liesbet Geris

Jury Members:

Prof. Dr. Ir. D. Ruffoni, Université de Liège - President

Prof. Dr. F. Lambert, Université de Liège

Prof. Dr. Ir. G. Kerckhofs, UC Louvain

Prof. Dr. Ir. P. Wieringa, Maastricht University (The Netherlands)

Nature does not hurry,
yet everything is accomplished

Lao Tzu

Acknowledgements

I would like to begin by expressing my heartfelt gratitude to everyone who has supported me throughout the course of this research. This journey would not have been possible without the invaluable contributions and encouragement of many individuals.

I would like to express my deepest gratitude and profound appreciation to Prof. Liesbet Geris for granting me the opportunity to embark on this extraordinary journey of discovery and learning. The opportunity of working under your mentorship has been one of the most significant and transformative experiences of my life, both academically and personally. From the very beginning, your unwavering support, insightful guidance, and continuous encouragement have shaped my journey through this PhD in ways I could have never imagined. Your mentorship extended beyond the confines of research and academia. You have been a role model in balancing the demands of a successful professional career with the compassion and understanding needed to nurture and support your students. Your patience, kindness, and willingness to listen, even during challenging times (like global pandemic), have been a source of comfort and strength. I am deeply grateful for the life lessons you have imparted, which have not only helped me grow as a researcher but also as an individual. Thank you, Lies, for believing in me, and for challenging me to push my boundaries. Your impact on my life and career is immeasurable, and I will carry the lessons learned under your guidance with me always.

I would like to express my sincere gratitude and grateful to my jury members. Prof. France Lambert, thanks so much for your guidance and

contribution to this project. I am grateful for the opportunity to work alongside you throughout this research work. Prof. Davide Ruffoni, Prof. Greet Kerckhofs and Prof. Paul Wieringa, thank you for taking the time to carefully read through my thesis, offering valuable comments and suggestions that have greatly contributed to the refinement and completion of this work. Your expertise and perspectives have not only enriched my research but have also pushed me to consider new angles and approaches.

I would like to express my heartfelt gratitude to colleges and friends in ULiege and KU Leuven. Varun, you were the first person I met when I started. I am grateful for the help and friendship you offered me from the very beginning. You not only helped me adapt to my new life in Belgium, but also generously introduced me to your circle of friends. Little did we know that one of those friends, Adrien, would later become my husband. Ehsan, we started work together in GIGA institute, and you always provide friendly collaboration and interesting conversation. It has been a true pleasure working with you and being friend with you. Mojtaba, you always gave me the invaluable support throughout my academic journey. I appreciate your patience and professionalism in addressing my questions. I always looked forward to our regular meetings and lunch breaks at KU Leuven, which were truly enjoyable. Sophie, I enjoyed our conversations – you were always full of positive energy and never hesitated to lend a helping hand. Remember that "super computer"? I am so glad we had the chance to become friends. Your cooking skills are amazing, and les boulets liegeois you taught me to make were absolutely delicious. Marc, you taught me so much about French and Belgian culture, and even introduced me to your daughters. Honestly, you are one of the coolest PhD students I have ever met. I am also extremely happy to know all the colleagues in ULiège and KULeuven especially Bernard, Morgan, Satanic, Fernando, Tim, Niki, Raphaelle, Laura and Dorien for being really great friends.

instrumental. I am truly grateful to be part of such a supportive and dedicated team.

I would also like to extend my heartfelt thanks to my new friends in Ireland, Mariangela, Kulwinder, Shan, Rocha, Meric, Paige, Martin, Ding, Liang, Eric, Pablo, Valentina, Baruch, Micklen, your companionship made my transition to this new environment so much smoother, and the friendships we have developed have truly enriched my experience. It is because of you that Dublin has become such a vibrant and appealing city to me.

At last, I would like to extend my deepest gratitude to my husband, Adrien, your support has been a cornerstone throughout this journey. Your unwavering patience, encouragement, and belief in me have been a constant source of strength. Even more fortunate, it's not just you—your entire family has also shown me the same level of care and support. Many times during this process, I found myself overwhelmed with anxiety, and it was your keen ability to sense my distress and your thoughtful efforts to ease my worries that helped me persevere. You have not only been a steadfast partner but also my greatest cheerleader, always reminding me to trust in myself and keep moving forward. Your role in my life extends far beyond that of a husband; you are my best friend, my confidant, and my soulmate. Your love and support have made this challenging journey not only manageable but also deeply meaningful. I am profoundly grateful for your presence and everything you has done to help me achieve this milestone.

Abstract

Though the natural process of bone regeneration is able to scarlessly repair the vast majority of bone defects, a number of cases require intervention. Bone tissue engineering combines principles of engineering and biomedical sciences in order to create living implants to treat large and non-healing bone defects. This thesis begins by outlining the fundamentals of the human skeleton, encompassing its composition, structure, and function. It then delves into the mechanisms of bone formation and regeneration, alongside the development and application of bone tissue engineering. The introductory chapter also reviews the experimental and mathematical models used in this research domain.

Next, the two primary assumptions guiding the doctoral project are put forth. The first objective is to validate the curvature-driven neotissue growth model on calcium phosphate scaffold materials through *in vitro* experiments, thus assessing the model's versatility across various conditions. The second objective is to refine the model to enhance scaffold design for alveolar bone regeneration. This involves adjusting the scaffold's gradient structure and initial cell concentration to better simulate cell growth within the scaffold, aiming to make the model more applicable in clinical scenarios.

The first study of this doctoral research employed a combined experimental and modelling approach to assess and apply a curvature-driven model of regenerative cell and tissue growth. This model is designed to simulate neotissue growth on three-dimensional scaffolds by tracking curvature changes. Model parameters were derived from a mix of *in vitro* experiments on custom-designed printed disks and literature

references. Bayesian optimization was used to align experimental results with model predictions. An application on a 3D porous structure confirmed the predictive potential of the model.

Building on these results, the next study applied the developed model to design a 3D scaffold for bone regeneration in a maxillofacial animal model. The design aims to optimize neotissue growth, balancing rapid growth with sufficient living tissue within the scaffold to support the placement of a dental implant. The design's feasibility was constrained by manufacturing precision and practicality. The chosen scaffold design was implanted, and biological outcomes were assessed at 4 and 8 weeks. Comparisons with the clinical gold standard and a lattice design revealed the superiority of the gyroid design, evidenced by a greater volume of bone formation and deeper bone penetration within the scaffold.

The final study aimed to address the model-related challenges observed in the previous study. Additional Triply Periodic Minimal Surface (TPMS) and lattice structures were analysed to assess neotissue growth. It also explored different initial cell layer configurations to evaluate the model's ability to replicate *in vivo* neotissue ingrowth when scaffolds are implanted without a layer of pre-seeded cells. The investigation showed that gradient structures in the scaffold design have minimal impact on neotissue growth rates. These findings underscore several routes for improvement of the current modelling framework, particularly in simulating *in vivo* conditions or non-TPMS structures.

Overall, the thesis advances the understanding of neotissue growth modelling on 3D scaffolds, providing insights into scaffold design optimization for bone regeneration. The research underscores the potential and limitations of the curvature-driven model and sets the stage for further refinement and application in clinical settings.

Résumé

Bien que le processus naturel de régénération osseuse soit capable de réparer sans cicatrices la grande majorité des défauts osseux, certains cas nécessitent une intervention. L'ingénierie tissulaire osseuse combine les principes de l'ingénierie et des sciences biomédicales pour créer des implants vivants afin de traiter les grands défauts osseux et les défauts non cicatrisants. Cette thèse commence par exposer les fondamentaux du squelette humain, incluant sa composition, sa structure et ses fonctions. Elle explore ensuite les mécanismes de formation et de régénération osseuses, ainsi que le développement et l'application de l'ingénierie tissulaire osseuse. Le chapitre introductif passe également en revue les modèles expérimentaux et mathématiques utilisés dans ce domaine de recherche.

Ensuite, les deux principales hypothèses qui guident ce projet doctoral sont présentées. Le premier objectif est de valider le modèle de croissance néotissulaire basé sur la courbure sur des matériaux de support en phosphate de calcium à travers des expériences *in vitro*, afin d'évaluer la polyvalence du modèle dans diverses conditions. Le deuxième objectif est de perfectionner le modèle pour améliorer la conception des supports pour la régénération osseuse alvéolaire. Cela implique d'ajuster la structure en gradient du support et la concentration initiale de cellules pour mieux simuler la croissance cellulaire à l'intérieur du support, dans le but de rendre le modèle plus applicable en milieu clinique.

La première étude de cette recherche doctorale a employé une approche combinée expérimentale et modélisation pour évaluer et appliquer un

modèle de croissance cellulaire et tissulaire régénérative basé sur la courbure. Ce modèle est conçu pour simuler la croissance néotissulaire sur des échafaudages tridimensionnels en suivant les changements de courbure. Les paramètres du modèle ont été dérivés d'une combinaison d'expériences *in vitro* sur des disques imprimés sur mesure et de références littéraires. L'optimisation bayésienne a été utilisée pour aligner les résultats expérimentaux avec les prédictions du modèle. Une application sur une structure poreuse 3D a confirmé le potentiel prédictif du modèle.

Sur la base de ces résultats, l'étude suivante a appliqué le modèle développé pour concevoir un échafaudage 3D pour la régénération osseuse dans un modèle animal maxillo-facial. La conception vise à optimiser la croissance néotissulaire, en équilibrant la croissance rapide avec suffisamment de tissu vivant à l'intérieur de l'échafaudage pour soutenir la mise en place d'un implant dentaire. La faisabilité de la conception était limitée par la précision et la praticabilité de la fabrication. Le design d'échafaudage choisi a été implanté, et les résultats biologiques ont été évalués à 4 et 8 semaines. Les comparaisons avec la norme clinique et une conception en treillis ont révélé la supériorité de la conception gyroidale, comme en témoignent un volume de formation osseuse plus important et une pénétration osseuse plus profonde dans l'échafaudage.

La dernière étude visait à aborder les défis liés au modèle observés dans l'étude précédente. Des structures supplémentaires de type «Triply Periodic Minimal Surface (TPMS) » et en treillis ont été analysées pour évaluer la croissance néotissulaire. Elle a également exploré différentes configurations de couches cellulaires initiales pour évaluer la capacité du modèle à reproduire l'ingrowth néotissulaire *in vivo* lorsque les échafaudages sont implantés sans couche de cellules pré-ensemencées. L'enquête a montré que les structures en gradient dans la conception de l'échafaudage ont un impact minimal sur les taux de croissance néotissulaire. Ces résultats soulignent plusieurs pistes d'amélioration du

cadre de modélisation actuel, en particulier dans la simulation des conditions *in vivo* ou des structures non TPMS.

Dans l'ensemble, la thèse fait progresser la compréhension de la modélisation de la croissance néotissulaire sur des échafaudages 3D, fournissant des insights pour l'optimisation de la conception des échafaudages pour la régénération osseuse. La recherche souligne le potentiel et les limites du modèle basé sur la courbure et prépare le terrain pour un affinage et une application ultérieurs en milieu clinique.

x

Table of contents

List of abbreviations

2D	two-dimensional
3D	three-dimensional
3Rs	reduce, refine and replace
aFGF	acidic fibroblast growth factor
ALP	alkaline phosphatase
AM	Additive manufacturing / additively manufactured
AMTs	additive manufacturing technologies
ASLI	A Simple Lattice Infiller
ASME	American society of mechanical engineers
AV	available volume
BC	boundary condition
BCP	biphasic calcium phosphates
BET	bromodomain and extra-terminal domain
bFGF	basic fibroblast growth factor
BMC	bone to material contact
BMP	bone morphogenetic protein
CaPs/CaP	calcium phosphate
CT	Computed tomography
CTAn	CT-Analyser
DAPI	4',6-diamidino-2-phenylindole
ECM	extracellular matrix
EDTA	ethylenediaminetetraacetic acid
FBS	fetal bovine serum
FDA	food and drug administration
FEG-SEM	field emission gun – scanning electron microscope
FRD/F-RD	förstner random dots
Gla	gamma-carboxyglutamic acid
GM	growth medium

HA/HAp	hydroxyapatite
HRP	horseradish peroxidase
hTERT-BMMSCs	human telomerase reverse transcriptase-immortalized bone marrow mesenchymal stem cells
hTERT-BMSCs	human telomerase reverse transcriptase - immortalized bone mesenchymal stromal cells
IGF	insulin-like growth factor
IWP/I-WP	isotropic woodpile
LSM	level set method
MDR	medical device regulation
MG-63	MG-63 human osteosarcoma cells
MPI	Message Passing Interface
MSCs	mesenchymal stem cells
MUMPS	MUltifrontal massively parallel Sparse direct Solver
NV	new tissue volume
ODE	ordinary differential equation
PBS	phosphate-buffered saline
PDE	partial differential equation
PDGF	platelet-derived growth factor
REML	mixed-effect model
SD	standard deviation
SEM	scanning electron microscope
SLA	stereolithograhy
SMBO	sequential model-based optimization
TCP	tricalcium phosphate
TE	tissue engineering
TGF	transforming growth factor
TGF-β	transforming growth factor beta
TPMs/TPMS	triply periodic minimal surface
UV	ultraviolet radiation
VOI1	the total volume inside the shells
VOI2	the empty volume inside the shells
VVUQ	verification, validation, and uncertainty quantification
β-TCP	β-tricalcium phosphate

List of symbols

∇	$\dfrac{\partial i}{\partial x} + \dfrac{\partial j}{\partial y} + \dfrac{\partial k}{\partial z}$
Γ	scaffold interface
η	viscosity of PBS
Ω	computational domain
Ω_{nt}	neotissue domain
Ω_v	void space domain
φ	level set function
ε	strain
V_G	interface moving with the growth velocity
κ	local mean curvature

List of figures

List of tables

CHAPTER 1

General introduction

Bone is a crucial organ that forms the human inner skeleton, providing structural support, facilitating movement, protecting vital organs, and storing minerals. As a dynamic material, bone can adapt to changing biomechanical environments and achieve scarless healing. The bone healing process comprises three stages: inflammation, bone formation, and bone remodelling. In cases of severe trauma, tumours, bone infections, and congenital bone diseases, tissue engineering (TE) offers effective solutions for repairing bone defects. The three fundamental components of TE are scaffolds, cells, and growth factors. Scaffolds serve as supportive structures for bone defects, promoting cell attachment and growth. Advances in porous design and 3D printing have enabled the development of scaffolds that enhance cell proliferation. Consequently, the structural design of scaffolds and computer simulations of cell growth are pivotal in TE for bone regeneration.

In the following chapter, we will explore the composition, structure, and function of human bones, followed by a discussion on bone formation and regeneration. Subsequently, we will review the development, application, and influencing factors in bone tissue engineering. The final sections will cover experimental and mathematical modelling methods utilized in this field of research.

1.1 Bone

Bone tissue is a dense connective tissue formed by the hardening of the matrix that encapsulates cells. When osteoblasts are trapped by the extracellular matrix (ECM) they produced, they become osteocytes. Bones come in various shapes and possess intricate internal and external structures that minimize weight while maintaining strength. Bone components include mineralized bone tissue, bone marrow, periosteum, nerves, blood vessels, and cartilage. Bone tissue consists of cells and an extracellular matrix with embedded fibres. Unlike other connective tissues, the extracellular matrix of bone is calcified (Wilk-Blaszczak, 2018).

1.1.1 Composition, structure and function

Bone is composed of living cells embedded in a mineralized organic matrix, including osteoblasts and osteocytes. Bones are about 60% inorganic (hydroxyapatite, citrate, mineral salts of calcium and phosphate), 25% organic (mainly collagen types I and II, non-collagenous proteins, ground substance, BMP), and 15% water. The primary inorganic component of human bones is hydroxyapatite ($Ca_{10}(PO_4)_6(OH)_2$). The organic matrix is predominantly collagen, providing elasticity and contributing to the biomechanical properties of bone. Bone collagen includes intrinsic collagen secreted by osteoblasts and extrinsic collagen formed by adjacent fibroblasts. The main non-collagenous proteins, such as proteoglycans, glycoproteins, and bone gla-containing proteins, play roles in mineralization. Gla-containing proteins are proteins that have gamma-carboxyglutamic acid (Gla) residues, which are formed through vitamin K-dependent modification. These proteins are crucial for processes such as bone mineralization and blood coagulation, as the Gla residues enable them to bind calcium ions. A healthy bone structure requires strength in both tensile and compressive, achieved through the synergy of collagen fibres and elongated hydroxyapatite crystals. Nutritional and mineralization changes can alter the matrix composition over time. The calcium to phosphate ratio ranges from 1.3 to 2.0 by weight, with

variations in trace minerals like magnesium, sodium, potassium, and carbonate (Aerssens et al., 1998).

Bones are classified by histology (compact and spongy bone), development (endochondral and intramembranous bone), and shape (long, short, flat, and irregular bones). For example, long bones consist of diaphysis and epiphysis. The diaphysis is a hollow tubular shaft with a dense and hard outer wall, including cortex and cortical bone, filled with yellow bone marrow in adults. The epiphysis, the bone's bulging part, is filled with spongy bone and red bone marrow (Figure 1.1).
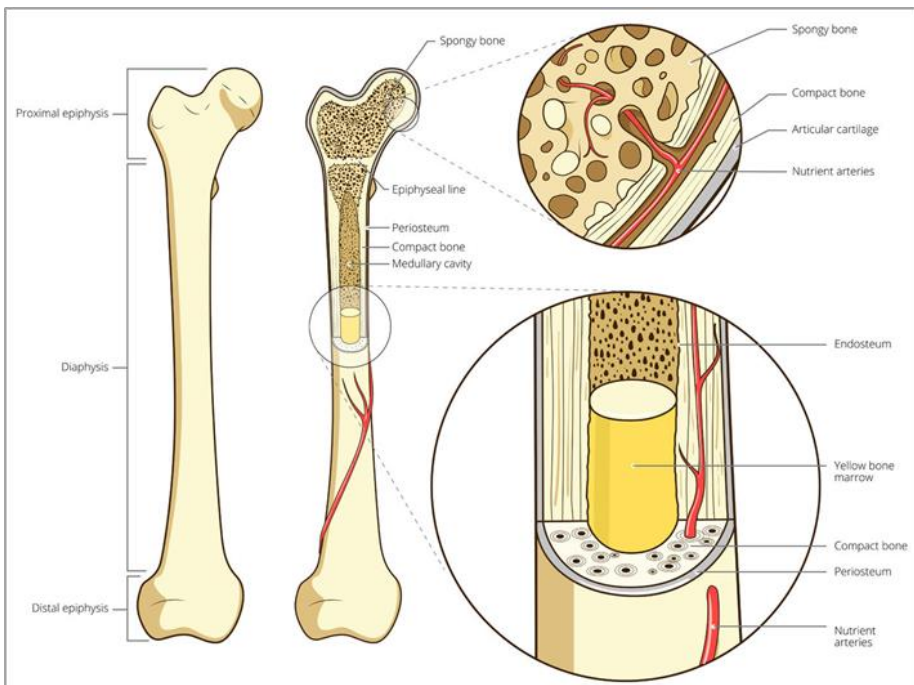
Figure 1.1: Long bone structure (Peate, 2018). The diagram shows the anatomy of a long bone, including the proximal and distal epiphysis, diaphysis, periosteum, compact bone, and medullary cavity. The upper magnified section details the spongy bone, characterized by its porous structure filled with red bone marrow. The lower magnified section reveals the yellow bone marrow within the medullary cavity, along with the endosteum and compact bone. The diagram also highlights the nutrient arteries that penetrate the periosteum to supply the bone with nutrients.

During growth, the metaphysis includes the growth plate, which becomes the epiphyseal line when bones stop growing. The endosteum, a type of bone cell, facilitates bone growth, repair and remodelling, and is located inside the bone near the medullary cavity. The periosteum, a double-layered fibrous structure, contains cells that also contribute to bone growth, repair and remodelling. The periosteum covers the cortical bone, except at joints, which are covered by articular cartilage to reduce friction and absorb shocks. Bones constantly renew to maintain and remodel cells. Osteoblasts, osteoclasts, and osteocytes are the most active cells in this process. Osteoblasts facilitate osteogenesis, including new bone growth and bone repair, through the production of a mixture of proteins called osteoid that mineralize into bone. Osteocytes, which are matured osteoblasts buried inside the bone matrix, act as mechanosensors and information transmitters between bone cells. Osteoclasts, large multinucleated cells, dissolve minerals in damaged bone areas, allowing osteoblasts to rebuild the bone. (Bilezikian et al., 2008).

Bone functions include:

1. Structural support and protection of soft tissues.

2. Mechanical support for movement.

3. Blood formation through bone marrow.

4. Mineral storage, primarily calcium and phosphate (Robey et al., 2008).

1.1.2   Alveolar bone

The alveolar bone is a specialized part of the maxilla and mandible that supports teeth. It includes the proper alveolar bone (lamellar and fascicular bone) and supporting alveolar bone (cortical plate and spongy bone). Alveolar bone comprises 67% inorganic matter (mainly calcium hydroxyapatite) and 33% organic matter (collagen and non-collagen materials). Osteoblasts and osteoclasts are the primary cells in alveolar bone. Development starts from the dental follicle, where mesenchymal

cells differentiate into osteoblasts, depositing osteoid and embedding osteoblasts in the matrix (Bath-Balogh et al., 2014).

Alveolar bone functions include:

- Protection: forms an alveolus to protect teeth; disappears if the tooth is lost.
- Attachment: attached to periodontal ligament fibres.
- Support: supports tooth roots.
- Shock absorption: distributes force exerted on teeth to underlying tissues, helping absorb external forces (Melsen et al., 1999).

Alveolar bone loss can result from periodontal disease (periodontitis, osteomyelitis, tumour), trauma, or aging (physiological degeneration of periodontal tissue, lost teeth). As this loss might surpass the natural healing capacity of the bone, successful bone regeneration will require the implantation of autologous bone, allogeneic bone or a tissue engineered implant (Urban et al., 2019).
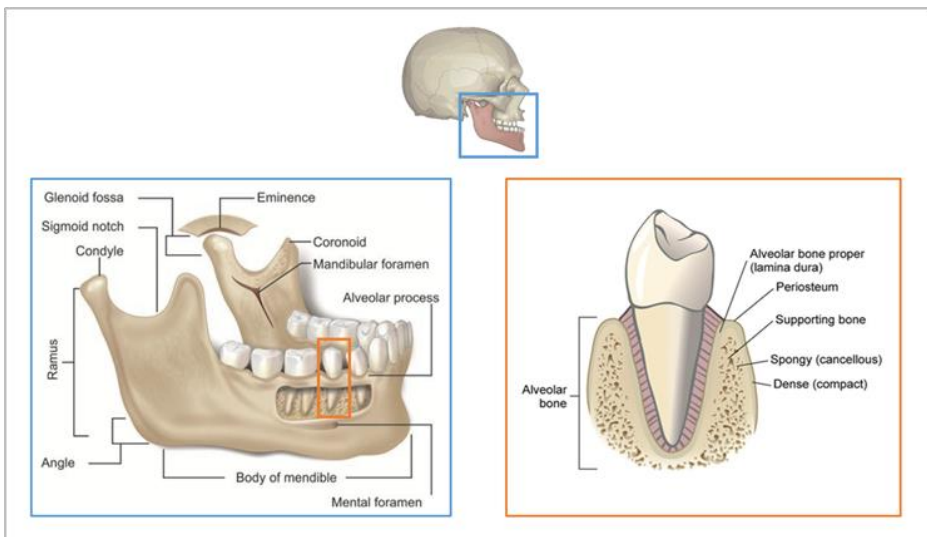
Figure 1.2: Schematic representation of alveolar bone (Malik et al., 2016). The diagram illustrates the anatomy of the mandible and alveolar bone. On the left, a detailed view of the mandible highlights key structures, including the ramus, condyle, coronoid process, alveolar process, and mental foramen. The upper inset shows the mandible's position within the skull. On the right, a close-up of the

alveolar bone and tooth structure is provided, showing the alveolar bone proper (lamina dura), periosteum, supporting bone, spongy (cancellous) bone, and dense (compact) bone. This diagram emphasizes the relationship between the jawbone and the dental structures it supports.

1.2   Bone formation

Bone formation, also known as osteogenesis and ossification, involves replacing mesenchymal tissue with bone (Akter et al., 2016). Differentiated cells in the osteoblast lineage undergo three stages: proliferation, matrix maturation, and mineralization. Initially, woven bone composed of randomly oriented collagen fibres forms. This immature bone gradually matures into lamellar bone through remodelling processes (Ozasa et al., 2018). Bone formation can be categorized into two main processes: intramembranous and endochondral ossification. Mesenchymal stem cells (MSCs) play a vital role in these processes (Dennis et al., 2015).

In intramembranous ossification, MSCs directly differentiate into osteoblasts, which then secrete non-mineralised bone extracellular matrix (ECM), mineralise the matrix, and eventually become embedded in it as osteocytes. In endochondral ossification, MSCs initially coagulate and differentiate into chondrocytes, secreting a cartilage matrix. Once mature, hypertrophic chondrocytes secrete factors mineralising their matrix and attracting blood vessels. The latter facilitate the migration of MSCs that differentiate into osteoblasts and replace the cartilaginous matrix with bone (Setiawati et al., 2019).

1.2.1   Bone development

The flat bones of the body and the face as well as the jaw (alveolar bone), most of the skull and the clavicles form through intramembranous ossification. Dense spongy bone develops directly within mesenchymal connective tissue. As shown in Figure 1.3, this process involves several steps. Initially, mesenchymal cells in the bone aggregate and differentiate

into osteoblasts. Osteoblasts then secrete an osteoid matrix that calcifies within a few days/weeks due to mineral salt deposition, trapping the osteoblasts and transforming them into bone cells.
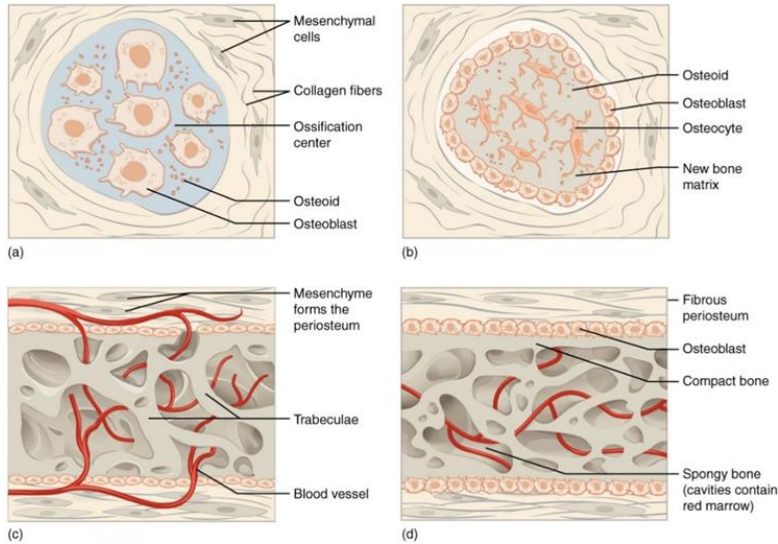
Figure 1.3: The stages of intramembranous ossification. This diagram illustrates the stages of intramembranous ossification, the process by which flat bones, such as those of the skull, are formed. (a) shows the initial stage where mesenchymal cells cluster and differentiate into osteoblasts, forming an ossification center. The osteoblasts secrete osteoid, which is the unmineralized bone matrix, and begin laying down collagen fibers. (b) depicts the osteoid surrounding the osteoblasts, which become trapped and mature into osteocytes. This stage shows the formation of new bone matrix around the ossification center. (c) demonstrates the development of trabeculae as the ossification centers expand. The mesenchyme on the surface forms the periosteum, while blood vessels begin to infiltrate the forming bone. (d) shows the final stage where the trabeculae near the periosteum thicken to form compact bone, while the trabeculae in the center remain spongy bone, with cavities that will eventually contain red marrow. The fibrous periosteum and the continuous activity of osteoblasts ensure the bone's growth and development.

Concurrently, osteoblasts in connective tissue continue to differentiate. The formation of trabecular matrix and periosteum follows, with the

unmineralized osteoid matrix gradually mineralising and reorganising into trabecular bone (Tortora et al., 2018).

Endochondral ossification involves the development of bones from hyaline cartilage, which serves as a template that is replicated and replaced by bone tissue. This process is essential for the formation of long bones and generally takes longer than intramembranous ossification. As shown in Figure 1.4, the stages of endochondral ossification are the following.

1. Mesenchymal cells differentiate into chondrocytes, forming a cartilage anlagen covered by the perichondrium.
2. Chondrocytes continue to grow and divide, sustained by the matrix's nutrient supply. Upon further maturation, chondrocytes become hypertrophic and calcify the cartilaginous matrix. The hypertrophic cells enter an apoptotic program, secreting matrix degrading enzymes and vascular growth factors, attracting blood vessels.
3. Blood vessels eventually invade the calcified area, creating a medullary cavity. The formation of primary ossification centres follows, where MSCs that came along with the blood vessels, forms bone.
4. This process is repeated on the epiphyseal sides, creating secondary ossification centres.
5. Bone gradually replaces the cartilage in these ossification centres, with the exception of the growth plate where chondrocytes continue to proliferate. Growth plates are the motor of longitudinal bone growth postnatally.
6. Upon reaching puberty, the growth plates gradually close, resulting in the formation of an epiphyseal line, indicating the completion of bone development.
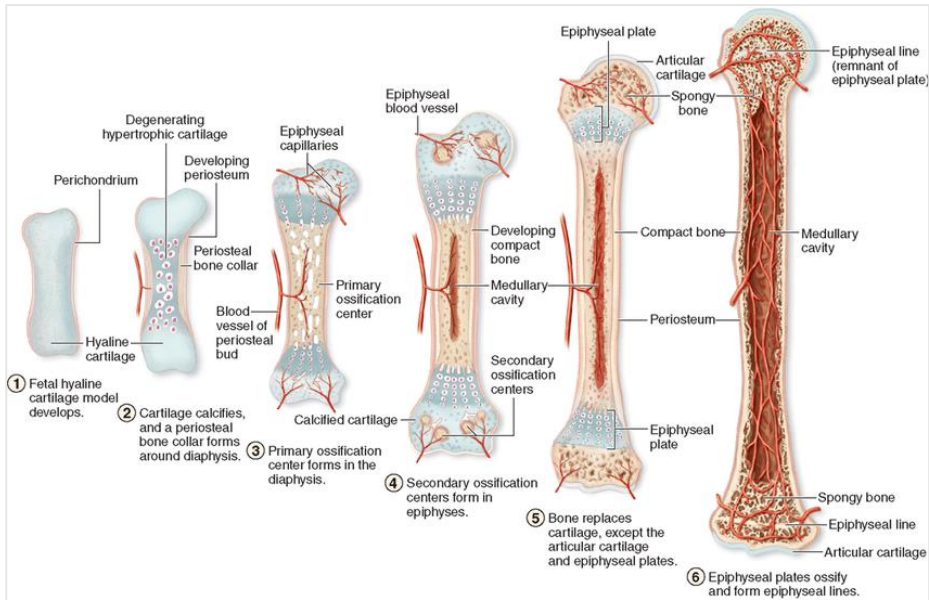
Figure 1.4: The stages of endochondral bone formation during development. 1. The initial stage of endochondral ossification starts with the formation of a hyaline cartilage template. 2. The cartilage in the center of the diaphysis begins to calcify, and a periosteal bone collar forms around the diaphysis as the perichondrium develops into the periosteum. 3. Blood vessels invade the internal cavities, leading to the formation of primary ossification centers in the diaphysis, where bone tissue begins to replace cartilage. 4. Ossification extends to the epiphyses, forming secondary ossification centers, while the medullary cavity develops in the center of the bone. 5. Most of the cartilage is replaced by bone tissue, leaving articular cartilage on the joint surfaces and epiphyseal plates for continued growth. 6. Finally, the growth in length ceases when the epiphyseal plates ossify and form epiphyseal lines, signifying the end of the bone's growth in length. (https://www.slideshare.net/MohiuddinMasum1/ossification-intracartilaginous-and-intramembranous, accessed: 17 May 2024)

1.2.2 Bone regeneration

Long bone healing after fracture generally follows the secondary healing route (endochondral ossification), unless compression plates are used to press the bone ends to one another. In that case, bone regeneration will

occur through primary healing (bone remodelling). The bone regeneration process takes 2-3 months. Below, the four stages of secondary bone healing are discussed, as shown in Figure 1.5:

1. Hematoma Formation: Local extravascular haemorrhage caused by disease or trauma (including injury or surgery) results in a hematoma. The patient will feel severe pain accompanied by inflammation and swelling of the fracture site. Inflammatory cytokines will influence the migration of mesenchymal stem cells and the secretion of growth factors (such as TGF-B, PDGF, BMP).

2. Fibrocartilaginous Callus Formation: Within a few days after the fracture, some soft callus and granulation tissue form, aided by capillaries growing in it. Phagocytes digest injured cells in the area, speeding up callus tissue formation. Due to the combination of lack of oxygen/nutrients with secretion of specific growth factors, cells differentiate into chondrocytes laying down a fibrocartilaginous matrix.

3. Bony Callus Formation: During this period (usually 3 weeks to 3 months after injury), chondrocytes mature into hypertrophic chondrocytes, initialising the endochondral ossification process described above. Newly formed woven bone gradually replaces the cartilage template, which is called the bony callus.

4. Bone Remodelling: woven bone is gradually removed by osteoclasts, who are immediately followed by osteoblasts laying down lamellar bone. This remodelling process allows recovering the medullary canal and original shape the bone had prior to the fracture.
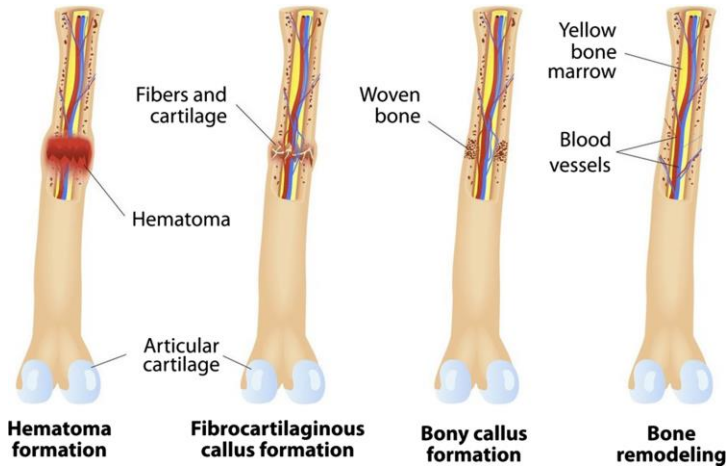
Figure 1.5: Bone regeneration. This image illustrates the process of bone fracture healing. Initially, a hematoma forms at the fracture site due to ruptured blood vessels. As healing progresses, the hematoma is replaced by a fibrocartilaginous callus made of fibrous tissue and cartilage, which helps stabilize the fracture. This callus is then replaced by woven bone, forming a bony callus that starts to rebuild the bone structure. Eventually, the bony callus undergoes remodelling, transforming into mature bone, with the marrow cavity and blood vessels being largely restored to their original state. ((Ansari et al., 2019), accessed: 17 July 2024)

Alveolar bone regeneration and long bone regeneration share several biological mechanisms, but they also exhibit significant differences in their mechanical environment, vascularization, and specific regenerative objectives.

__Similarities__ - Alveolar and long bone regeneration rely on similar basic biological processes. The cellular and molecular mechanisms involved in both regeneration processes include bone resorption (removal of damaged or excess bone tissue) and bone formation. The regeneration of both types of bone depends on the activity of osteoblasts, which are responsible for forming and repairing bone tissue. .Growth factors, such as bone morphogenetic protein (BMP) and transforming growth factor-beta (TGF-β), play critical regulatory roles in both long bone and alveolar bone regeneration (Son et al., 2020). These growth factors stimulate the

differentiation and proliferation of osteoblasts, thereby promoting the repair and regeneration of bone tissue (Ansari et al., 2019).

Differences - Despite these similarities, there are notable differences in the mechanical environments and specific requirements for regeneration between long bones and alveolar bones.

- **Mechanical Environment**: Long bone regeneration must account for the bone's load-bearing function, especially in the lower extremities, where the regenerated bone must withstand body weight and the mechanical loads of daily activities (Son et al., 2020). Thus, the regeneration of long bones requires not only the formation of new bone tissue but also the restoration of bone strength and durability to ensure structural integrity under mechanical stress. In contrast, alveolar bone regeneration typically (but not always) occurs in a low mechanical load environment (Son et al., 2020; Cho et al., 2000). As a result, alveolar bone regeneration focuses more on promoting rapid healing in the absence of significant mechanical stress, which is crucial for restoring oral function quickly.

- **Blood Supply**: The difference in blood supply between long bones and alveolar bones is another important distinction. Long bones have a relatively rich blood supply, which is crucial for the healing and regeneration of bone tissue. Adequate blood flow provides the necessary oxygen, nutrients, and growth factors to support osteoblast activity and the formation of new bone. In contrast, alveolar bones have a more limited blood supply (Cho et al., 2000), especially following tooth extraction or injury, where the blood flow to the alveolar bone region may decrease (An et al., 2017). This limited blood supply can impact the regeneration process, potentially slowing down healing compared to long bones (An et al., 2017).

- **Regenerative Focus and Goals**: The regenerative focus and objectives of interventions and therapies also differ between long bone and alveolar bone regeneration. Interventions in long bone

regeneration prioritize the structural strength and durability of the bone, ensuring that the regenerated bone has sufficient mechanical strength to withstand various stresses encountered in daily life (Lasanianos et al., 2010). On the other hand, alveolar bone regeneration interventions focus on rapid healing to restore the supportive structure for teeth while also considering aesthetic outcomes, which is vital for subsequent dental restoration or implant procedures (Sheikh et al., 2017).

1.3   Bone tissue engineering

Healing of large bone defects caused by congenital bone dysplasia, severe trauma, organ infection, tumour resection, and metabolic diseases have always been a huge clinical challenge. In 5-10% of all fractures and bone defects, the regeneration process is inadequate leading to delayed or non-unions (Stewart et al., 2019). For intraoral bone defects like the maxilla and mandible, the situation may be more complicated, involving craniotomy and aesthetic considerations (Sheikh et al., 2017). The traditional treatment method is autologous bone grafting (a type of autograft), which uses a donor site (such as fibula, rib) in the patient's body for autologous vascularized bone repair. Autologous bone grafting is considered the gold standard for bone replacement because it is not prone to immune rejection and has a low rate of disease transmission (Misch et al., 1999; Prolo et al., 1985; Alt et al., 1999; Dimitriou et al., 2011). Newly implanted tissue is more likely to associate rapidly with surrounding tissues. However, it has limitations, such as limited donor bone mass and the risk of morbidity at the site of transplantation. The resorption rate of the graft is difficult to predict, requiring a richer experimental database to ensure the absorption and degradation of the graft bone, which may lead to prolonged treatment cycles. Moreover, even autologous bone grafts from different locations exhibit significant differences in mechanical and physical properties, further increasing the limitations of this method (Robinson et al., 2020; Betz et al., 2002; Baldwin et al., 2019; Sakkas et al., 2017). As allogeneic transplants are limited in availability as well as in

regenerative capacity, bone tissue engineering emerged as a possible alternative for treating bone defects that are too large to be healed by themselves. Bone tissue engineering combines insights from engineering, sciences and medicine to generate constructs able to regenerate these large defects. The main components of most bone tissue engineering combine scaffolds, cells and biologically active molecules. A very active part of the research in the TE domain is committed to discovering, developing and optimizing materials and structures that are beneficial to bone regeneration (Lanza et al., 2011).

The different steps of bone TE are shown in Figure 1.6. Cells are isolated from the patient (e.g. bone marrow, periosteum) and cultured in an *in vitro* environment. The extracted cells are allowed to proliferate to a sufficient amount for subsequent tissue culture. Under the impetus of growth factors, the cells are gradually guided to divide and differentiate rapidly. Cells can be seeded onto a carrier structure, a scaffold, a cultured in an *in vitro* environment (which can range from a 2D static culture to more dynamic culturing methods such as bioreactors). Finally, the construct is transplanted into the patient's body (Yang et al., 2018).

Animal studies and clinical trials in humans have shown that several factors may influence bone regeneration, such as material properties (natural and/or synthetic) of the scaffolds (with or without cell seeding) (Dehkord et al., 2024). With an improved understanding at the molecular level in tissue engineering, skeletal tissue engineering solutions are becoming increasingly effective (Papantoniou et al., 2021). It is expected that scientific research in this direction will continue at a high rate in the coming years. Research in related fields is also proceeding in parallel, with hopes that many skeletal diseases secondary to trauma, ablative surgery, aging, and metabolic or genetic skeletal diseases will be treated more optimally by new bone regeneration technologies.
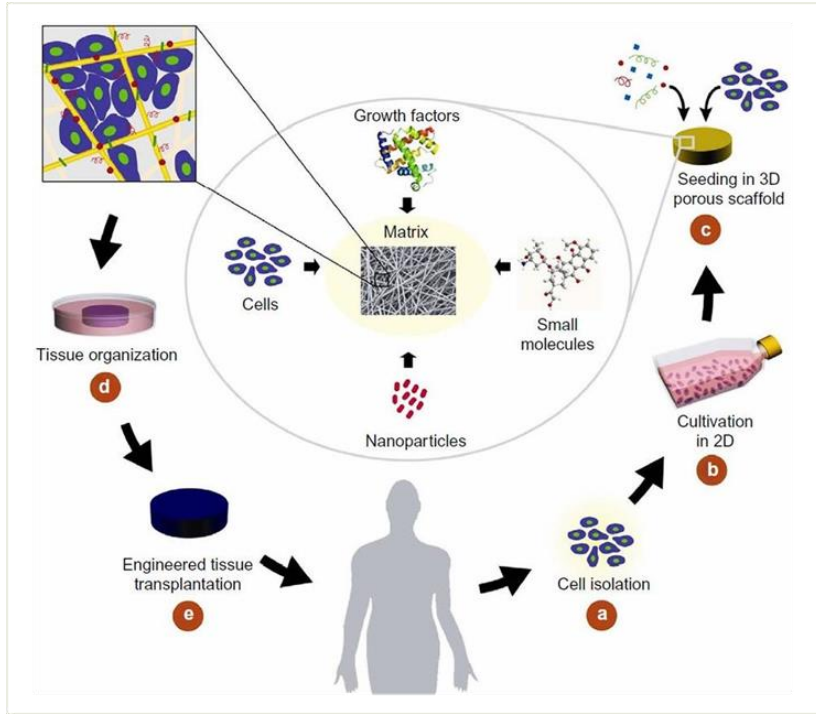
Figure 1.6: Bone tissue engineering treatment strategy. Classical tissue engineering strategies begin with the isolation of cells (a), which are then cultivated in a 2D environment (b). Following cultivation, the cells are seeded into a 3D porous scaffold (c) to provide structure. Growth factors, small molecules, and nanoparticles can be incorporated into the matrix to support cell growth and differentiation. The tissue is then organized within this scaffold (d), leading to the development of engineered tissue. Finally, this engineered tissue is transplanted back into the body to replace or repair damaged tissue (e). (https://www.researchgate.net/figure/Seeding-of-cells-into-fibrous-electrospun-scaffolds-for-tissue-engineering-TE_fig3_338018342, accessed: 17 July 2024)

1.3.1 Cells

Mesenchymal stem cells (MSCs) are pluripotent stem cells with self-renewal and multidirectional differentiation capabilities. MSCs mainly exist in connective tissue and the interstitium of organs, including bone marrow, umbilical cord, fat, mucous membrane, bone, muscle, lung, liver, pancreas, and other tissues, as well as amniotic fluid, amniotic membrane,

and placenta (Nakahara et al., 1991; Mason et al., 1998; Noth et al., 2002; Kern et al., 2006). Bone marrow MSCs have the following characteristics:

1. Strong proliferation ability and multi-directional differentiation potential, with the ability to differentiate into various cells in suitable environments.
2. Immune regulation function, inhibiting T cell proliferation and immune response through cell interaction and cytokine production.
3. Convenient source, easy to separate, culture, expand, and purify, retaining stem cell characteristics without immune rejection.
4. Blurred surface antigen, light rejection of allogeneic transplantation, and non-strict matching requirements (Osyczka et al., 2001; Bosch et al., 2000; Zuck et al., 2001; Wickham et al., 2003).

Because of these immunological properties, MSCs have broad clinical application prospects in treating diseases. They can reconstruct tissue and organ structure and function through autologous transplantation, avoiding immune rejection (Young et al., 2001; Erices et al., 2000). MSCs' multi-directional differentiation potential, their ability to, regulate immunity, and easy isolation and culture techniques have attracted increasing medical attention. In tissue engineering, MSCs have shown great application potential in bone repair (Jiang et al., 2002; Bedada et al., 2006). Work performed by Groeneveldt et al. (Groeneveldt et al., 2014 has investigated the transcriptional differences between periosteal cells derived from long bones (tibia) and jaw bones (mandibula and maxilla). The observed differences could (partially) be attributed to the differences in developmental origin. Differences were observed in *in vivo* bone formation potential when implanted on Calcium Phosphate cells without growth factor stimuli.

1.3.2   Growth factors

Growth factors, signal molecules indicating cell growth and development, play a vital role in tissue regeneration. Controlling growth factors can further control tissue regeneration direction (Babensee et al., 2000).

Growth factors are soluble secreted signal polypeptides guiding specific cellular responses in the biological environment (Whitaker et al., 2001). For bone-related growth factors, these mainly include BMP, bone morphogenetic protein; TGF, transforming growth factor; PDGF, platelet-derived growth factor; aFGF, acidic fibroblast growth factor; bFGF, basic fibroblast growth factor; IGF, insulin-like growth factor (see Table 1). Growth factors bind to receptors on target cells to guide cell behaviour, affecting cell proliferation, differentiation, division, apoptosis, and migration (Tayalia et al., 2009). Growth factor signals often participate in the response as endocrine signals but differ in delivery and response methods, involving short-range diffusion and local effects (Kaigler et al., 2006). The ability of growth factors to transmit signals is related to ECM's diffusion ability, affected by the number of target cells, receptor types, and signal transduction (Lamalice et al., 2007).

Stage of healing	Growth factor	Source, localisation and action	
Immediate injury response	BMP-2/4	Found in mesenchymal cells in hematoma and cambium layer of periosteum adjacent to fracture. BMP-4 mRNA is present in osteoprogenitor cells of the proliferating periosteum, the medullary cavity and the muscles near the fracture.	(Bostrom et al., 1995) (Nakase et al., 1994) (Bolander et al., 1992)
	TGF-β	Released by platelets and inflammatory cells into the fracture hematoma. Stimulates proliferation of mesenchymal cells in cambium layer of periosteum.	(Joyce et al., 1990) (Bourque et al., 1993)
	PDGF	Released by platelets and inflammatory cells into the fracture hematoma. Found in macrophages close to the periosteum 2 days post-fracture, decreases from day 3. Stimulates proliferation of mesenchymal cells in cambium layer of periosteum.	
	aFGF	Found in cells of the expanded cambium layer and associated with rapid increase in mesenchymal cells.	(Bourque et al., 1993)
Intramembranous bone formation	BMP-2/4	Found in osteoblasts lining primitive (woven) bone by 6 days after fracture. Decreases as the bone matures.	(Bostrom et al., 1995)
	TGF-β	Found in proliferating mesenchymal cells, in osteoblasts lining new bone and in the matrix.	(Joyce et al., 1990) (Nakase et al., 1994)
	PDGF	Released by platelets and stimulates intramembranous bone formation.	
Chondrogenesis	BMP-2/4	Chondroid precursor cells stain intensly just prior to becoming immature chondrocytes.	(Bostrom et al., 1995)
	TGF-β	Found in mesenchymal cells, young chondrocytes and mature chondrocytes.	(Joyce et al., 1990)
	IGF-I	Found in young chondroblasts at the edge of the cartilage mass replacing fibrous tissue.	(Bourque et al., 1993)
	aFGF	Synthesized by chondrocytes, their precursors and macrophages. Stimulates chondrocyte proliferation and is probably important for chondrocyte maturation.	(Bolander et al., 1992)
Endochondral ossification	BMP-2/4	Intense intracellular staining of osteoblasts lining the calcified cartilage matrix.	(Bostrom et al., 1995)
	TGF-β	Found in the matrix surrounding hypertrophic chondrocytes.	(Joyce et al., 1990)
	TGF-β	Found in chondrocytes at the edge of the ossification front.	(Bourque et al., 1993)
	bFGF	Probably produced by chondrocytes and is important for endochondral bone formation.	(Bolander et al., 1992)

Table 1.1: Growth factors in bone in tissue regeneration. BMP, bone morphogenetic protein; TGF, transforming growth factor; PDGF, platelet-derived growth factor; aFGF, acidic fibroblast growth factor; bFGF, basic fibroblast growth factor; IGF, insulin-like growth factor (Solheim et al., 2011; accessed: 15 September 2024).

1.3.3   Scaffolds

One of the most important functions of implanted bone regeneration scaffolds is to promote the proliferation and differentiation of seeded cells. With additive manufacturing and computational 3D design, it is possible to generate more efficient 3D scaffolds for bone regeneration in tissue engineering (Hutmacher et al., 2001). The primary considerations for scaffolds suitable for neo-tissue growth and new bone formation include the provision of a conducive physical and chemical environment for neo-tissue growth. Such an environment facilitates cell attachment to the scaffold surface and promotes tissue morphogenesis (Hutmacher et al., 2001).

To mimic the real bone structure, porous scaffolds are used in order to provide a larger surface area for cell attachment as well as to support cell proliferation and differentiation. Porous scaffolds provide enough space for newly formed blood vessels to invade. More blood vessels mean enhanced oxygen transport and higher metabolic rates. The spatial nature of the porous structure meets these needs for oxygen and waste transport (Pilipchuk et al., 2015). The porous nature furthermore facilitates communication between the scaffold and surrounding host tissue, improving the mechanical stability of the implant (Nicholas et al., 2016). Additionally, the release of ions based on the scaffold's chemical composition can benefit neo-tissue growth at the implant site (Ostrowska et al., 2016).

In tissue engineering, various materials for bone regeneration scaffolds have been studied, including metals, ceramics, and polymers. Here, we focus on Calcium Phosphate-based ceramics, which are extensively used as material for bone regeneration, playing a positive role in both bone conduction and osteoinduction. The release of calcium ions regulates the growth, division, and differentiation of osteoblasts and affects osteoclast production and bone resorption, impacting bone regeneration. Phosphorus ions similarly guide bone tissue regeneration. Calcium phosphate comes in various types, such as hydroxyapatite (HA), tricalcium phosphate (TCP), and biphasic calcium phosphates (BCP), each

suitable for different scenarios due to differing mechanical properties, hydrolysis rates, and physical stability. Developers often mix different types or combine calcium phosphate with other materials to optimize performance (Jeong et al., 2019). A general discussion of the properties of biomaterials used in tissue engineering are discussed below.

1.3.4   Biomaterials tissue engineering

Compared with ordinary materials and autologous bone, biomaterial scaffolds have several advantages (Alaribe et al., 2016):

- Good biocompatibility: Biomaterial scaffolds, made from natural or synthetic biomaterials, often display limited foreign body reactions and immune responses.
- No surgical extraction needed: Unlike autologous bone, biomaterial scaffolds avoid complications and postoperative pain from bone extraction.
- Good structure controllability: Biomaterial scaffolds can be customized for size, pore size, and porosity to meet different tissue repair needs.
- Good stability: Biomaterial scaffolds have excellent mechanical properties and stability, remaining intact in tissue without fatigue damage.
- Easy to operate: Biomaterial scaffolds simplify operations, reducing surgical time, trauma, and recovery time.
- Avoid infection risk: Biomaterial scaffolds eliminate the risk of infectious disease transmission, important for patients with infections.

Despite these advantages, biomaterial scaffolds have limitations in practical applications (Schilling et al., 2004):

- High cost limits their use in some regions and medical institutions.
- Rejection and immune reactions may occur, especially with long-term use.
- Histocompatibility and biodegradability may be affected by patient-specific factors, requiring individualized consideration.

- Structure and material selection affect mechanical properties and stability, needing comprehensive evaluation and preclinical tests.
- Postoperative complications, such as infection, scaffold displacement, or destruction, require strict monitoring and treatment.

When choosing a biomaterial scaffold, consider its advantages and limitations, making individualized choices based on patient conditions.

Current development in biomaterials tissue engineering focuses on:

- Novel biomaterials: Exploring biomimetic materials, natural polymers, synthetic polymers, etc., to meet different tissue regeneration needs. For example, bioactive glasses and glass ceramics are used for bone, cartilage, nerve, and tooth restoration (Fernandes et al., 2018).
- Scaffold structure optimization: Designing scaffold microstructures to enhance cell growth and tissue reconstruction through geometric modelling, microstructural parameter optimization, and computational simulations (Adachi et al., 2006).
- Multifunctional biomaterials: Developing materials promoting tissue regeneration, drug release, and cell growth. These materials offer new therapeutic approaches for complex tissue defects and diseases (Chen et al., 2022).
- Clinical application and translation: Bridging the gap between laboratory success and clinical use through large-scale clinical trials and translational research (Ratner et al., 2019).

1.4 Enabling technologies for tissue engineering

1.4.1 Additive manufacturing for bone regeneration

Additive manufacturing, or 3D printing, is increasingly used in bone tissue engineering for creating complex, patient-specific structures with high precision. This technology produces implants, scaffolds, and bone substitutes tailored to individual patient needs. One frequently used application is customized implants for orthopaedic surgery. Traditional

implants often have a poorer fit and reduced functionality due to standardization, which is exacerbated during bone in. Additive manufacturing allows for individual-specific implants matching the affected bone's anatomy, improving fit, function, and patient outcomes. For instance, magnesium-based scaffolds infused with stem cells and growth factors have been used for jaw reconstructions, demonstrating the potential of additive manufacturing for individualized implants (Prasadh, 2019). Challenges in additive manufacturing include selecting biocompatible, mechanically robust materials that support bone growth and repair (Kumar, 2021).

Applying additive manufacturing for bone tissue engineering purposes involves using biocompatible materials, such as ceramics, polymers, and metals, to create implants or scaffolds that promote bone growth and repair. In big lines, materials are printed layer-by-layer to create scaffold geometries described in the section above. The use of high-precision scaffolds improves the success rate of bone regeneration surgery. Studies have shown biocompatible polylactic acid and β-tricalcium phosphate composite materials printed into scaffolds can repair rat humerus, accommodating mechanical loads while promoting new bone tissue (Puppi et al., 2010).

1.4.2 Mathematical modelling of bone regeneration

The process of bone regeneration is complex, with various cells, biomaterials, biochemical factors, and mechanical factors affecting it simultaneously. Since the 1990s, scientists have developed mathematical models simulating bone regeneration to facilitate the understanding of the process and design optimized scaffolds.

Early models focused on mechanical regulation, exploring the relationship between cell behaviour and mechanical stimulation (Carter et al., 1998; Claes et al., 1999; Geris et al., 2004, 2008b; Prendergast et al., 1997). Since the mid-2000s, models have studied bone regeneration after scaffold implantation (Bailon-Plaza et al., 2001). Other models have

examined scaffold porosity's structural characteristics (Lacroix et al., 2009; Charles-Harris et al., 2007; Sanz-Herrera et al., 2008). Research has expanded to include blood vessel growth in porous scaffolds (Geris et al., 2008a; Gomez-Benito et al., 2005; Saz-Herrera et al., 2011), scaffold design's influence on cell adhesion (Sandino et al., 2010; Mehdizadeh et al., 2013; Sun et al., 2013; Melchels et al., 2011), and degradable scaffolds' impact on bone regeneration (Carlier et al., 2011). Models have also explored calcium ion concentration's effect on cell behaviour at transplantation sites (Adachi et al., 2006; Byrne et al., 2007), and factors affecting the healing of larger bone defects (Carlier et al., 2012, 2015a; Ribeiro et al., 2015).

Mathematical modelling methods have become widely accepted in academia and industry, contributing significantly to the development of tissue engineering (TE). Digital simulation's predictability maximizes the scope of experimental research and shortens experiment durations, making it an excellent strategy for designing and optimizing bone tissue engineering treatment plans.

1.5   Conclusion

This chapter has provided an introduction to the various aspects of bone structure, function, and formation, as well as the innovative approaches in bone tissue engineering and regenerative medicine. Understanding the complex biological processes and advanced technologies involved in bone regeneration is crucial for developing effective treatments for bone defects and diseases. Future research and development in this field will continue to advance our capabilities in tissue engineering, ultimately improving patient outcomes and quality of life

CHAPTER 2

Objectives and methodology

The first chapter mainly explained the basic bone concepts bone biology and regeneration. Although certain bone regeneration strategies are already applied in clinical practice, the optimization and innovation of related technologies continues. This doctoral research will focus on the validation and application of *in silico* neotissue growth models to optimize the design of bone regeneration scaffolds, in order to achieve the goal of effectively healing bone defects (such as resulting from alveolar bone loss). This chapter will start by introducing, the overall aim of this PhD project, followed by an overview of the specific research goals that are tackled to reach the overall aim. Finally, the main methodologies applied in this research work are briefly discussed.

2.1   Overall aim of the thesis

Although the process of bone regeneration is increasingly understood, providing solutions for large defects and non-healing fractures is still a major challenge for clinicians and researchers. Interdisciplinary methods are used in the scientific research process of bone TE, including biological experiments and computer modelling. This not only allows the bone regeneration process to be better understood, but also facilitates a departure from the classical trial and error approach, making the experimental process faster and more efficient. Over the past decade, many researchers have worked on the development of computer models of bone regeneration approaches, including the optimization of scaffolds (Jones et al., 2003; Sanz-Herrera et al., 2009; Zadpoor et al., 2015; Roseti et al., 2017; Chakka et al., 2021). The surge in research related to another enabling technology, additive manufacturing or 3D printing, ensures that these optimized scaffolds can be produced (Griffith et al., 2002; Schieker et al., 2006; Park et al., 2010; Inzana et al., 2014; Liu et al., 2019; Zhu et al., 2021). Computer models are used to further understand the scaffolds' degradation process as well as the influence of different growth factors released from the scaffold on the regeneration process (Lacroix et al., 2002; Tuan et al., 2005; Isaksson et al., 2012; Rodriguez et al., 2016; Manhas et al., 2017; Garcia-Aznar et al., 2021). However, the material, porosity, geometric structure, and stiffness of the scaffold still require further optimization, incorporating the latest biological insights and technological developments.

This PhD project undertakes an interdisciplinary approach improve 3D printable scaffold designs for bone tissue engineering. Emphasis is placed on the testing, validation, and application of the *in silico* neotissue growth model developed in house (Guyot et al., 2014) and its use in defining optimizing scaffold design. More specifically, this work will employ a combined *in silico-in vitro* approach to study the effect of structure and material of the scaffold geometry on its neotissue formation and bone regeneration capacity.

2.2   Specific objectives

In order to evaluate the feasibility of the aims, this doctoral thesis has set specific goals. As shown in Figure 2.1, these specific goals are explained in turn in subsequent chapters.

- **Adaptation of a neotissue growth model to determine the applicability of curvature-driven neotissue growth principle in Calcium Phosphate-based scaffolds.** Dedicated experimental tests were performed to confirm the curvature-based growth process was also taking place on CaP substrates. Additionally, they allowed assessing the influence of channel shapes and sizes on neotissue growth, using 3D-printed CaP discs specifically designed for this purpose, seeded with bone marrow-derived stromal cells. The in-house developed Level-Set model of neotissue growth in inert Titanium scaffolds, was recalibrated to capture the neotissue growth dynamics on CaP materials (chapter 3).

- **Application of the adapted model to design efficient 3D scaffold structures for craniomaxillofacial bone regeneration.** Gyroid structures allow meeting both biological and manufacturing requirements. Wall thickness and pore sizes have been investigated, in order to obtained sufficient and sufficiently fast neotissue growth in the scaffold. An *in vivo* cranial augmentation model in rats was used to compare the bone formation in different scaffold structures (gyroid, lattice) and compare it to the clinical gold standard (chapter 4).

- **Further *in silico* improvements of scaffold design to better capture *in vivo* requirements and behaviour.** In the first two results chapters (Chapter 3 and Chapter 4), the feasibility of curvature-driven neotissue growth and the performance advantages of the gyroid structure have been verified. In Chapter 5, we explored additional Triply Periodic Minimal structures, including diamond, double diamond, gyroid, FRD, IWP, Fischer-Koch S, and Schwarz

primitive structures, as well as influence of gradients in the structures. Finally, in order to understand the limitations of the current neotissue growth computational framework to capture *in vivo* (bone) tissue formation and ingrowth, we studied the influence of the initial seeding cell density on neotissue formation within the model (Chapter 5).
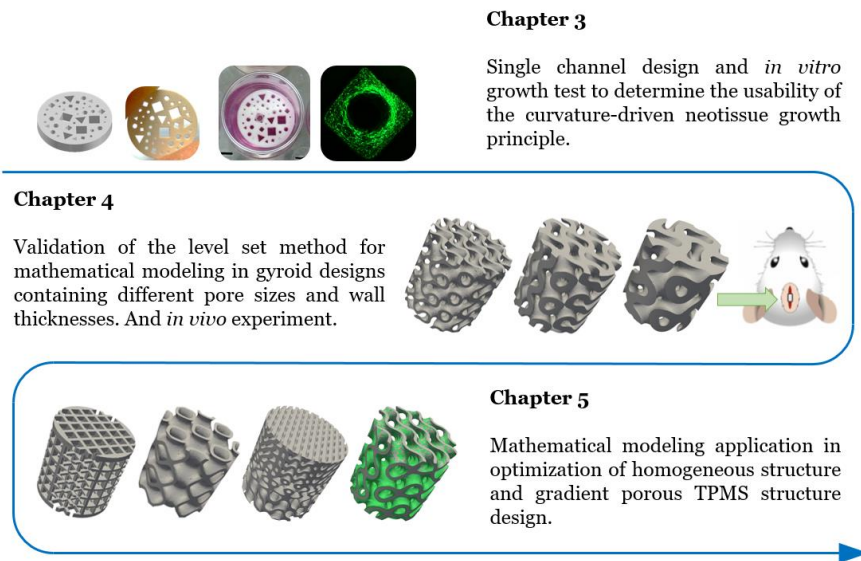
Figure 2.1: Schematic representation of the key concepts and scaffold designs tested in this PhD dissertation. Chapter 3 mainly describes the validation of the curvature-driven neotissue growth model in Calcium Phosphate-based biomaterials. Chapter 4 describes the application of the model in 3D structures. Chapter 5 describes the optimization of the model to better simulate *in vivo* neotissue formation.

2.3 Methodology

This PhD project applies interdisciplinary research methods, combining *in silico* modelling, additive manufacturing and biological *in vitro* an *in vivo* experiments. Below a brief overview is provided of the main methodological elements. Further details are provided in the respective chapters.

2.3.1 Computational modelling aspects

This thesis used FreeFem++ (https://freefem.org/), a free partial differential equation solver, to implement the curvature-based neotissue growth model (Chapter 3 and Chapter 4). This model uses the level set method (LSM) to track the interface between the neotissue and void space, and calculating its movement, influenced by the local curvature. The Salome platform (https://www.salome-platform.org) was used to generate the lattice geometries. We used the mesh generation software GMSH (http://gmsh.info) to optimize the mesh.

For the image analysis of the results of the *in vitro* experiments, we used ImageJ (https://imagej.net/) to calculate the ratio of cell (neotissue) area to the total channel cross section area after separating them using threshold.

2.3.2 Additive manufacturing aspects

In this thesis, stereolithography (SLA) was used to produce the bioceramic implants, in a process optimized by partners Cerhum (https://www.cerhum.com/) and Sirris (https://www.sirris.be). First, hydroxyapatite powders from four different suppliers were tested to determine how they behave at different sintering temperatures. The powders were then evaluated based on several parameters, such as color, density, and mechanical strength. Subsequently, printing experiments were conducted on selected biomaterials, pure hydroxyapatite (HA100), pure tricalcium phosphate (TCP100), and a ratio of 60/40 (HA60-TCP40). Then, the materials and the process of the selected gyroid structure itself were optimized, including cleaning steps, a process to remove excess slurry and a degreasing sintering process to increase the density of the product. Ultimately, it was guaranteed that the material composition of hydroxyapatite would reach more than 95% during the sintering process,

reaching the goal specified by the ISO13175-3 standard (the material composition after sintering is at least 95%).

2.3.3 Experimental aspects

In the *in vitro* experiment (Chapter 3), we used 2D static discs as well as 3D scaffold with specific designs, manufactured in the thee material compositions mentioned above. After manufacturing, the scaffold was sterilized by high temperature and high pressure. The scaffolds were then pre-wetted in the growth medium and air-dried. A commercial immortalized bone marrow derived cell line (hTERT-BMSCs) was used for *in vitro* experiments. Cells were drop-seeded on the scaffold and the seeded discs were transferred to culture plates and cultured in the growth medium for up to 3 weeks. Cell survival and neotissue formation were assessed by fluorescence microscopy. The *in vitro* experiments were conducted at the KU Leuven Skeletal Biology and Engineering Research Center by Ehsan Sadeghian Dehkord.

In the *in vivo* experiment (Chapter 4), a rat cranial augmentation model was used to study bone ingrowth into the scaffolds (gyroid, lattice and the current clinical gold standard material). Results were evaluated after 4 and 8 weeks through nanofocus Computed Tomography (nanoCT) imaging, histology, and biomolecular analyses. The execution and analysis of the *in vivo* experiments was performed by Dorien Van Hede and France Lambert of the dental-Biomaterials Research Unit (d-BRU) at the University of Liège.

CHAPTER 3

Model-based design to enhance neotissue formation in additively manufactured Calcium Phosphate-based Scaffolds

3.1 Abstract

In biomaterial-based bone tissue engineering, optimizing scaffold structure and composition remains an active field of research. Additive manufacturing has enabled the production of custom designs in a variety of materials. This study aims to improve the design of Calcium Phosphate-based additively manufactured scaffolds, the material of choice in oral bone regeneration, by using a combination of *in silico* and *in vitro* tools. Computer models are increasingly used to assist in design optimization by providing a rational way of merging different requirements into a single design. The starting point for this study was an in-house developed *in silico* model describing the *in vitro* formation of neotissue, i.e., cells and the extracellular matrix they produced. The level set method was applied to simulate the interface between the neotissue and the void space inside the scaffold pores. In order to calibrate the model, a custom disk-shaped scaffold was produced with prismatic canals of different geometries (circle, hexagon, square, triangle) and inner diameters (0.5 mm, 0.7 mm, 1 mm, 2 mm). The disks were produced with three biomaterials (hydroxyapatite, tricalcium phosphate, and a blend of both). After seeding with skeletal progenitor cells and a cell culture for up to 21 days, the extent of neotissue growth in the disks' canals was analysed using fluorescence microscopy. The results clearly demonstrated that in the presence of Calcium Phosphate-based materials, the curvature-based growth principle was maintained. Bayesian optimization was used to determine the model parameters for the different biomaterials used. Subsequently, the calibrated model was used to predict neotissue growth in a 3D gyroid structure. The predicted results were in line with the experimentally obtained ones, demonstrating the potential of the calibrated model to be used as a tool in the design and optimization of 3D-printed Calcium Phosphate-based biomaterials for bone regeneration.

3.2 Introduction

In recent years, bone regeneration strategies have advanced significantly in clinical practice. While autologous bone grafting remains a gold standard due to its minimal risk of immune rejection and disease transmission, it presents drawbacks, including donor site morbidity, a limited donor volume, and shaping difficulties (Baldwin et al., 2019; Schmidt et al., 2021). Synthetic biomaterials are gaining attraction as bone scaffolds due to the absence of donor site morbidity and due to their favourable biocompatibility, biodegradability, and foreseeable immunological response (Whedon et al., 2022; Peacock et al., 2010; Foreman et al., 2005; Riddle et al., 2006). Notably, porous scaffolds, particularly those composed of calcium phosphates (CaPs), play a pivotal role in bone tissue regeneration. CaPs, like hydroxyapatite (HAp) and tricalcium phosphate (TCP), exhibit similarities to bone's inorganic composition (see review by Hou et al. With the use of additive manufacturing technologies (AMTs), patient-specific implants have become a (clinical) reality (Garot et al., 2021; Lin et al., 2019). Their design is based on a range of considerations, including the printing technology, the material, and the macroscopic mechanical requirements (Hou et al., 2022). The design of microscopic properties has typically been dominated by considerations of interconnectivity, porosity, and pore size. However, in recent years, local curvature has been shown to be an important factor in driving bone regeneration (Van Hede et al., 2022; Yang et al., 2022; Li et al., 2023).

When optimizing scaffold designs, *in silico* modelling (i.e., the use of computer modelling and simulation) is a key approach to limiting the amount of *in vivo* testing required, in line with the 3Rs principle (reduce, refine, and replace animal tests), by selecting the most promising designs based on the predictions made by the model. A variety of models of bone regeneration *in silico* have been proposed in the literature, with most of them corroborated on the basis of historical or animal experiments. In addition, most of these models focus on regeneration without a support structure (Carlier et a., 2015) or on a predefined shape (Perier et al., 2020; Sandino et al., 2010; Sandino et al., 2010) rather than using the model to select the optimal internal architecture of the structure. On the other hand,

earlier approaches aiming for a more objective optimization often focused on optimizing the mechanical properties of the structure without taking into account internal form or biological requirements (Coelho et al., 2015; Dias et al., 2014). Due to the recent increase in attention for curvature-based biology in general (Schamberger et al., 2023), scaffold research has also turned to local curvature to optimize the internal design of bone substitutes to maximize neotissue formation (Rumpler et al., 2008; Bidan et al., 2013; Guyot et al., 2014; Guyot et al, 2016; Alias et al., 2017; Blanquer et al., 2017; Buenzli et al., 2020). In several cases, dedicated validation experiments have been performed, consisting mostly of *in vitro* cell culture experiments on titanium, hydroxyapatite, or polycaprolactone 2D and 2D+ substrates.

In this study, we aim to improve the design of Calcium Phosphate-based additively manufactured scaffolds by using a combination of *in silico* and *in vitro* tools. We build on our prior work related to the curvature-based modelling of neotissue growth in additively manufactured titanium implants (Guyot et al., 2014) in order to account for the effect of the use of active CaP-based biomaterials. To recalibrate the model, we have designed a dedicated *in vitro* experiment allowing us to evaluate the effect of pore shape and pore size on neotissue growth in scaffolds produced with HAp, TCP, and an HAp–TCP blend (biphasic calcium phosphate, BCP). After running a Bayesian optimization for the model recalibration, we test the predictive capacity of the model by performing a new neotissue formation experiment, both *in silico* and *in vitro*, in a 3D gyroid structure. The observed correspondence between the *in vitro* and *in silico* results is an indicator of the potential of the model to be used in the design and optimization of more complex 3D bone tissue engineering scaffolds.

3.3 Material & Methods

3.3.1 *In silico* model

This section describes the setup, implementation, and optimization of the *in silico* model for curvature-based neo-tissue growth applied to CaP-

based biomaterials. The effect of the released ions is not considered explicitly in the developed model but instead is captured by the changes in the overall neotissue growth rate during the model calibration phase.

3.3.1.1 Level Set Method

The level set method (LSM) is a mathematical approach for tracking moving interfaces, in which the parameterization of curves and surfaces can be conveniently performed to study the change in the morphology and topology of objects (Osher et al., 1988). We have previously used the LSM to implement curvature-based neotissue growth in titanium scaffolds (Guyot et al., 2014; Guyot et al., 2016) as, amongst other advantages, it can effectively be used to calculate the average curvature as a guiding factor for tissue growth simulations.

A signed distance function (φ) describes the distance of each node of the desired domain to the interface. The zero iso-surface determines the moving interface. In the current study, the interface divides the computational domain into two subdomains, neotissue, and void space, according to the following definition:

$$\begin{cases} \varphi > 0 & \text{in} \quad \Omega_{nt} \\ \varphi < 0 & \text{in} \quad \Omega_{v} \\ \varphi = 0 & \text{in} \quad \Gamma \end{cases} \tag{1}$$

with Ω denoting the domain of interest, and Ω_{nt} and Ω_{v} denoting the neotissue and void space subdomains, respectively. The interface between Ω_{nt} and Ω_{v} is denoted by Γ. The LSM formalism for tracking the interface moving with growth velocity $\mathbf{v_G}$ can be expressed by the convection equation, describing how the level set function φ evolves in the entire domain Ω over time:

$$\frac{\partial \varphi}{\partial t} + \mathbf{v_G} \cdot \nabla \varphi = 0 \quad \text{in} \quad \Omega \tag{2}$$

This equation is solved with a homogenous Neumann boundary condition ($\frac{\partial \varphi}{\partial n} = 0$) with n being the normal to the computational domain Ω. The

calculation of the interface advection velocity $\mathbf{v_G} = V_G \cdot \mathbf{n_\Gamma}$ (with $\mathbf{n_\Gamma} = \frac{\nabla\varphi}{|\nabla\varphi|}$) is related to the local mean curvature κ ($\kappa = \nabla \cdot \mathbf{n_\Gamma}$) of the neotissue interface (shown in Figure 3.1a).

$$V_G = A \cdot g(\kappa) \cdot \mathbf{n_\Gamma}$$

$$g(\kappa) = \begin{cases} -\kappa, & \text{if } \kappa > 0 \\ 0, & \text{if } \kappa \leq 0 \end{cases}$$
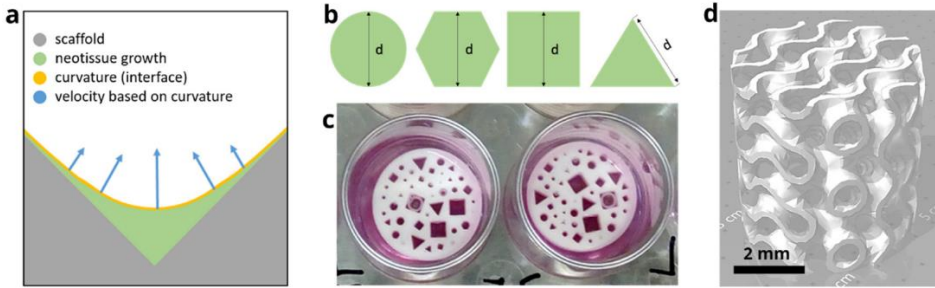
Figure 3.1: *In silico–in vitro* experimental design element. (a) Schematic representation of the different domains of the level set method showing the curvature-based growth velocity (in blue) as well as the interface (in yellow) between the neotissue (in green, $\varphi > 0$) and void space (in white, $\varphi < 0$). (b) Individual channel geometries and sizes (indicated by d). (c) Additively manufactured disks shown in the wells (diameter 14 mm) of a 24-well plate submerged in culture medium. (d) 3D scaffold with gyroid design.

A is a parameter to control the curvature effect, determined from experimental data in a fitting procedure. The negative sign in the definition of $g(\kappa)$ comes from the fact that, according to our definition of φ, the normal $\mathbf{n_\Gamma}$ points towards the neotissue, so growth has to be towards the opposite of $\nabla\varphi$.

3.3.1.2   Implementation of the model

The curvature-based model was solved numerically using the finite element method, implemented in the open-source partial differential equation (PDE) solver FreeFEM (v4.6, Laboratoire Jacques-Louis Lions,

Université Pierre et Marie Curie, Paris, France) (Hecht et al., 2012). The computational domain consisted of individual beams of 2 mm height and triangular, squared, hexagonal, or circular cross-sections of diameters 0.5 mm, 0.7 mm, 1 mm, and 2 mm (Figure 3.1). The geometries and their corresponding computational mesh were created using the SALOME platform (v9.8.0, Salome-platform.org, France) (Ribes et al., 2007), and all the other pre-processing steps were performed in FreeFEM. The computational mesh was generated using a set of first-order tetrahedral elements, and the convergence was checked (Appendix A).

To initialize the LSM, an initial distance function, φ_0, was defined in the domain Ω at the boundary of the scaffold. However, the level set function, φ, is not differentiable where the gradient is discontinuous, meaning that the normal $\mathbf{n}_\Gamma$ and the curvature κ cannot be properly defined everywhere in the domain. A solution is to add a small numerical diffusion term to the expected direction $\mathbf{n}_\Gamma$ and curvature κ. The specific mathematical expression is as follows:

$$\mathbf{n}_\Gamma = \frac{\nabla\varphi}{|\nabla\varphi|} + \varepsilon\,\Delta\mathbf{n}_\Gamma$$

$$\kappa = \nabla\cdot\mathbf{n}_\Gamma + \varepsilon\Delta\kappa$$

During the verification process, a comparison of images generated by different diffusion values showed that the smaller the value of ε, the greater the oscillation of the curvature calculation and the worse the smoothness of the boundary. Conversely, the larger the value of ε, the larger the influence of the numerical diffusion, generating erroneous results. In Guyot et al, the parameter ε was fixed at 1×10^{-4} based on a comparison between the numerical and analytical solutions. In the process of initializing the level set function φ, the open-source software mshdist (v1.0, by Charles Dapogny (Université Joseph Fourier) and Pascal Frey (Université Pierre et Marie Curie), France) (http://ljk.imag.fr/membres/Charles.Dapogny/software.html) was used to avoid the level set distortion that the distance function in the model application may cause.

To reduce the computational cost, the method of characteristics can be used in FreeFEM (Polyanin et al., 2001). This method reduces a partial differential equation (PDE) to a system of ordinary differential equations (ODE) along curves called characteristics. The resolution of these ODEs along those curves leads to the solution of the original PDE. To further improve the performance of the model and decrease the execution time of simulations, model parallelization was taken into account. Parallelization was considered for two main stages of the computation pipeline: assembling the matrices and solving the resulting linear system of equations. As part of a standard finite element computation, assembling the matrices requires extensive numerical integration on each element. This can be conducted in parallel by distributing elements among the available nodes. In this regard, a primary domain decomposition technique using the Message Passing Interface (MPI) was implemented to assign a subset of elements to each available computing node. After performing the integration, the results of all nodes are gathered to assemble the linear system of equations. In the current implementation, an MUMPS sparse direct solver (v5.5.1, Mumps Technologies SAS, Lyon, France) (Amestoy et al., 2001) was used to solve the linear system. The post-processing of the results was carried out using ParaView (v5.11, Kitware Inc., New York, NY, USA) (Ahrens et al., 2005).

3.3.1.3   Optimization of the velocity control value

Obtaining the correct values for the parameters of a computational model can be pretty challenging and may require dedicated experimental input. In this regard, defining an efficient inverse problem can help save time and resources when estimating the unknown parameters. In this study, a dedicated *in vitro* experiment was set up, and the results were used in a Bayesian optimization routine (Mockus et al., 2012) to calibrate the parameter A. The objective function of the inverse problem was the root-mean-square error of the difference between the predicted and experimentally obtained values of tissue growth rate over 21 days.

3.3.2 *In vitro* experiments

3.3.2.1 Design of the disk

In order to efficiently test a range of pore geometries and sizes, a disk was designed with a height of 2 mm and a diameter of 14 mm, fitting the well of a 24-well plate. In the disk, channels were included, with four basic cross-sections (triangle, square, hexagon, and circle) and three sizes. They were 0.5 mm, 0.7 mm, and 1 mm for the circle and hexagon and 0.7 mm, 1 mm, and 2 mm for the square and triangle, as with the latter shapes, the smallest size could not be accurately produced. Each combination of cross-sectional shape and size was repeated three times. All channels were arranged randomly on the disk, with at least 60 μm in between them. Table 3.1 provides a summary of the experimental setup.

Pore shapes	Triangle, square, hexagon, circle
Pore size	0.5mm, 0.7mm, 1mm and 2mm
Distribution	Randomly
Materials	Hydroxyapatite (HA, 100%), Tricalcium phosphate (TCP, 100%), mix HA 60% - TCP 40% pastes (supplier Cerhum)
Sintering temperature	1030°C for TCP100 and HA60-TCP40, and 1130°C for HA100
Time points analysis	10 days and 21 days
Cell type	Human telomerase reverse transcriptase-immortalized bone marrow mesenchymal stem cells (hTERT-BMMSCs)

Table 3.1: Disk design, manufacturing parameters, and experimental variables considered for the *in vitro* experiment in this study.

3.3.2.2 Design of the gyroid scaffold

Upon confirmation of the curvature-based growth principle in CaP-based scaffolds (see results section), a 3D structure was designed that allowed us

to test the potential of the *in silico* model to predict neotissue growth in more complex geometries. Triply periodic minimal surface structures in general and gyroid structures in particular provide an environment with a well-controlled curvature and a narrow curvature distribution (Blanquer et al., 2017). Gyroid structures (or triply periodic minimal surfaces in general) have received an increasing amount of attention over the last couple of years for this reason. In addition to being interesting from a biological/mathematical perspective, they are also very manufacturing-friendly, as the geometry varies very smoothly from one layer to the next.

3.3.2.3 Production of the disk and scaffold

The disks were produced through stereolithography using different CaP-based pastes from Cerhum (Liège, Belgium): pure hydroxyapatite (HAp100), pure tricalcium phosphate (TCP100), and a 60/40 mixture of the two (HAp60 TCP40), also known as BCP. Stereolithography is an additive manufacturing process that builds polymer parts in 3D by photocuring a liquid or paste. Here, the bioceramic powder was carefully mixed with organic components (polyfunctional acrylic resins and a UV photoinitiator) in order to obtain a viscous paste material with roughly 50% solid loading to be processed by SLA (Cerhum and Sirris, Liège, Belgium). During manufacturing, the suspension was spread on the working area in thin layers of 50 μm, after which UV light was projected by a digital light onto the paste surface. Subsequently, the samples were subjected to a thermal cycle (1030 °C for TCP100 and HAp60-TCP40 and 1130 °C for HAp100 for 5 h), allowing for the removal of the resin and the densification of the ceramic, as reported and discussed elsewhere (Van Hede et al., 2022; Blanquer et al., 2017; Goffard et al., 2013; Champion et al., 2013; Bouakaz et al., 2023). After manufacturing, the parts were rinsed and ultrasonically cleaned in an 80% ethanol bath for 10 min. The same process was followed for the manufacturing of the 3D gyroid structure (HAp100).

3.3.2.4 Cell culture and analysis

After production, the disks were sterilized with an autoclave at 121 °C for 15 min. Prior to the cell culture experiment, the disks were pre-wetted for 3 h with growth medium (GM) composed of Prigrow II Medium + Fetal Bovine Serum (FBS) to a final concentration of 10% + hydrocortisone to 10^{-6} mol/L and Penicillin/Streptomycin Solution to a final concentration of 1%. After prewetting, the disks were air-dried for 1 h under sterile conditions. Then, 600,000 hTERT-Immortalized Bone Mesenchymal Stromal Cells (hTERT-BMSCs, Applied Biological Materials Inc. Richmond, Canada) were drop-seeded onto each disk suspended in a 200 μL cell suspension and subsequently incubated statically for 4 h at 37 °C to facilitate cell attachment. The amount of cells was chosen to ensure a good baseline coverage of the disk with cells without having open spaces on the disk. Then, the cell-seeded scaffolds were transferred to a 24-well plate and cultured in GM for 3 weeks. The medium was refreshed three times a week. The cell viability and kinetics of the neotissue (cell+ECM) channel filling were evaluated after 10 and 21 days of *in vitro* culture for the different pore geometries using fluorescence microscopy imaging (Live−Dead viability/cytotoxicity staining (Invitrogen, Thermo Fisher Scientific inc., Waltham, MA, USA) and DAPI/Phalloidin). Disks were rinsed with 1 mL of PBS, incubated in the staining solution (0.5 mL of calcein AM and 2 mL of ethidium homodimer in 1 mL of PBS) for 20 min under standard cell culture conditions, and finally imaged using an Olympus IX83 inverted fluorescence microscope (Evident, Tokyo, Japan).

Similar steps were followed for the 3D structure. First, 200,000 cells were drop-seeded and allowed to attach for 3 h prior to the start of the static culture. Neotissue formation was evaluated at days 10 and 21 using contrast-enhanced nanofocus Computed Tomography (nanoCT) imaging with an 80% Hexabrix 320 solution (Guerbet, Villepinte, France) as a contrast agent (applied for 20 min) to visualize the neotissue inside the scaffold. NanoCT scans of the samples were acquired using the GE Nanotom-M (Phoenix Nanotom® M, GE Measurement and Control Solutions, Billerica, MA, USA). The scaffold was scanned with a diamond−

tungsten target, mode 0, a 500 msec exposure time, 1 frame average, 0 image skips, 1800 images, and a 0.2 mm aluminum filter. The constructs were scanned at a voltage of 70 kV and a current of 150 µA, resulting in a voxel size of 4 µm.

3.3.2.5   Image processing

All images from the fluorescence microscopy were analysed with ImageJ software version 1.53q for Windows (v1.53, ImageJ software, Wayne Rasband and contributors, NIH, Bethesda, MD, USA), using Bio-Format (v7.0.1, Bio-Format project, Madison, WI, USA) as a plugin for ImageJ to read and write images in the formats it supports. The image analysis provided a qualitative and quantitative measure of the filling of each channel on the disk.

CTAn (v1.18.8.0, Bruker Belgium SA, Kontich, Belgium) was used for image processing and the quantification of newly formed tissue based on automatic Otsu segmentation, 3D space closing, and a de-speckle algorithm. The percentage of neotissue was calculated in relation to the total scaffold volume. CTVox (v3.3.0, Bruker Belgium SA, Kontich, Belgium) was used to create 3D visualization.

3.3.2.6   Statistical analysis

All data from the quantitative processing of the fluorescence microscopy images were statistically analysed using GraphPad Prism software version 8.2.1 for Windows (GraphPad Software, San Diego, CA, USA). To compare multiple groups' means with three repeats, a statistical analysis of the results was performed by a two-way analysis of variance (ANOVA), followed by post hoc tests (Tukey's multiple comparison test). Significant levels are reported as follows: * $p < 0.05$, ** $p < 0.01$, *** $p < 0.001$, and **** $p < 0.0001$.

3.4   Results

3.4.1   Analysis of *in vitro* cell behaviour

The percentage of neotissue formed within the channels was calculated using image processing on fluorescent images (Figure 3.2). The Live/Dead staining showed the good biocompatibility of the produced CaP disks with the hTERT-BMSCs. The fluorescence images revealed a viable cell population for all pore channels on both time points with a greater abundance for day 21 compared to day 10. Cells were seen to attach to the top surface of the disk as well as the pore walls. The pattern of neotissue growth in the channels, particularly for the triangle, square, and hexagon shapes, demonstrates that neotissue growth indeed starts in the areas of the highest curvature, ultimately forming a circular growth boundary. Subsequently, neotissue continues to grow towards the centre of the channel, gradually filling it up. This was observed to happen regardless of the shape and size of the initial channel or the material used, confirming the curvature-based hypothesis for the tested materials. The results of the quantification of neotissue formed for different channel cross-sectional shapes and sizes and different types of CaP biomaterials on days 10 and 21 are shown in Figure 3.3 and in Table B1 and Figure C1, Figure C2, Figure C3 and Figure C4 in Appendix B and C, respectively. When comparing the different materials (using the channels with 0.7 mm and 1 mm diameters as examples), the experiments demonstrated that the results for HAp (0.7 mm: 38% on day 10 to 93.42% on day 21; 1 mm: 30% on day 10 to 76.83% on day 21) and TCP (0.7 mm: 49.58% on day 10 to 86.67% on day 21; 1 mm: 33.42% on day 10 to 69.33% on day 21) were not significantly different; however, the BCP results (0.7 mm: 23.67% on day 10 to 59.83% on day 21; 1 mm: 17.08% on day 10 to 48.08% on day 21) were significantly lower on day 21 (Figure 3.3b). Comparing the pore shapes, the triangles mostly showed faster growth than squares, hexagons, and circles (Figure 3.3c and Figure 3.4a), although the influence of the material and pore size confounded the results. For the largest sizes (2 mm in the triangle and square channels), the growth rate was strongly reduced

compared to all others, with limited neotissue formation present in the corners, though the circularization of the neotissue interface was still visible.
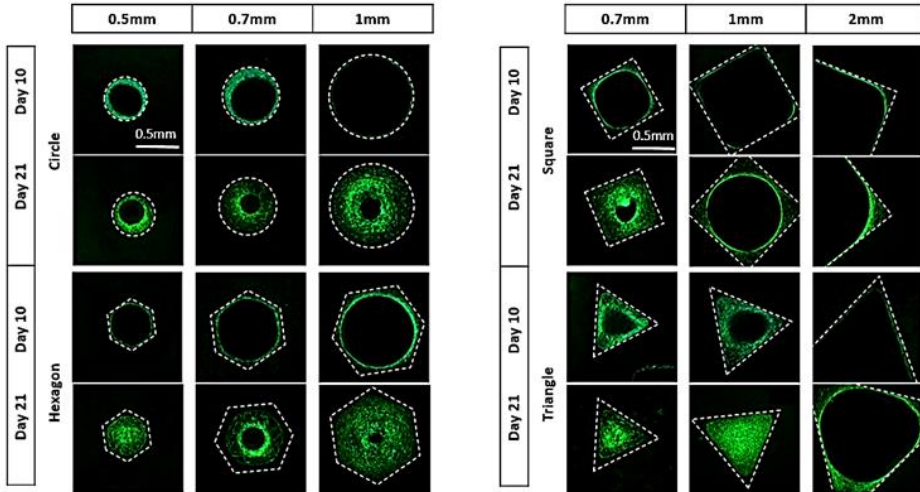
Figure 3.2: Neotissue growth results in the different channels for HAp disks (representative images) for the different channel shapes and diameters over time. Looking vertically, it is evident that for every shape and size, curvature-driven neotissue formation is taking place over time. Scale bar (0.5 mm) is the same for all panels.
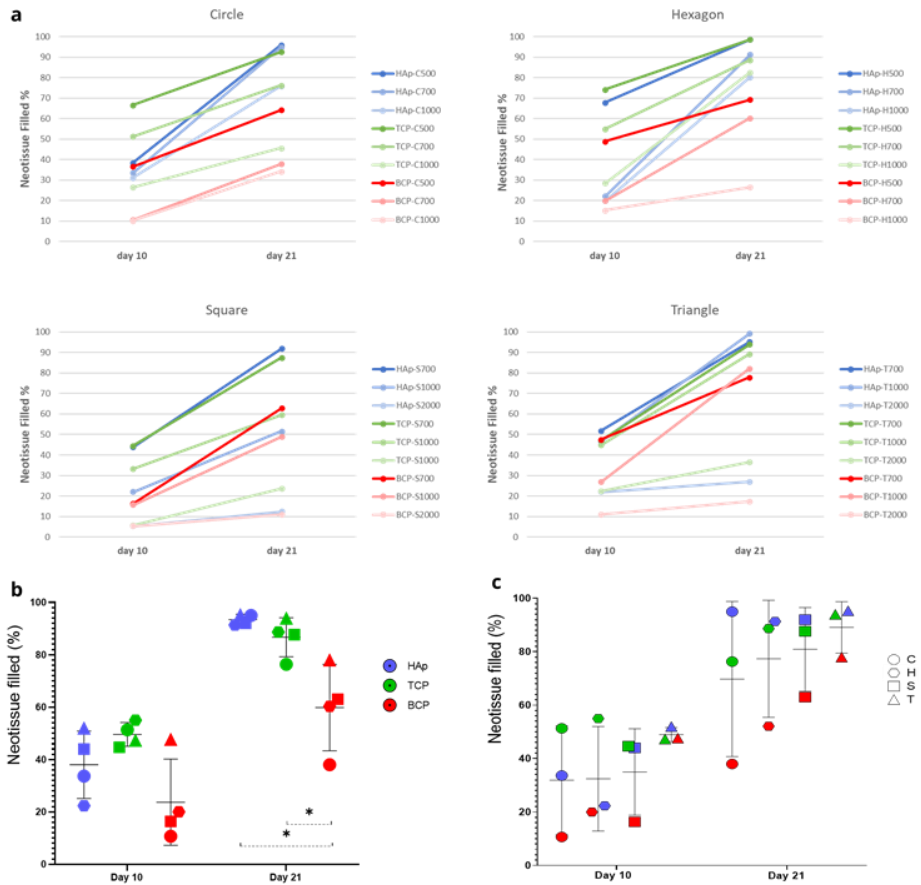
Figure 3.3: Quantification of experimental results. (a) Percentage of channel cross-section filled with neotissue after 10 and 21 days for the different channel shapes, shown as the mean. The labels in the legend refer to the material used (HAp, TCP, BCP), the shape (C: circle, H: hexagon, S: square, T: triangle), and the channel diameter in micrometres. (b) Percentage of channels with a diameter of 0.7 mm filled with neotissue after 10 and 21 days comparing different CaP biomaterials, shown as the mean of various shapes ± SD, and (c) percentage of channels with a diameter of 0.7 mm filled with neotissue after 10 and 21 days comparing different shapes, shown as the mean of various biomaterials ± SD. Statistical significance is calculated by two-way ANOVA test; * p < 0.05.
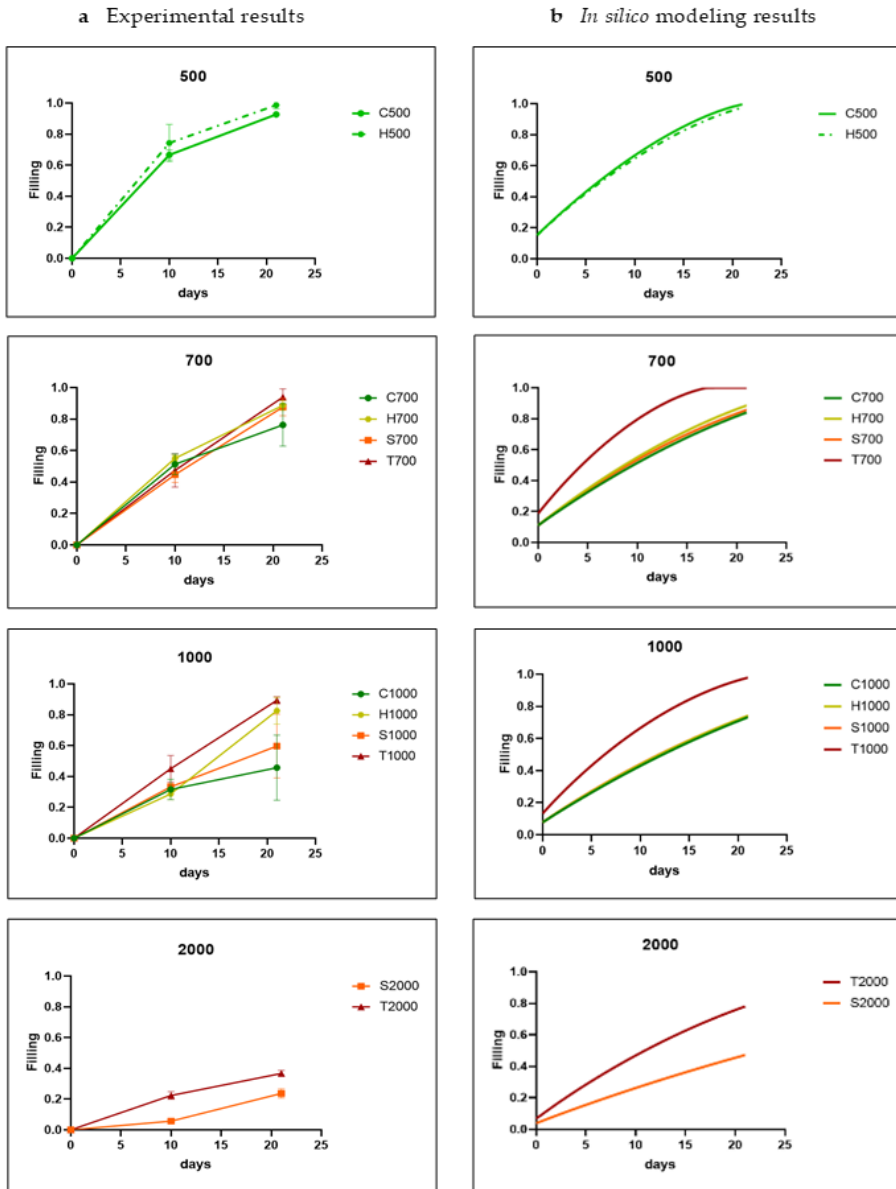
Figure 3.4: Comparison between experimental results (a) and *in silico* results (b) for each channel size (parameter A was fixed at 0.3 during Bayesian optimization) for HAp disks. The shapes are labelled by a letter (T: triangle; S: square; H: hexagon; C: circle) and a number indicating the channel diameter in micrometres. The experimental data are shown as mean ± SD.

3.4.2 *In silico* modelling

As the experimental results confirmed the *in silico* model's basic premise of curvature-based neotissue growth, qualitatively, the simulation results largely corresponded to the experimental ones. Bayesian optimization was used as indicated in the Methods section in order to calibrate the model parameter A for all materials, shapes and sizes and was ultimately fixed at 0.3 for the HAp disks, 0.01 for the TCP, and 0.001 for the BCP disks. The optimization led to a good quantitative correspondence between the experimental and simulation results, shown in relation to channel size (Figure 3.4) and channel shape (Figure 3.5). The simulation results showed, as expected from the curvature-based principles, that increasing the channel diameter decreased the neotissue growth rate (Figure 3.4). For the channel sizes 0.5 mm and 0.7 mm, all the shapes reached high filling percentages on day 21. However, especially for 0.5 mm, the experimental time points did not allow us to assess the exact time point at which 100% filling was reached. Hence, this could explain the qualitative difference in filling rates between the experiments and simulations, with the filling tendency appearing as a polyline in the experimental result and a smoother line in the simulations. The hexagon shows the fastest neotissue growth across all sizes, whereas for the smallest sizes (0.7 mm and 1 mm), the triangular channel fills up fastest both in the experiments and the simulations due to the curvature being highest in those channels and the neotissue growing inward from the corners being more likely to establish contact quickly. For the size 1 mm, the triangle was still the fastest-growing one, almost reaching 100% filling on day 21, followed by the circle and hexagon, which reached about 60% filling on day 21. The square was relatively slow, and the final filling rate was about 40%. For the size 2 mm, the filling rate of the four basic shapes did not exceed 20%.
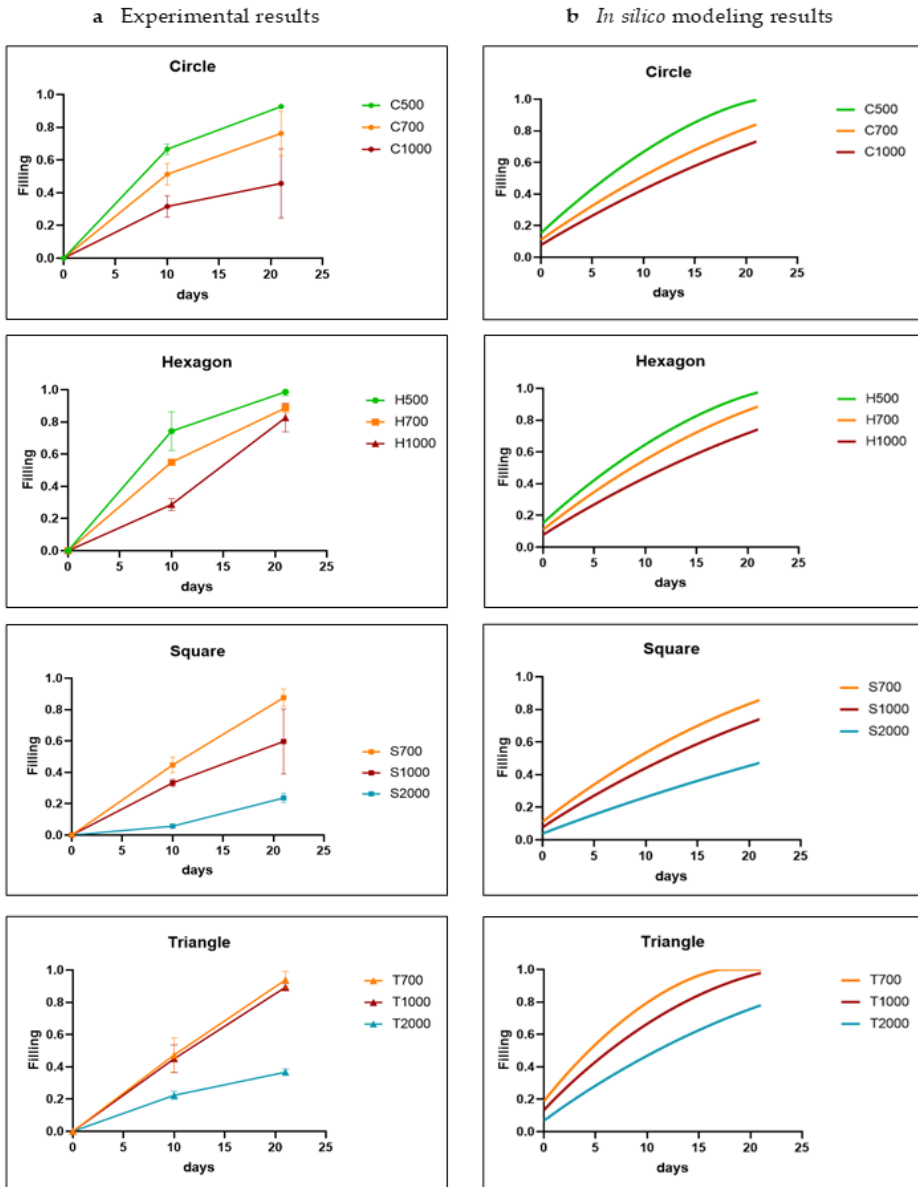
Figure 3.5: Comparison between experimental results (a) and *in silico* results (b) for each channel shape (parameter A was fixed at 0.3 during Bayesian optimization) for HAp disks. The shapes are labelled by a letter (T: triangle; S: square; H: hexagon; C: circle) and a number indicating the channel diameter in micrometer. The experimental data are shown as mean ± SD.

3.4.3 Model-informed 3D scaffold design and validation

Based on the results obtained with the basic geometries, neotissue growth in a 3D HAp structure was predicted and experimentally assessed to provide a validation step. A triply-periodic minimal surface structure (gyroid) was designed with a 0.2 mm wall thickness and 0.9 mm pore size (Figure 3.1d) to respect manufacturing constraints. Due to differences in the initial seeding densities between the experimental disc and 3D structure experiments, different values of the thickness of the initial cell layer were tested (10 μm (L1 in Figure 3.6a) and 1 μm (L2 in Figure 3.6a), respectively), as seeding at a non-confluent density was followed by a period of mostly 2D growth before starting growth in the third dimension, leading to an overall reduction in the speed of neotissue formation (Figure 3.6a,b). *In vitro* experiments under static conditions in growth medium were executed for the designed gyroid structure, produced in HAp, and analysed using contrast-enhanced nanoCT imaging (with Hexabrix as a contrast agent) (Figure 3.6c). The quantitative comparison demonstrated a similar trend in neotissue growth between day 10 and day 21, illustrating the potential of the model to be used as a tool to design 3D bone tissue engineering scaffolds.
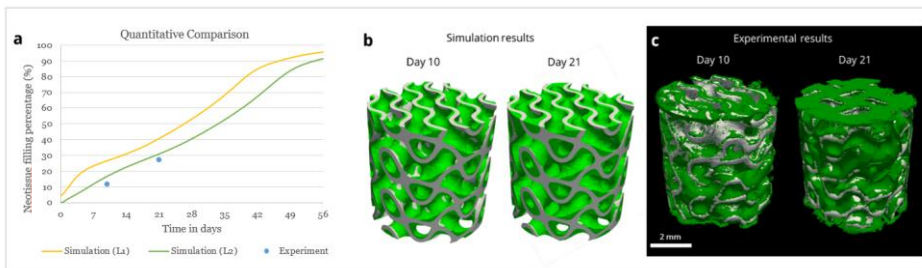
Figure 3.6: Comparison between *in vitro* experiment and simulations for 3D HAp gyroid structure. (a) Quantification of the neotissue formation (% of filling as a function of time (days)) in the experiment (points) and simulations (full line). L1 = initial thickness of neotissue layer, 10 μm; L2 = initial thickness of neotissue layer, 1 μm. (b) Quantitative view of simulation results on day 10 and day 21. (c)

Contrast-enhanced nanoCT images of *in vitro* experiments on day 10 and day 21, with neotissue in green pseudo-colour.

3.5 Discussion

Optimizing the scaffold shape with respect to cell (in)growth remains an open challenge in tissue engineering. With additive manufacturing, not only material composition and overall porosity but also the microarchitecture can be designed and accurately produced. The present model builds on previous work for simulating neotissue growth in titanium additively manufactured scaffolds (Guyot et al., 2014) in order to investigate neotissue growth in Calcium Phosphate-based scaffolds. First, a dedicated 2D+ *in vitro* experiment was designed, allowing us to qualitatively and quantitatively compare the influence of channel shape and size for different CaP materials. The final calibrated model was then used to predict neotissue growth on a 3D gyroid-based scaffold, showing adequate agreement between the simulation results and the *in vitro* experiments. The most important contribution of this study is the application of the neotissue growth model to CaP additively manufactured scaffolds, moving from basic shapes and 2D+ substrates to experimentally validated complex 3D structures.

A Bayesian approach was followed for calibrating the computational-intensive model (Barzegari et al., 2021) since it minimizes the number of optimization iterations, during each of which the computational model should run at least once. Since evaluating the objective function is expensive, a Bayesian optimization routine considers the previous iterations to choose the following values by constructing a probability tree of the objective function, acting as a surrogate model, which makes the selected approach more efficient than gradient-based or fully stochastic methods (Mockus et al., 2012). The probability model is a conditional probability, p (score parameters), which gets updated by the optimization algorithm during each iteration by incorporating newly obtained results. This operation was carried out by Sequential Model-Based Optimization (SMBO) methods, which need fewer optimization iterations than methods relying on a random selection of values (stochastic methods) or

approaches needing an evaluation of the objective function at least twice (gradient-based methods) (Mehrian et al., 2018).

Regardless of the basic shape and channel size tested, the neotissue growth showed the hallmarks of curvature-based growth, including the circularization of the neotissue-void interface taking place over time and the neotissue growth speed decreasing for the larger channel sizes. For all the materials tested, the triangular shape demonstrated the fastest growth with the lowest variability compared to the other channel geometries of the same size. This might appear to contrast with our previous study, where, when testing basic shapes in titanium scaffolds, the triangle performed worst in terms of speed (Guyot et al., 2014). However, in that study, the parameter d was chosen as the diameter of the inscribed circle rather than the side of the triangle, as was done here (Figure 3.1b), leading to a substantially larger surface compared to the other shapes (~30%) with longer straight edges between the corners and hence a slower filling. The results of this study are in agreement with other reports using a dimensionalisation similar to the one used here (Rumpler et al., 2008). For the smallest diameter channels (500 μm in the hexagon and circle), complete filling was reached during the experiment in between the first and second observation time points, explaining the experimentally observed change in growth speed between both points. Not knowing the exact point of filling, the simulations were unable to account for it accurately, leading to a smoother behaviour in the simulation results compared to the experimental observations.

Extending the use of the model from basic shapes towards 3D structures for the same materials and experimental settings is a strong point of this study. For the 2D+ set-up, cells were seeded at a density close to confluency to speed up the onset of growth inside the channels. For the 3D structure, a lower initial density was chosen, moving towards densities more typically used in tissue engineering applications (Kerckhofs et al., 2016). This meant that the initial phase of the neotissue growth was mostly driven by the growth of cells onto the substrate (Kommareddy et al., 2010). As this type of growth is not captured by the current model, it

was simulated by lowering the initial thickness of the cell layer to 1μm. This resulted in slower predicted neotissue growth in the initial phase, followed by a neotissue growth rate and final filling density similar to those obtained for a higher initial cell layer, in line with the experimental observations (Figure 3.6a). This second phase of neotissue growth is characterized by cells growing on top of the extracellular matrix they have produced themselves, as described in (Kommareddy et al., 2010). The gyroid structure used in this study (defined by its pore size and wall thickness) was the result of an *in silico* study in the context of oral bone regeneration, balancing the need for rapid neotissue (in)growth, the need for a high neotissue-to-biomaterial ratio, and the constraints imposed by the additive manufacturing process. The gyroid structure was tested for its capacity to induce *in vivo* bone formation in a cranial augmentation model (implantation without seeded cells), showing the superiority of the design over the clinically used gold standard and a lattice structure control (Van Hede et al., 2022).

Compared to our own previous work (Guyot et al., 2014; Van Bael et al., 2012), moving from titanium to CaP-based materials led to a decrease in the neotissue growth rate. This might be related to the active nature of the CaP material, which could be shifting the balance from the proliferation of the progenitor cells towards their early differentiation (Winning et al., 2017) or to the difference in surface composition and topography (Cun et al., 2020). Both factors might also provide additional insight into the obtained experimental differences for the different materials that were tested. A wide range of *in vitro* and *in vivo* studies have been reported in the literature with the different calcium phosphate materials used in this study (reviewed extensively in (Jeong et al., Milazzo et al., 2019; Bal et al., 2020; Tavoni et al., 2021; Han et al., 2021; Yazdanpanah et al., 2022; Noordin et al., 2022)). These reports describe how differences in composition, manufacturing techniques, sintering temperatures, surface treatments, etc., result in differences in terms of (amongst others) mechanical properties, dissolution rates, biological activity, and bone formation potential. Added to this are the effects that the *in vitro* and *in vivo* conditions themselves have on the experimental results (e.g., the

same materials respond differently in different animal models (Yazdanpanah et al., 2022)). Confirmation of the possible causes explaining the observed differences between the materials in this study could be obtained from additional biological experiments involving gene expression analysis on the cultured cells in the neotissue or material tests such as X-ray diffraction to analyse material decomposition; however, this falls outside of the scope of this study.

This study provides additional experimental and numerical support for the current research focus on triply-periodic minimal surfaces in bone tissue engineering. This focus was inspired by the development of the relatively new field of curvature-based biology (see (Schamberger et al., 2023) and references within). In this field, the mechanistic underpinnings of the effect of local curvature on neotissue growth (linked to intercellular tensile forces) have been investigated in a range of materials and applications (Bidan et al., 2013; Buenzli et al., 2020; Bidan et al., 2012; Kommareddy et al., 2010; Callens et al., 2023). On the other hand, in the tissue engineering field, many studies address either theoretical aspects of the description of 3D structures (Callens et al., 2020) or focus on particular mechanical or mass transport (Hayashi et al., 2023; Li et al., 2022; Pires et al., 2022). This study sits at the interface between the aforementioned approaches, using a combined *in vitro–in silico* approach with a focus on the biological outcome. As such, it provides a clear basis for the further testing of these structures in *in vivo* settings (Van Hede et al., 2022).

3.6 Conclusions

In this study, a curvature-based tissue growth model was adapted for use in calcium phosphate 3D additively manufactured structures. After model calibration by a coupled *in silico–in vitro* approach, the final model's potential for simulating neotissue growth was demonstrated on a 3D gyroid scaffold. The *in silico* framework presented in this study has demonstrated its ability to be used as a tool for designing improved bone

tissue engineering scaffolds and can easily be extended with additional design features for other applications in the future.

CHAPTER 4

3D-Printed synthetic hydroxyapatite scaffold with *in silico* optimized macrostructure enhances bone formation *in vivo*

The candidate performed the *in silico* work reported in this study.

4.1 Abstract

3D printing technologies are a promising approach to treat intra-oral bone defects, especially those with poor regenerative potential. However, there is a lack of evidence regarding the impact of internal design specifications on the bone regenerative potential. Here, an *in silico* approach to optimize the internal design of Calcium Phosphate-based scaffolds for bone regeneration is proposed. Based on an *in silico* model of neotissue formation, a gyroid 3D-printed scaffold is designed and manufactured using UV stereolithography of bioceramic materials. An orthogonal lattice structure 3D-printed scaffold and a particulate xenograft are used as control groups. The scaffolds are implanted subperiosteally under a shell on rat calvarium for 4 or 8 weeks and bone neoformation performances are investigated by nanofocus computed tomography and decalcified histology. After 8 weeks, the gyroid group is associated with a higher ingrowth potential of the bone and is characterized by signs of osteoinduction (newly formed bone islands). The bone to material contact is similar between the gyroid and the particulate groups. The present results reinforce this *in silico* modelling strategy to design Calcium Phosphate-based 3D scaffolds and the gyroid experimental internal architecture seems to be highly promising for intra-oral bone regeneration applications.

4.2 Introduction

Despite being very common, intra-oral bone defects are still challenging clinical situations that can be lengthy to treat with often unpredictable outcomes owing to the lack of patient-customized treatment. Although particulate bone substitutes have demonstrated their efficacy in self-containing defects, they have shown limitation inherent to their lack in 3D stability in defects with poor regenerative potential. Alternatively, blocks of different sources (autologous or allogeneic cortical bone, xenogeneic and synthetic bone blocks) were tested in animals and humans with most of them displaying the main disadvantages of being shaped by hand to fit

the patient's bone defect and containing no or inappropriate interconnectivity for neovascularization, reducing their overall bone regenerative performances (Carrel et al., 2016; Giuliani et al., 2016; Sawada et al., 2018; Venet et al., 2017; Artzi et al., 2002; Spin-Neto et al., 2015). Nowadays, combination of several new technologies such as Computer-Aided Design–Computer-Aided Manufacturing, Cone Beam Computed Tomography and high resolution stereolithograhy (SLA) (Figliuzzi et al., 2013; Helal et al., 2019; Jacotti et al., 2014; Mangano et al., 2014; Mangano et al., 2015), enable the fabrication of patient-customized 3D scaffolds with tailored dimensions, shape, and internal design (Garot et al., 2019; Lin et al., 2019; Rider et al., 2018; Roseti et al., 2017).

The internal design together with the surface properties are two major factors influencing bone regeneration performances of 3D-printed scaffolds (Albrektsson et al., 2004; Gariboldi et al., 2015; Klenke et al., 2008; Lambert et al., 2017; Perez et al., 2016). Whereas the surface roughness depends on biomaterial composition and postproduction processes (sintering t°, coatings, etc.) (De Carvalho et al., 2019; Mealy et al., 2015), recent 3D printing technologies allow the manufacturing of custom-made scaffolds with a multitude of internal design. *In silico* modelling (the use of computer modelling and simulation) is a key approach to avoid the *in vivo* testing of numerous designs, in accordance with the 3 R's principle, by designing and selecting the most promising patterns according to the predictions established by the model. As the efficacy of bone regeneration is dependent of a number of parameters, the ideal model should consider as many of them as possible. Besides the well-studied factors (biochemical, physical, and surface properties), the effect of the 3D scaffold internal design is less explored although this parameter has an important impact on the tissue formation rate (Alias et al., 2017; Gamsjäger et al., 2013; Guyot et al., 2016; Rumpler et al., 2008; Werner et al., 2017). A variety of *in silico* bone regeneration models has been proposed in the literature (Wang et al., 2015), with most of them corroborated by comparison with historic or dedicated animal experiments. However, most of them focus either on scaffold-free

regeneration (Carlier et al., 2015) or a specific shape (Perier-Metz et al., 2020; Sandino et al., 2010; Sandino et al., 2011) rather than using the model to optimize the scaffold structure. *In silico* models focusing on optimizing scaffold internal design to maximize neotissue formation have primarily been corroborated by *in vitro* 3D cell culture experiments (Rubert et al., 2020; Guyot et al., 2016).

Previously, we developed an SLA-based approach to fabricate 3D-printed synthetic CaP scaffolds aiming to generate new bone while being biocompatible (Guéhennec et al., 2019). After assessing the cytocompatibility *in vitro* using MG-63 osteoblastic-like cells, our proof-of-concept was challenged in a subperiosteal cranial rat model using 3D-printed pellets displaying a simple macrostructure (rounded unidirectional channels). Although biocompatibility and biological performance were demonstrated, the tested scaffolds did not explore different 3D geometries. Based on the *in silico* modelling and using high resolution SLA 3D printers, the present study goes one step forward investigating the effect of complex and optimized scaffold on bone regeneration.

The objective of the present study was to reinforce our *in silico* modelling strategy by evaluating the *in vivo* biological performances of our optimized 3D-printed scaffold (gyroid) in a small animal bone augmentation model compared to a gold standard (granules of Bio-Oss) and a classic geometry (orthogonal).

4.3   Experimental section

4.3.1   *In silico* scaffolds design

In order to define the optimal scaffold geometry leading to maximal neotissue formation, a previously developed *in silico* model of neotissue growth was used (Guyot et al., 2014). Full details are provided in Chapter 3. Briefly, neotissue growth in porous scaffolds has been shown to be depending on the local mean curvature of the interface between the

scaffold and the neotissue (Rumpler et al., 2008; Bidan et al., 2012). The *in silico* model uses the level set method to implement this curvature-based growth through a simulation of the movement of the interface between the neotissue and the void space. The speed of the moving interface is made dependent on the mean local curvature, leading to an effective and efficient implementation of the curvature-based growth (Guyot et al., 2014). The model calibration performed in Guyot et al. was for titanium scaffolds culture in a bioreactor setting (Guyot et al., 2014). For the purpose of the present study, dedicated calibration experiments were performed on prismatic structures, demonstrating a considerably slower growth on the CaP scaffolds, nevertheless confirming the curvature-based nature of the growth. Neotissue growth was then simulated for a variety of lattice-based structures as well as structures from the triply periodic minimal surface (TPMS) family (Figure 4.1B,C) and compared in a qualitative way. A full quantitative prediction is not possible due to the absence of relevant validation experiments, which explains why comparisons between geometries are made over non-dimensional time. After identification of the gyroid-TMPS as the optimal structure, an additional analysis was carried out to investigate the pore size and wall thickness best suited to stimulate neotissue ingrowth by maximizing speed of growth as well as amount of neotissue formed, while taking into account restrictions of the manufacturing process in terms of smallest feature dimensions. The gyroid scaffold identified through this process was manufactured along with a lattice-based control.
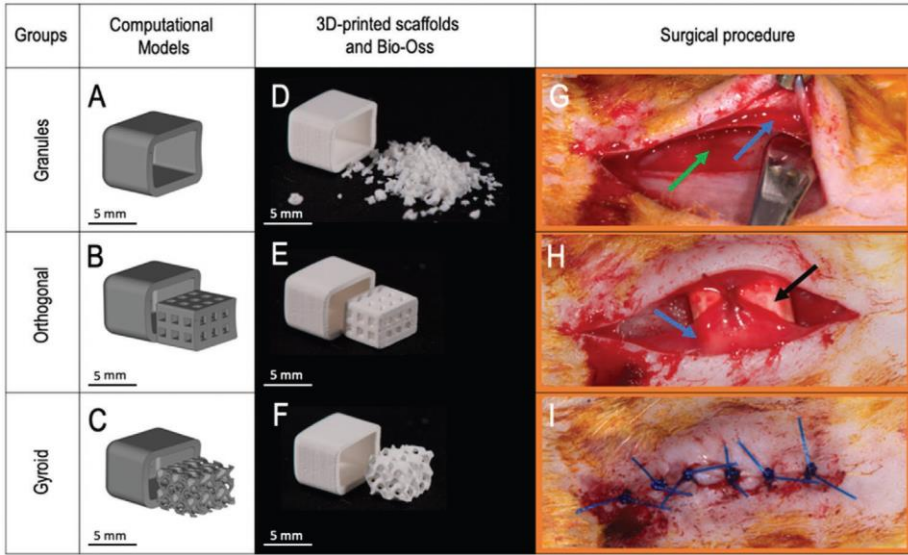
Figure 4.1: 3D designs based on the computational model, 3D-printed parts and surgical procedure. A–C) Gyroid structures were suggested by the *in silico* model and compared to a lattice-based orthogonal structure and the clinical gold standard. D–F) Shells and inserts were printed by stereolithography. G–I) The surgical procedure is depicted. Blue arrows: detached periost; green arrow: parietal bone; black arrow: scaffold.

4.3.2 Scaffold manufacturing

Orthogonal and gyroid inserts as well as shells were implemented in Netfabb by Autodesk (Figure 4.1A–C). They were produced using a SLA machine (Prodways V6000, France) and composed of hydroxyapatite as previously described (Figure 4.1D–F) (Guéhennec et al., 2019). Briefly, the bioceramic was carefully mixed with organic components (polyfunctional acrylic resins and UV-photoinitiator) in order to obtain a viscous paste material to be processed by SLA (Cerhum and Sirris, Belgium). The solid loading was $\approx 50\%$ for both formulations. During the process, the suspension was spread on the working area in thin layers of 50 µm. After spreading a layer, UV-light was projected by a digital light processing on the paste surface. The samples were then submitted to a thermal cycle (1125 °C, for 5 h) allowing the removal of the resin and the

densification of the ceramic (Goffard et al., 2013). After manufacturing, the parts were rinsed and ultrasonically cleaned in an ethanol 80% bath for 10 min. As a final step, they underwent autoclave sterilization (134 °C for 30 min) before *in vivo* implantation.

4.3.3 Physico-chemical characterization

Gyroids and orthogonal parts were analysed using a diffractometer (Rigaku Miniflex 600) in order to identify and quantify their mineralogical phases. Moreover, a qualitative analysis of their surface microtopography was carried out with a scanning electron microscope (SEM). Scaffolds were mounted on SEM stubs and coated with platinum using a Q 150T S sputter coater (Quorum Technologies, West Sussex, UK). The sample surface analysis was performed using a Quanta 250 FEG-SEM. Additional analyses (Compressive strength, BET, and degradation tests) are presented in the Appendix D.

4.3.4 *In vivo* implantation

4.3.4.1 Animals and study design

Subperiosteal implantation of the scaffolds was performed in a calvaria rat model in order to determine the impact of the scaffold internal design on the bone augmentation performances *in vivo*. All experimental procedures used in this investigation were reviewed and approved by the Institutional Animal Care and Use Ethics Committee of the University of Liège, Belgium (ethical number 1527). Animal Research Reporting of *In vivo* Experiments guidelines were carefully followed as well as national and European legislation (Kilkenny et al., 2012). The male Wistar rats were acquired from the University of Liège and randomly allocated into six groups (three experimental scaffolds: granules, orthogonal, and gyroid; two time points: 4 and 8 weeks).

4.3.4.2   Global scaffold design

Scaffolds were produced in two parts, an insert (3.4 mm in length, 5.1 mm in width and 4 mm in height) and a shell (6.5 mm in length, 5 mm in width and 5 mm in height, 0.7 mm wall thickness), with their respective dimensions allowing a perfect assembly of the insert into the shell. To play the role of a barrier and allow bone ingrowth exclusively from the calvarium, the shell was not perforated (Figure 4.1A–F). In addition, both inserts and shells displayed a slight curvature on their lower side to best fit the animal's skull. Shell design was identical for the three groups both types of scaffolds. The insert designs corresponded to a lattice structure with square struts (orthogonal group, pores diameter of 700 μm) or a gyroid structure (gyroid group, pores diameter of 700 μm) while in the granule group the particles diameter ranged from 0.25 to 1 mm (Bio-Oss, Geistlich, Wolhusen, Switzerland).

4.3.4.3   Surgical procedure

Animals were anaesthetized with a combination of Ketamine (8 mg/kg) and Xylasine (5 mg/kg) administered intraperitoneally, the surgical site was shaved and few blood drops were collected from the tail extremity. Following a local administration of anaesthetic (Septanest special, Septodont, France), an antero-posterior incision was performed on the calvarium. A full thickness skin flap was raised in order to exhibit the entire parietal bone (Figure 4.1G). Before implantation, the Bio-Oss particles were mixed with the collected blood while the inserts were filled in with it. The experimental specimens were then placed into a shell and a single scaffold was implanted over the sagittal calvarial suture in each animal according to the randomization (Figure 4.1H). The surgical site was sutured with polypropylene 5/0 (Permashap, Hu Freidy, USA) (Figure 4.1I). Antibiotics (Baytril, 5 mg/kg), painkillers (Temgésic, 0.05 mg/kg) and anti-inflammatory (Rimadyl, 5 mg/kg) drugs were administrated subcutaneously. After 4 and 8 weeks, rats were euthanized by an overdose of pentobarbital (euthasol). The samples were harvested

and fixed for 24 h in 4% formaldehyde and then stored in PBS at 4 °C until Nano-CT acquisition.

4.3.4.4 Nanofocus computed tomography

Nano-CT scans of the samples were acquired using the GE Phoenix Nanotom (Hawker Richardson, New Zealand). Scanning was carried out at 75 kV, 140 μA, and with a 0.5 mm aluminium filter. A total of 1800 images were taken over a 360° scan using the fast scan mode with a resolution of 5.5 μm per voxel. Scans 3D reconstruction was performed using Phoenix datos|x CT and then reoriented adequately with DataViewer (Bruker micro-CT, Kontich). Using the same software, the experimental inserts were selected excluding the shell. The selected volume (total volume, VOI1) was then quantitatively analysed with CTAn (Bruker micro-CT, Kontich). The quantity of newly formed bone was determined using a segmentation based on the grey levels. The percentage of bone was then calculated within the VOI1 as follows:

$$\text{Bone within VOI1 (\%)} = \frac{\text{(Volume of Bone)}}{\text{VOI1}} \times 100$$

Additional methodologies for bone volume quantification are presented in the Appendix E.

As not only the quantity of bone, but also the ingrowth into the scaffold is of importance, the distance between the parietal bone and the highest point of newly formed bone within the 3D scaffolds was measured in all samples as follows:

$$\% = \frac{\text{Highest point of Bone}}{\text{Total height of the scaffold}} \times 100$$

4.3.4.5 Qualitative histological analysis, blood vessels quantification, and bone to material contact calculation

Following a decalcification procedure of two days using a mixture of hydrochloric acids (DC2, VWR, USA), the samples were embedded in

paraffin. Five µm-thick longitudinal sections were obtained from three different levels of the samples and stained with hematoxylin and eosin. Additionally, a fourth section was used to assess the blood vessels invasion. These sections were heated in EDTA buffer and incubated with an anti-CD34 antibody (1/2500, ab81289, Abcam). Goat anti-Rabbit–HRP antibody was used as the secondary antibody at 1/500. The histological sections were then scanned (NDP NanoZoomer Digital Pathology, Hamamatsu, Japan) and a descriptive analysis was performed regarding the global inflammation and bone localization (NDPView2, Hamamatsu). Neoangiogenesis was quantified according to the area occupied by blood vessels and to their density using a semi-automatic method with the software ImageJ (Schneider et al., 2012). Finally, for the eight weeks samples, the percentage of bone to material contact (BMC) was calculated in areas where newly formed bone was present as follows:

$$BMC\,(\%) = \frac{\text{Perimeter of Biomaterial in contact with Bone}}{\text{Total Perimeter of Biomaterial}}\,X\,100$$

4.3.5   Statistical analysis

4.3.5.1   Sample size calculation

The required sample size was determined using the software Gpower (Faul et al., 2007). The effect size was set at 0.55 and the power at 0.95. Thus, the calculated total sample size was 55 but it was rounded up to 60 according to the study design (six groups with ten animals per group).

4.3.5.2   Statistical tests

Statistical tests were carried out using GraphPad 8.3.0. Normality tests (D'Agostino & Pearson) were performed following outliers' identification (ROUT test with Q = 1%) and withdrawal. The blood vessels invasion (Area and Density) was analysed using a Two-Way ANOVA, the percentage of BMC was analysed using a One-Way ANOVA whereas a Mixed-effect model (REML) was used to analyse the % of bone within the VOI1 and the highest point of newly formed bone. Tukey's and Sidak's corrections were

applied for multiple comparisons. The data were presented as violin plots with quartiles and medians.

4.4   Results

4.4.1   *In silico* modelling

A previously developed *in silico* model, simulated neotissue growth by using a level-set method (Guyot et al., 2014). This means that the interface between the neotissue and the empty space is advected with a certain speed. In this study, as Guyot et al., that speed was dependent on the local curvature of the substrate. Neotissue growth was simulated for a variety of lattice-based and TPMS structures. Combining the results of this simulation with the superior printability of the gyroid-TPMS, this structure was further investigated in a second round of *in silico* modelling. There, we investigated the effect of its pore size and wall thickness, in order to obtain the combination leading to optimal neotissue growth. Pore size was varied between 700 µm and 1.3 mm and wall thickness was varied from 200 to 800 µm (Figure 4.2), which are ranges that take into account restrictions of the manufacturing process in terms of smallest feature dimensions. Balancing the need for swift neotissue ingrowth (Figure 4.2B, relevant for short-term implant stability) with the volume of neotissue formed (Figure 4.2A, relevant for long-term implant stability), the combination of 700 µm pore size and 200 µm wall thickness (Figure 4.2C) was chosen as the optimal structure to continue with the experimental part of this study.
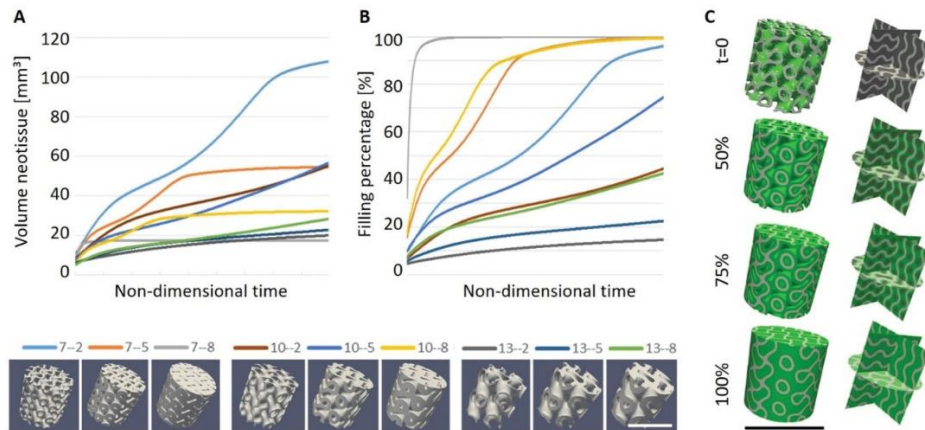
Figure 4.2: *In silico* predictions of neotissue formation. Neotissue formation quantified in A) absolute volume and B) filling percentage for cylindrical test samples (ø 6 mm, height 6 mm). The different combinations are indicated in the legend by 2 numbers, the first of which refers to pore size (7: 700 µm, 10: 1 mm, 13: 1.3 mm) and the second refers to wall thickness (2: 200 µm; 5: 500 µm; 8: 800 µm;). C) Side view and cross-sectional view of neotissue growth in gyroid (7–2) scaffold for different levels of filling, starting with initial condition at t = 0 (top). Scale bars: 6 mm.

4.4.2 Physico-chemical characterization

Orthogonal and gyroid inserts were composed of $\approx 94\%$ of $Ca_5(PO_4)_3(OH)$ (hydroxyapatite) and 6% of $\beta\text{-}Ca_3(PO_4)_2$ (β-TCP) whereas $\alpha\text{-}Ca_3(PO_4)_2$ (α-TCP) was undetectable. From a qualitative point of view, SEM analysis revealed similar surface roughness of both 3D-printed scaffolds whereas more microporosities were observed for the granules group (Figure 3).
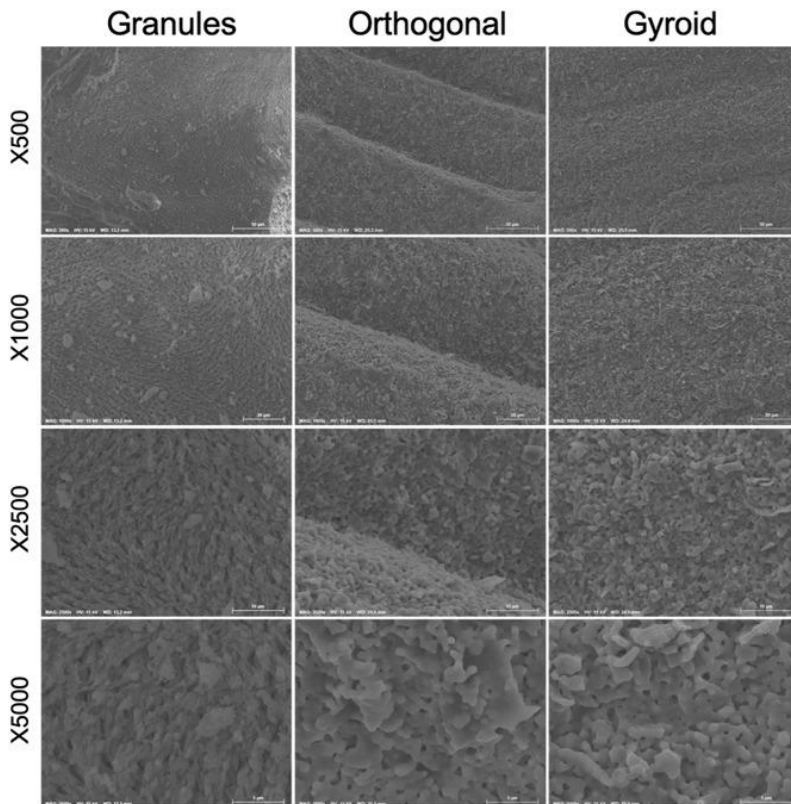
Figure 4.3: SEM analysis. Surface topographies of the three biomaterials are shown at different magnifications.

4.4.3 *In vivo* implementation

4.4.3.1 Nano-CT analysis

The percentage of newly formed bone (Bone) within the total volume (VOI1) was similar between the three groups at 4 weeks but was higher in the gyroid group at 8 weeks compared to the granules and the orthogonal groups ($p < 0.0001$) (Figure 4.4A). Moreover, the percentage of Bone increased with time for the granules ($p < 0.05$) and the gyroid ($p < 0.0001$) groups but was stable for the orthogonal group. Additional output measures were carried out but did not change the overall conclusion (Appendix E). At 8 weeks, the highest point of Bone was superior for the

gyroid group compared to the granules and the orthogonal groups (p < 0.0001) (Figure 4.4B). Moreover, at 4 and 8 weeks, it was higher for the orthogonal group compared to the granules group (p < 0.05). This parameter did not evolve with time in the granules and the orthogonal groups but increased in the gyroid group (p < 0.0001). Interestingly, when looking at these highest points of newly formed bone within the 3D-printed scaffolds, we observed that most of them formed self-standing islets of bone, in the gyroid group in particular.
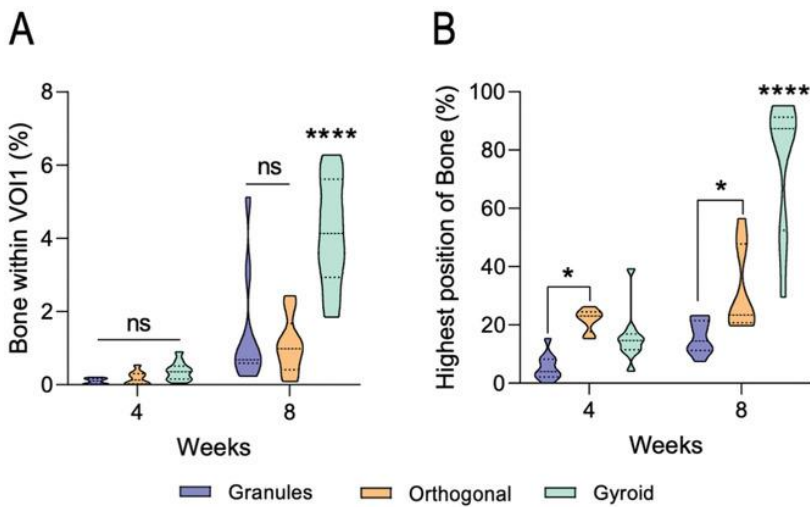
Figure 4.4: Bone regeneration analysis by Nano-CT. The percentages of newly formed bone between the granules, the orthogonal and the gyroid groups were determined A) within the VOI1 at 4 and 8 weeks. B) The bone highest position was calculated at 4 and 8 weeks. ns = not significant; * = p < 0.05; **** = p < 0.0001.

4.4.3.2   Histological descriptive analysis, blood vessels quantification, and BMC

At 4 weeks, the scaffolds in all three groups were mainly colonized by soft tissues. Remaining blood clots were observed mostly in the centre and the highest areas of the scaffolds. Blood vessels were present in each sample. Few inflammatory cells were noticed in some samples. Early bone

colonization, characterized by woven bone and starting from the calvarium, was observed in all the 3D-printed samples but only in some of the granules group. At 8 weeks, the amount of bone inside the scaffolds increased, especially in the 3D-printed scaffolds. Moreover, islets of bone were observed at the distal portion of the scaffold in almost all gyroid group samples. Overall, no major signs of inflammation were highlighted among the investigated groups (Figure 4.5).
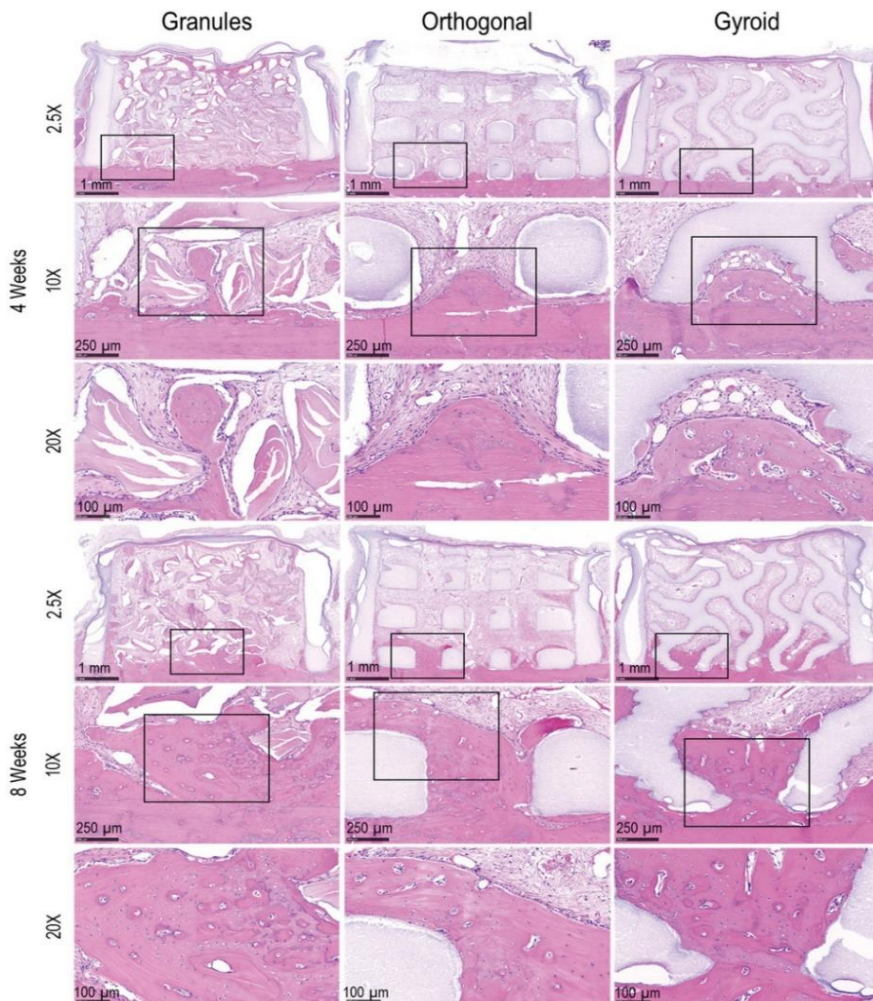
Figure 4.5: Representative histological sections from the three experimental groups at 4 and 8 weeks. At 4 weeks post-implantation, the low magnification pictures (2.5×) allowed to visualize a low, localized but similar new bone

formation between each of the three experimental groups. At 8 weeks, bone formation was still localized in the granules group whereas the 3D-printed scaffolds displayed a widespread bone colonization (low magnification pictures).

Neoangiogenesis is an important process that occurs in the early phases of bone formation. Therefore, the area occupied by blood vessels as well as the blood vessel density were quantified. The Area occupied by blood vessels decreased over time ($p < 0.05$) but no specific difference within groups was found (Figure 4.6A). Also, regarding the blood vessels density, the orthogonal group displayed less vessels compared to the granules group at both 4 and 8 weeks ($p < 0.05$) (Figure 4.6B) but no difference was found between the granules and the gyroid groups.
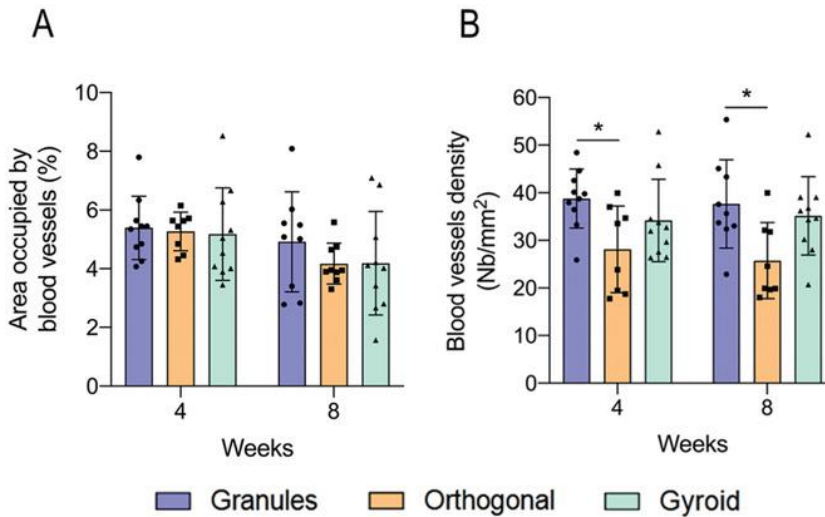
Figure 4.6: Blood vessels quantification. Area occupied by blood vessels (A) and Blood vessels density (Nb mm−2) were quantified on sections at 4 and 8 weeks post-implantation in the granules (n = 10 and n = 9), orthogonal (n = 8 and n = 9) and gyroid (n = 10 and n = 10) groups. Both parameters were obtained by using a semi-automatic method with the software ImageJ on 40× scanned sections stained with an antibody anti-CD34 marker. * = $p < 0.05$.

As the Nano-CT analysis revealed weak rates of bone regeneration and highlighted no difference between the groups at 4 weeks, the BMC was not

determined for this time point. At 8 weeks, the BMC was superior for the gyroid group compared to the orthogonal group ($p < 0.05$), with a distribution between $\approx 30\%$ and 50%, and a median of 40%, whereas the orthogonal group displayed a more scattered distribution (10 to 50%) and a median inferior to 20%. No difference between the granules and the gyroid groups was highlighted (Figure 4.7).
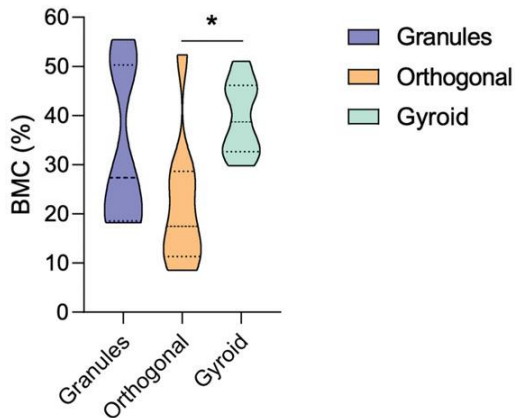
Figure 4.7: The BMC at 8 weeks. The percentages of BMC were calculated using the 8 weeks histological sections. * = $p < 0.05$.

4.5   Discussion

This study demonstrates that our 3D-printed HA scaffolds with *in silico*-optimized internal macro-porous architecture (gyroid group) enhanced bone neoformation in a subperiosteal bone augmentation calvarial rat model and, therefore, corroborates the *in silico* model in its qualitative prediction of neotissue growth acceleration between different structures. Although the scaffolds from the three groups showed similar mineral composition and surface roughness, *in vivo* results highlighted a superior bone regenerative potential in the *in silico* optimized gyroid group (amount and height).

In silico modelling is widely used for tissue engineering as it offers a more exhaustive approach compared to a "trial-and-error" method and reduce

the number of experimental tests. Optimization of scaffold structures for bone tissue engineering purposes is often corroborated by comparison with *in vitro* tests (Guyot et al., 2016; Rubert et al., 2020) and only a small number of *in vivo* studies have been reported (Long et al., 2012; D. Luo et al., 2017; X. Luo et al., 2015). However, in these *in vivo* studies, optimization was first performed on mechanical properties rather than the structural elements such as local curvature underlying the *in silico* model used this study.

HA was chosen to fabricate the 3D-printed scaffolds because among the various CaP ceramics, HA is the least soluble, providing a long term 3D stability of the regeneration, and is known to be highly biocompatible as its composition is similar to the natural bone matrix (Dorozhkin & Epple, 2002). Thanks to its different properties, this CaP ceramic is a widely used synthetic bone substitute for bone regeneration procedures (Jeong et al., 2019). Nano-CT and histological analysis of the *in vivo* ectopic implantation data showed that none of the scaffolds underwent a substantial resorption over the experimentation follow-up period as expected from the HA material used in this study (Dorozhkin & Epple, 2002). The physico-chemical analyses showed that, in all experimental 3D-printed scaffolds, a small portion of HA (6%) was transformed in β-TCP which is most likely induced by the sintering process. The presence of β-TCP, being more soluble, may actually play a role in the regenerative process by releasing Ca+ ions in the environment and contribute to the bone forming process (Harding et al., 2005). The relatively low sintering temperature used in the present study allowed to produce experimental scaffolds with a surface topography rather close to the natural bone surface characteristics favourable for cell adhesion, anchoring, and proliferation (Andrukhov et al., 2016; Fellah et al., 2008; Le Guéhennec et al., 2019).

In vivo results obtained from the Nano-CT analysis highlighted the superior bone regenerative potential of the gyroid design with more newly formed bone inside the scaffold, especially in the highest parts of the scaffolds. This result emphasized, besides the pore size parameter, the

critical role of the pore geometry and orientation when designing 3D scaffolds for bone regeneration applications (Boccaccio et al., 2016; Van Bael et al., 2012; Zadpoor, 2015). Indeed, whereas cell growth preferentially occurred within highly curved pore corners, tissue growth is favoured within pores displaying numerous corners such as hexagons compared to rectangular and triangular pores (Van Bael et al., 2012). Moreover, pore orientation may also influence bone regeneration (Jones et al., 2009; Liu et al., 2013; Serrano-Bello et al., 2020). The orientation of the gyroid structure, with waved channels running from the parietal bone to the top of the insert, might have allowed for a curvotaxis-type of migration of progenitors into the insert (Pieuchot et al., 2018). Finally, the screening of the 3D volumes of each sample revealed the presence of independent bone islets in most of the 8 weeks gyroid samples solely. This observation may suggest that this particular design harbour some osteoinductive capacity which is in accordance with previous works highlighting the effect of pore interconnectivity on bone ingrowth (Habibovic et al., 2005, 2006; Jones et al., 2009). Additionally, having even isolated islands of bone formation at all levels throughout the implant scaffold, will be beneficial for follow-up actions such as oral implant osseointegration.

The histological analysis revealed no signs of inflammatory reactions neither at 4 weeks nor at 8 weeks of implantation in any of the three experimental groups, indicating that the manufacturing process and post-manufacturing treatment produced biocompatible 3D-printed scaffolds as previously described (Le Guéhennec et al., 2019). On the other hand, histological sections displayed a decreased percentage of the area occupied by blood vessels over time, showing that the bone regenerative process was ongoing between 4 and 8 weeks post-implantation, although no difference between the designs was found. Also, the differences observed in terms of blood vessels density between the designs highlight the importance of internal design to improve bone regeneration through an enhanced neoangiogenesis. Indeed, previous reports indicated that optimal blood vessels neoformation occurs in macro-pores characterized by a diameter ranging from 100 to 800 μm, depending on the

experimental conditions (Cheng et al., 2016; De Wild et al., 2018; El-Rashidy et al., 2017; Hulbert et al., 1970; Roosa et al., 2010). As neoangiogenesis occurs at an early phase of the bone regenerative process, it would be interesting to evaluate the influence of the biomaterial design on the blood vessels invasion during the first two weeks post-implantation.

Finally, the interface between the newly formed bone and the biomaterial surface (BMC) was equivalent in the gyroid and the granules groups while less contact was found in the orthogonal group. If surface topography was often correlated to the degree of osseointegration of regenerative materials (Lambert et al., 2017; De Carvalho et al., 2019; Denry et al., 2016), the present results suggest that additional characteristics such as the pore size, geometry, and orientation may also play a role in the osteoconduction process.

Taken together, the present results emphasize the excellent biological performances of the 3D-printed scaffolds and the better performance of the gyroid design supporting the role that *in silico* modelling can play in designing optimized macro-porous architectures of cell-free scaffolds for bone regeneration.

However, our study encounters some limitations that should be underlined. Simulation results have been used in a qualitative way after the curvature-based growth principle was confirmed in dedicated *in vitro* tests but without aiming to provide a detailed quantitative prediction of the actual *in vivo* experiment. Using the proposed *in silico* model in a quantitative way requires a substantial amount of data to fully validate the model (Erdemir et al., 2020; Pathmanathan et al., 2019; Patterson & Whelan, 2017). Additionally, the current version of the neotissue model was developed to assess neotissue formation in *in vitro* conditions with uniform cell seeing, leading to the uniform filling observed in Figure 4.2C. It does not allow to capture fully the neotissue growth *in vivo* due to the absence of directional migration and osteogenic differentiation in the modelling framework. However, as both directional migration (Pieuchot et al., 2018) and osteogenic differentiation (Werner et al., 2017) have been shown to be positively influenced by local curvature, adding these

elements to the modelling framework would not alter the conclusions. The experimental results generated in this study can now serve to further validate the *in silico* model so that it can develop into a stand-alone tool for quantitative *in vivo* neotissue formation prediction. For manufacturing reasons, while pore diameter was standardized, pore struts differed between the 3D-printed scaffolds, leading to orthogonal scaffolds with larger struts and thus fewer empty spaces for bone neoformation compared to the gyroid group. This limitation was mitigated by normalizing the VOI2 in each group using the VOI2 of the granules group as reference (Appendix E). Because of the global dimensions of the scaffolds, it was not possible to implant more than one scaffold per animal, resulting in an uncontrolled inter-animal variation. However, this weakness was compensated by the high study power (n = 10 for every time point in every group). Finally, and in order to enhance the standardization of the animal experimentation, instead of the usual collagen barrier membrane, a rigid HA-based shell was used to limit the ingrowth of soft tissue into the scaffold. However, this is not fully representative of the clinical application and similar experiments on bigger animals would be necessary in order to validate such a treatment concept in more realistic conditions.

4.6   Conclusion

Within the limits of the present study, we demonstrated that *in silico* model facilitates the internal design optimization of 3D-printed scaffolds for bone regeneration applications. The gyroid design, identified by using *in silico* modelling, displayed better regenerative performance compared to the gold standard or the orthogonal printed structures. Using the modelling results, we were able to limit the amount of conditions tested *in vivo* to one gyroid design and two controls rather than multiple gyroid designs. With the excellent bone regenerative performances obtained in the present study, we hope to encourage regenerative medicine research to adopt a similar approach and avoid unnecessary animal

experimentation. However, further developments in larger animal models are necessary to translate this concept to clinical practice.

CHAPTER 5

Application of curvature-driven neotissue growth model in 3D structures for *in vivo* applications

As can be appreciated from the comparison between simulation results and *in vivo* results in Chapter 4, a number of challenges remain with respect to adequately capturing the neotissue growth dynamics of the *in vivo* situation. In this chapter, we use the model developed in Chapter 3 and applied in Chapter 4, and look into to various elements that are important when simulating *in vivo* applications, from gradient scaffolds to neotissue ingrowth. The introductory part of this chapter describes the differences between *in vivo* and *in vitro* environments and suggests directions for improving scaffold architecture and model setup. The purpose of the research in this chapter is stated in Section 5.2. Section 5.3 describes, amongst others, the generation of different 3D scaffolds. The generated scaffolds are used in model simulations to test simplified ways of capturing *in vivo* tissue formation and ingrowth. The simulation results and discussions are presented in Sections 5.4 and 5.5, respectively.

5.1 Introduction

In Chapter 3, we constructed 2D and 3D scaffold models based on calcium phosphate biomaterials. Through a series of *in vitro* experiments, we precisely determined a crucial parameter within the model, namely, the growth rate control parameter (referred to as velocity control A). The experimental focus in Chapter 3 primarily centred on the effect of basic shape geometries on the neotissue growth (both in terms of quantity and quality), to calibrate this parameter. Using this calibration, the model's behaviour in predicting 3D neotissue growth in a gyroid structure (with 900 μm pore size and 200 μm wall thickness) was tested. The model was able to capture the overall process of neotissue growth on the 3D structure, demonstrating a seamless transition of the model from 2D to 3D.

Nevertheless, the current model possesses a limitation whereby cells are assumed to be uniformly distributed on the scaffold's surface at the start of the simulation. This is appropriate for *in vitro* situations where a homogenous cell density is ensured throughout the scaffold at the start of the experiment. This is not realistic for biomaterial-based *in vivo* experiments, such as those executed in Chapter 4, where cells need to be attracted from the host environment. Furthermore, due to mechanical considerations (amongst others), a homogeneous porosity and resulting homogeneity in mechanical properties might not be desired. As an example, when creating maxillofacial implants, some regions in a mechanically more loaded environment might require a higher apparent stiffness of the implant. The exploratory research in this chapter will provide us with tangible handles on further limitations and possible future extensions of the model.

5.1.1 Differences between *in vivo* and *in vitro* environments

There are essential differences in the process of neotissue growth under *in vivo* and *in vitro* culture conditions, and these differences arise from the complexity of the surrounding environment and the diversity of cellular

interactions (Antoni et al., 2015). Cells are regulated by biological signals, including growth factors, cytokines, and hormones, which can affect cell proliferation, migration, and differentiation (Bottaro et al., 2002. *In vivo*, these signals originate from surrounding cells and tissues, forming a complex cellular microenvironment (Metallo et al., 2007). Cells often interact with neighbouring cells, and this cell-cell interaction regulates cell behaviour through cell adhesion, intercellular communication, and signalling (Collins et al., 2015). Cells also interact with the scaffold in a process that involves, amongst others, proteins adsorbed to the scaffold's surface connecting to cell surface molecules such as integrins. In the case of Calcium Phosphate-based biomaterials, a relationship exists between the physico-chemical characteristics of the initial powders and the final biological response to the sintered ceramics prepared from these powders. An inverse relation exists between the specific surface area and protein adsorption capacity of the powder on the one hand and the protein adsorption and cell attachment on the sintered ceramics on the other (Rouahi et al., 2006). The cells' response to the surrounding environment is not only affected by biological signals or the scaffold surface but also regulated by factors such as mechanical forces, oxygen concentration, and nutrient supply, which are much less controlled *in vivo* than in *in vitro* static or dynamic set-ups (Pampaloni et al., 2007).

In *in vitro* culture set-ups, researchers have greater control over laboratory conditions, including culture medium composition and temperature (Griffith et al., 2006). However, *in vitro* cultures often lack the complex biological signals found *in vivo*, so researchers need to add these signals to mimic the *in vivo* environment (Rossi et al., 2018). Furthermore, in *in vitro* environments, cells are typically grown on flat growth surfaces, lacking the complexity of the *in vivo* three-dimensional environment (Xu et al., 2014). Typically, *in vitro* cultures contain only a single type of cell strain or cell line, which limits the complex interactions between different cell types (Jensen et al., 2020). While 3D cell culture and the use of dynamic set-ups (bioreactors) can address some of the limitations of static 2D cell culture, such as providing a structure closer to that of the *in vivo* environment and allowing for cell interaction with the

3D matrix and a dynamic microenvironment, it still cannot fully replace *in vivo* research (Ravi et al., 2015).

5.1.2   Growth patterns of neotissue in alveolar bone

In vivo, the scaffold is implanted into the (alveolar) bone defect area. Cells will migrate to the scaffold surface from surrounding tissue and blood. These cells include immune cells, endothelial cells and osteochondral progenitor cells, which all play an important role in the bone regeneration process. Once cells contact the scaffold surface, they adhere to the scaffold through (through proteins as explained above) interactions and begin to spread to cover the scaffold surface (Salgado et al., 2007). Cells will continue to proliferate on the surface of the scaffold, filling the empty areas on the scaffold until confluency is reached (Liao et al., 2004). As cell density increases, interactions between cell populations drive the proliferation of the cells. Once cell density reaches a certain level, cells usually stop proliferating. This is due to the phenomenon of contact-inhibition.

At the same time, cells begin to secrete collagen and other extracellular matrix components (Raggatt et al., 2010). These substances accumulate on the surface of the scaffold and form primary bone tissue. Osteoclasts resorb some of the initial bone tissue and osteoblasts secrete new bone matrix. This process is called bone remodelling. The entire bone regeneration process usually takes time until the newly formed bone tissue can completely replace the initial bone tissue formed inside the scaffold. This process is also affected by other biochemical and biomechanical factors in the body, including blood supply, immune response, etc (Robling et al., 2006).

Normally, after scaffold implantation, the distribution of cells in the alveolar bone at the bone defect site will show certain spatial heterogeneity. This spatial heterogeneity results in a relatively high density of cells near the bone defect and a lower density away from the bone defect (Huang et al., 2015). The Calcium Phosphate scaffold material

itself has a certain biological activity and can interact with surrounding tissues. This interaction can result in the release of chemokines by various inflammatory cells after contact with the Calcium Phosphate scaffold material, which can attract cells to colonize and grow. Therefore, in the area near the direct contact surface of the scaffold, cells are more likely to migrate there due to the influence of chemokines, resulting in an increase in density. Nutrients and oxygen from the blood are normally supplied to the tissues through blood vessels (Velard et al., 2013).

Moreover, due to the effect of chemokines on blood vessel formation, more blood flow is supplied to these areas, and cells can obtain more nutrients, so cells are more likely to accumulate in this area, resulting in higher density. This gradient distribution of cell density helps promote the activity of bone cells and the bone regeneration process on the surface of the scaffold while also encourages bone tissue to adapt to the environment near the scaffold gradually. Scaffold design and treatment protocols often consider this cell density gradient to promote overall regeneration and healing of bone tissue (Huang et al., 2005).

5.1.3 Advantages of TPMS structures in scaffold design

Designing bone regeneration scaffolds involves several critical mechanical principles to ensure effective support for bone healing and integration. The scaffold must possess adequate strength and stiffness to handle physiological loads and support bone regeneration, including sufficient compressive and tensile strength to prevent breakage or deformation (Abbasi et al., 2020; Li et al., 2020). The porosity and pore structure of scaffolds are crucial, with optimal pore size and connectivity facilitating cell infiltration, vascularization, and new bone growth, while balancing mechanical strength (Collins et al., 2021; Mohammadi et al., 2021; Loh et al., 2013; Zhen et al., 2010). The degradation rate of the scaffold material must align with the rate of bone formation to provide adequate support throughout healing (Liu et al., 2004; Patterson et al., 2010). Load distribution must be evenly managed to avoid stress concentrations that could impair scaffold integrity or surrounding bone tissue (Leong et al.,

2008). Materials used should have mechanical properties similar to natural bone to ensure functional support, with advanced manufacturing techniques like 3D printing enabling precise design and structure (Feng et al., 2023). Overall, integrating these mechanical considerations—strength, stiffness, porosity, degradation rate, load distribution, material selection, and design optimization—is essential for creating an effective scaffold for bone regeneration (Egan et al., 2019).

The Triply Periodic Minimal Surface (TPMS) scaffold is a porous scaffold structure with some special geometric and physical properties that can affect the growth and differentiation of cells in the body (Dong et al., 2021). The pore structure of TPMS scaffolds has a highly regular geometric shape, usually consisting of mathematically rigorously defined curved surfaces. These geometric shapes include some well-known mathematical surfaces, such as Gyroid, Schwarz D, etc., which are characterized by minimum surface area (Kapfer et al., 2011). This regular pore structure helps cells arrange in an orderly manner within the scaffold, affecting cell growth and differentiation. The pore structure of the TPMS scaffold has a high specific surface area, meaning that a relatively small volume can provide a large amount of surface area. This is essential for cell attachment, exchange of nutrients, and diffusion of oxygen (Pugliese et al., 2023). The high surface area helps support the growth and activity of large numbers of cells. TPMS scaffolds are porous, meaning they have many tiny pores and channels. This porosity is similar to natural tissues such as bone and spongy bone, helping to mimic the microstructure of natural tissues. Porous scaffolds can provide the microenvironment required for growth and differentiation (Melchels et al., 2010). The structures of TPMS scaffolds usually have self-similarity, which means that their structures have similar geometric characteristics, whether they are scaled up or down. This self-similarity contributes to the predictability and controllability of the scaffold, making it a beneficial tool for engineering design. TPMS scaffolds are periodic, meaning their structure repeats with a certain pattern in space. This periodicity can be precisely described mathematically, making scaffold preparation and research more accessible (Feng et al., 2021). TPMS scaffolds usually have mechanical

properties that are sufficient to provide support and structural stability (Bouakaz et al., 2023). The mechanical properties of the scaffold can influence how cells perceive and respond to mechanical stimuli (Qiu et al., 2023). Some TPMS scaffold designs include gradient structures, where the size, shape, or density of pores inside the scaffold changes with position. This gradient structure can simulate the microenvironmental differences in tissues *in vivo*, thereby promoting the directional growth and differentiation of cells (Kanwar et al., 2022).

5.1.4   Gradient structures in skeletal tissues

In alveolar bone, a gradual decrease in bone density from the alveolar ridge (the outer edge of the alveolar bone) to the base of the alveolar bone can be observed (Figure 5.1). This density gradient helps the teeth stay securely in their sockets and provides proper support and stability (Kim et al., 2015). The porosity in alveolar bone varies between different regions. For example, areas near the alveolar ridge have lower porosity, while areas near the alveolar base have higher porosity (Shahlaie et al., 2003; Zamani et al., 2020; Xiao et al., 2022; Goldberg et al., 2022). Matrix components in alveolar bone, such as collagen and minerals, vary between regions, creating a gradient structure. Changes in this matrix composition can affect bone tissue's mechanical properties and bioactivity.
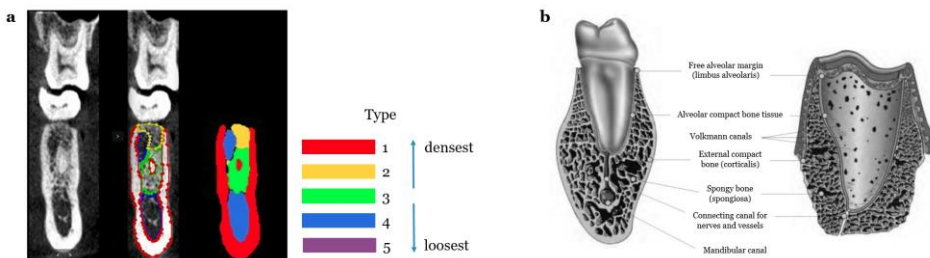
Figure 5.1: Gradient distribution of alveolar bone density and structural diagram. (a) Bone mineral density profile and recognition effect diagram. This image illustrates how an AI-based deep learning classification method determines bone density levels at implant sites using ray data from cone beam computed tomography images. From left to right: original image, doctor annotations, and

model recognition results. Red, yellow, green, blue, and purple represent bone densities from most dense (Type 1) to most porous (Type 5) (Image source: Xiao et al., 2022). (b) Schematic of the posterior mandibular alveolar bone. This diagram shows the alveolar bone density and structure in different areas, highlighting features such as cancellous bone, cortical bone, and vascular channels. It emphasizes the gradient distribution of alveolar bone, aiding in understanding its functional variations in supporting dental implants and providing clinical guidance (Image source: Goldberg et al., 2022).

Usually the cell density is higher at the outer edge of the alveolar bone tissue. This is because the alveolar ridge needs to provide support and stability to the teeth, so more cells are needed to maintain the integrity of the bone tissue. Areas near the alveolar base have lower cell density, as in these areas, bone tissue typically does not need to withstand the greater forces associated with chewing and biting, so there are fewer cells to maintain it (Djomehri et al., 2015). Between the alveolar ridge and the alveolar floor, there is a transition zone with a gradual change in cell density. This transition zone generally contains different types of cells to suit different functional needs. If there is an injury to the alveolar bone or the need for repair, cell density may increase significantly at the injury site to support the healing and repair process (Fiorellini et al., 2015).

These gradient structures are very important for scaffold design and bone tissue engineering because they can help stimulate the microenvironmental differences of bone tissue *in vivo* and promote the directional growth and differentiation of cells, thereby enhancing bone regeneration and repair (Afshar et al., 2016). Designing the scaffold with these gradient structures in mind will better simulate the complexity of the alveolar bone tissue.

5.2 Objective of this study

The central objective of this chapter is to understand the possibilities and limitations of the current *in silico* model in capturing conditions found within *in vivo* regeneration. This endeavour is directed towards providing

more precise guidance and predictions for extensions of the *in silico* model and its applications in modelling *in vivo* of bone regeneration.

5.3 Materials & Methods

The selection of scaffold materials in this study is based on the results obtained from the *in vitro* and *in vivo* experiments presented in Chapter 3 and Chapter 4 and the foundations laid by the model explained in Chapter 3.

In this chapter, we continue employing calcium phosphate as the scaffold material but will perform an *in silico* study to test various (gradient) geometries and seeding conditions as detailed in the sections below. Regarding the optimization of scaffold pore size and porosity, our focus has been on investigating two specific configurations (similar to previous chapters): TPMS structures with larger pores with a diameter of 1 mm and TPMS structures with smaller pores with a diameter of 0.7 mm, both featuring a wall thickness of 0.2 mm. Lattice structures with similar properties are used as control. In the design of gradient pore structures, we have considered two distinct types of density gradients. The first type involves a gradient variation in wall thickness within the same surface structure. The second type maintains a constant wall thickness but introduces a gradient in the distribution density within the same surface structure.

5.3.1 TPMS and lattice homogeneous porous structure design

5.3.1.1 TPMS homogeneous porous structure design

The design of the structure and accompanying mesh is detailed in the steps below and illustrated in Figure 5.2.

1. Preparation of the initial mesh

Firstly, we selected a 3D object to which we wanted to add a TPMS structure. This can be any 3D model in the target application. The cylinder used in this section is 6mm in diameter and 6mm in height. To create TPMS structures, the first step involved preparing a refined initial mesh that could accurately capture the desired surface's shape and details.

2.   Definition of finite element space

In FreeFem++, a finite element space was defined to facilitate subsequent mesh generation and analysis.

3.   Definition of geometric structures

The mathematical expressions defining the TPMS were formulated. These expressions played a crucial role in determining the shape of the generated surfaces. In this process, a set of mathematical expressions representing TPMS was employed, as summarized in Table 5.1.

Function name	Mathematical expression $f(x, y, z)$	Structure unit
Schwarz G (Gyroid)	$\cos(x)\sin(y) + \sin(x)\cos(z) + \cos(y)\sin(z)\cos(x) + \cos(y) + \cos(z)$	
Schwarz D (Diamond)	$\sin(x)\sin(y)\sin(z) + \sin(x)\cos(y)\cos(z) + \cos(x)\sin(y)\cos(z) + \cos(x)\cos(y)\sin(z)$	
Double Diamond	$(\cos(2x)\cos(2y) + \cos(2y)\cos(2z) + \cos(2x)\cos(2z)) + (\sin(2x)\sin(2y)\sin(2z))$	
Schwarz P (Primitive)	$\cos(x) + \cos(y) + \cos(z)$	
F-RD	$4\cos(x)\cos(y)\cos(z) - (\cos(2x)\cos(2y) + \cos(2x)\cos(2z) + \cos(2y)\cos(2z))$	
Fischer-Koch S	$\sin(x)\cos(y)\cos(2z) + \cos(2x)\sin(y)\cos(z) + \cos(x)\cos(2y)\sin(z)$	
I-WP	$2(\cos(x)\cos(y) + \cos(x)\cos(z) + \cos(y)\cos(z)) - (\cos(2x) + \cos(2y) + \cos2(z))$	

Table 5.1: Mathematical equations for designing TPMS structures.

4. Creation and adjustment of distance functions

A distance function was created to extract the desired surfaces from within the cylinder. Additionally, a specific thickness corresponding to the wall thickness of the scaffold structure was assigned to these surfaces. For all the TPMS designs in this section, the wall thickness is 0.2mm (the minimal thickness that can be reliable produced during the additive manufacturing process described in Chapter 3).

5. Saving distance functions

In FreeFem++, the "savesol" function was utilized to store the distance functions as files, ensuring their availability for subsequent processing and visualization.

6. Generation of new mesh

The external tool "mmg3d" was utilized to create the new mesh for TPMS structures. This tool generated the mesh based on the previously defined distance functions.

7. FreeFem++ for Meshed Void Space Extraction

The FreeFem++ software was utilized to extract the meshed void space to be used as the computational domain for this study.

8. Saving the mesh

Finally, the processed mesh portions were saved separately as "scaffold" and "void" to be used for subsequent analysis and simulations. The "scaffold" was saved as a .vtk file for the Paraview visualization. The "void" was saved as a mesh file for the computer simulation.
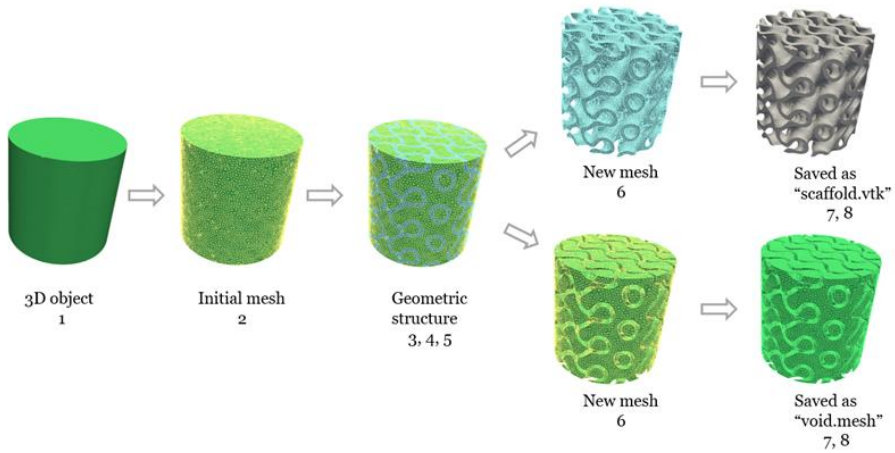
Figure 5.2: Schematic diagram of the generation process of TPMS homogeneous porous structures. The process starts with creating an initial mesh (2) of a 3D object (1) and refining it. In FreeFem++, a finite element space is defined, and mathematical expressions for the TPMS shapes are formulated (3). Distance functions (4) are used to define surface shapes and assign wall thickness, then saved with "savesol" (5). The external tool "mmg3d" generates a new mesh based on these functions (6). FreeFem++ extracts the meshed void space for the computational domain (7), and the processed mesh is saved as "scaffold" and "void" for further use (8).

Table 5.2 contains the overview of all structures generated with the equations in table 5.1 for the larger and smaller pore size. The Figure F.1 in Appendix F describes the 3D pore size measurement for different TPMS geometries.

	Gyroid	Diamond	Double diamond	Fischer-Koch S	F-RD	IWP	Primitive
Pore size: 0.7mm							
Area scaffold (mm²)	562.6	506.1	631.7	574.6	526.1	577.1	573.9
Porosity	66.1%	69.6%	62.3%	65.1%	67.6%	64.7%	64.9%

	Gyroid	Diamond	Double diamond	Fischer-Koch S	F-RD	IWP	Primitive
Pore size: 1mm							
Area scaffold (mm²)	458.0	358.9	519.4	394.0	384.9	452.6	354.7
Porosity	72.9%	79.0%	69.4%	76.9%	77.0%	72.9%	79.2%

Table 5.2: The homogeneous porous structure of TPMS with large pore size (1mm) and small pore size (0.7mm) and the porosity of the geometry. The seven TPMS structures are Gyroid, Diamond, Double Diamond, Fischer-Koch S, F-RD, IWP, and Primitive.

5.3.1.2 Lattice homogeneous porous structure design

1. The Salome platform (https://www.salome-platform.org/) was used to create geometric shapes, which were subsequently saved in .brep format. Following this, meshing was performed using gmsh (http://gmsh.info/), and the resulting mesh was saved in .mesh format.

2. The design dimensions of the lattice structure are 1mm and 0.7mm pore size and 0.2mm wall thickness.
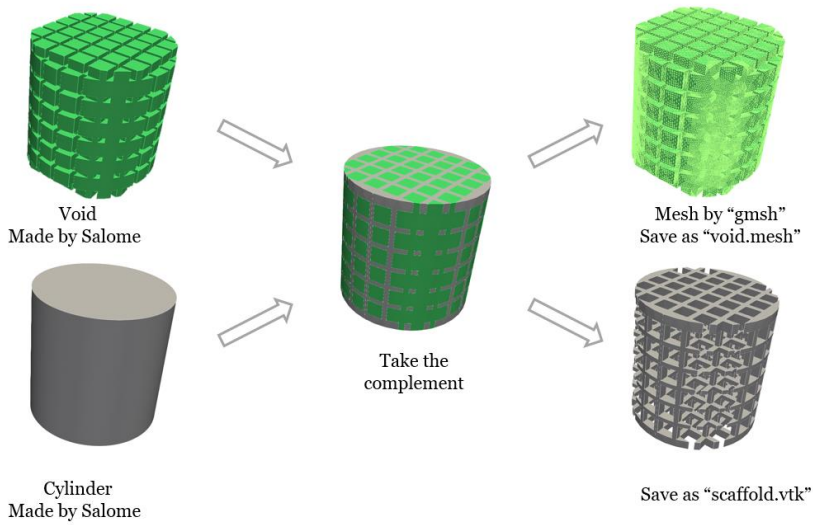
Figure 5.3: Schematic diagram of the generation process of lattice homogeneous porous structures. The geometric shapes are created by Salome. The mesh is created by gmsh. The void space is saved as mesh file for future simulation.
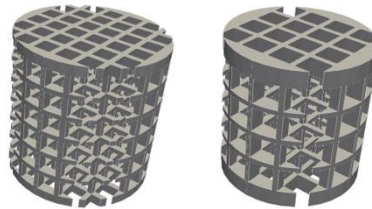
Pore size (mm)	0.7	1
Area scaffold (mm²)	414.4	243.1
Porosity	82.6%	92.5%

Table 5.3: The homogeneous lattice structure with large pore size (1mm) and small pore size (0.7mm) and a quantification of the scaffold area and porosity.

5.3.2 TPMS gradient scaffold design

In order to generate functionally gradient 3D porous structures, the in-house developed tool ASLI (A Simple Lattice Infiller) was employed

(Perez-Boerema et al., 2022). The primary steps for generating TPMS gradient structures are outlined as follows:

1.   Specify the 3D object

In the ASLI environment, specify the 3D object to which a TPMS gradient structures should be added. This can be any 3D model with gradient structures relevant to the target application. In this section, a cylinder with a diameter of 6 millimetres and a height of 6 millimetres was used as the 3D object.

2.   Define local unit cells

In ASLI, choose any TPMS structure as the desired unit cell to fill the cylinder. In this section, Diamond and Gyroid were selected as unit cell structures.

3.   Determine unit cell size

Within the unit cell (1mm x 1mm x 1mm), the pore size is 0.7mm, and the wall thickness is 0.2mm.

4.   Set functional gradients

To generate different types of Diamond and Gyroid TPMS structures, functional gradients need to be set. This means that different local unit cell types and parameters can be defined in different parts of the 3D cylinder. In this chapter, three-dimensional models of two gradient structures are presented. In Gradient Gyroid, Gyroid was used as the unit structure, with a pore size of 0.7mm. The wall thickness in the upper half of the cylinder is 0.17mm, and in the lower half is 0.38mm (Figure 5.4). In Gradient Diamond, Diamond was used as the unit structure, with a wall thickness of 0.2mm. The pore size in the upper half of the cylinder is 0.2mm, and in the lower half, it is 0.54mm.

5.   Design of transition regions

In ASLI, filtering the weights with a Gaussian function constitutes a simple mechanism to create a gradual transition between the different

structures in the gradient and provide direct control over the size of the filtered region.

6.   Exporting the Structure

Finally, ASLI can be used to export an STL file for 3D printing production directly. For computer simulations, a volume mesh of the structure needs to be generated using FreeFem++. For the method of generating the mesh, please refer to the design of the TPMS homogeneous porous structure section.

Gradient Gyroid structure   Gradient Diamond structure
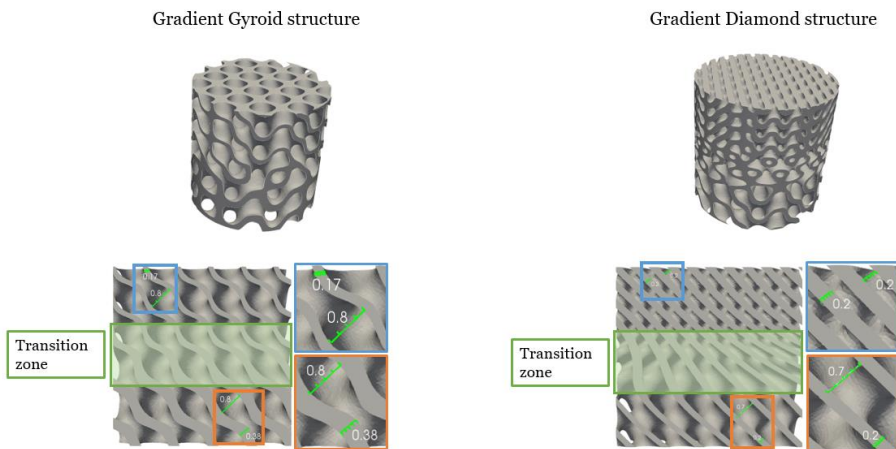
Figure 5.4: The gradient TPMS structures. In the gradient gyroid structure, the pore size remains constant, but the wall thickness becomes wider from top to bottom, showing a gradient distribution. In the gradient diamond structure, the wall thickness remains unchanged, but the pore size increases from top to bottom, showing a gradient distribution. The blue box represents the parameters of the upper part of the geometry, and the orange box represents the parameters of the lower part of the aggregate. The green box represents the transition zone. Dimensions indicated in mm.

5.3.3   Cell seeding density within TPMS scaffold

In this model, the initial thickness of the seeded cells is used as a way to simulate ingrowth of cells into the scaffold in anticipation of future model extensions that will include migration. A first *in silico* experiment investigated the use of sub-physiological initial cell layer thickness The size of hTERT-BMMSCs ranges from 10μm to 30μm. Setting the initial cell seeding thickness to 10μm means that a single layer of cells is evenly distributed on the surface of the scaffold. A smaller value could be used in order to capture a non-confluent cell seeding density. Another way of simulating this early phase could be the use of the standard thickness of the initial cell layer (10μm), combined with a latency period in 3D neotissue growth. This latency period would correspond to the time cells require to reach confluence (hence reach the thickness of 10μm) via 2D substrate-based growth.

In addition, during cell ingrowth into the scaffold, a gradient in cell density will likely be observed. Here, we used a simplified way of representing the emergent cell density gradient observed *in vivo* with lowest thickness representing cells furthest away from the scaffold outer surface. We selected G-7-2, G-9-2, and G-10-2 as the targeting scaffolds and divided the scaffolds into six layers from bottom to top, with the height of each layer being 1mm. The initial thickness of the cells decreases layer by layer from bottom to top, from 0.31mm to 0.3nm. See Figure 5.5 for a diagram of the model setup in G-10-2.

Layers	Seeding cell thickness (mm)
6	3e-7
5	0.01
4	0.03
3	0.07
2	0.13
1	0.3
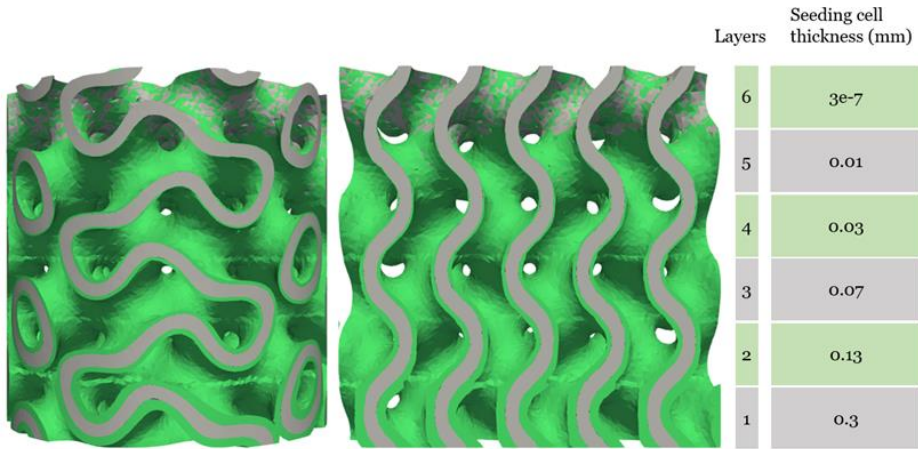
Figure 5.5: An example of the gradient initial cell seeding on a gyroid scaffold with a pore size of 1mm and wall thickness of 0.2mm (G-10-2). The initial cell layer thickness decreases in discrete steps from scaffold bottom to top, from 0.3mm to 0.3nm (lowest value possible still allowing for neotissue growth in that zone).

5.4   Results

5.4.1   Initial cell seeding thickness and growth

In Figure 5.6, the simulation results show that when the initial cell seeding thickness is set to 1e-3mm, the result is the same as obtained with an initial cell thickness value of 10μm plus a latency period of 7 days. The latter was used as the standard condition for simulations shown in this chapter.
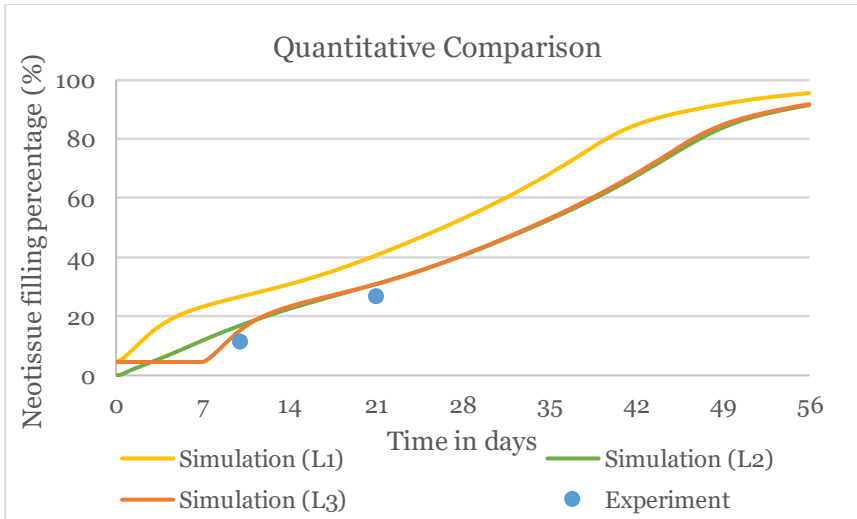
Figure 5.6: Comparison between the different simulation strategies for the initial cell seeding (full line) and the neotissue formation in the experiment (points, for details on the experimental set-up, see chapter 3). L1= Initial thickness of neotissue layer 10μm; L2= Initial thickness of neotissue layer 1e-3mm. L3= Initial thickness of neotissue layer 10μm plus a neotissue growth latency period of 7 days.

5.4.2 Results of homogeneous porous structure

Figure 5.7 shows a comparison of the void filling ratio (new tissue volume (NV)/available volume (AV)) over time for two sizes of the seven tested TPMS shapes for both large (1mm) and small (0.7mm) pore sizes. The total duration of the simulation is 8 weeks. As can be seen from the graph, there is a clear difference in the filling process between structures with large or small pores during the 8 weeks of simulation time. Structures with small pores have a more compact geometry with greater curvature, which promotes growth rates and ultimately results in almost complete filling. On the other hand, it is difficult to achieve a filling rate of 80% for structures with larger pores. It needs to be noted however, that due to differences in scaffold surface area and porosity, the proportion of the initial seeded cell volume to the available volume is different. The porosity of structures with small pores is generally lower than that of structures with large pores, while the surface area of the scaffold with small pores is

larger than that of scaffolds with large pores. Therefore, the proportion of seeded cell volume to the total available volume in scaffolds with small pores is greater than in scaffolds with large pores.
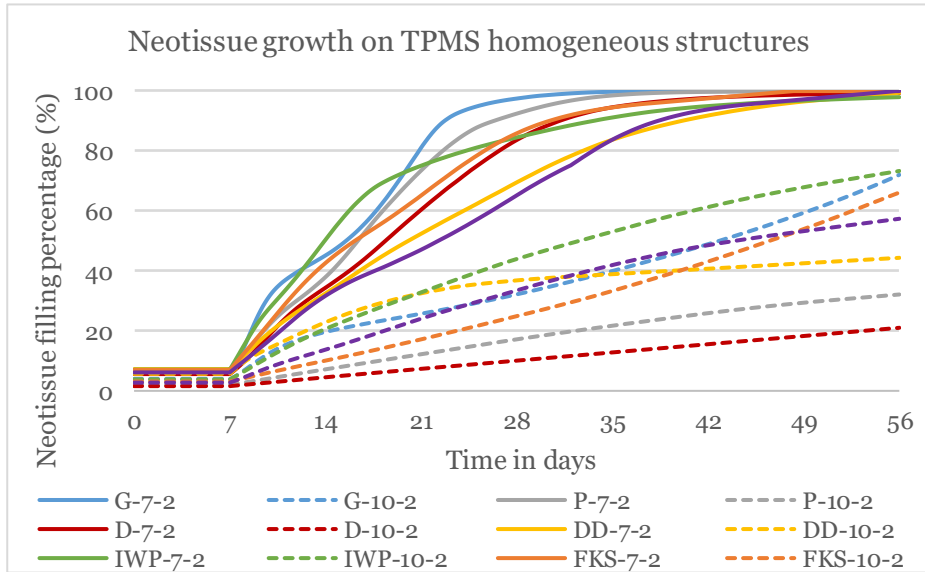
Figure 5.7: The filling process and results of 7 TPMS homogeneous structures over a period of 8 weeks. G: gyroid, P: Schwarz primitive, D: Schwarz diamond, DD: double diamond, IWP: Schoen's I-WP, FKS: Fischer-Koch S, FRD: Schoen's F-RD . The numbers following the letter indicating the structure refer to the pore size (10 = 1mm, 7 = 0.7mm) and wall thickness (2=0.2mm) respectively.

The simulations start with a 7-day latency to capture substrate colonization by the cells. Regardless of the type of TPMS structure, the neotissue growth process will go through a fast filling period (when the filling ratio is less than 80%), followed by a slower filling period (when the filling ratio is greater than 80%). The closer the filling ratio is to 100%, the lower the filling speed. The shape of the filling curve is dependent on the structure, for example, the filling curves of G-7-2, P-7-2, and FKS-7-2 are closer to S-shaped curves, while the filling curves of the remaining structures with small pores are closer to parabolas.

Figure 5.8 shows the change in the simulated scaffold filling rate over time for the lattice structure. Despite differences in porosity and surface area, resulting in varying initial cell volumes, the overall trends remain similar.

This similarity is partially attributed to the necessary adjustment of coefficients in the distance function. The adjustment of coefficients in the distance function is crucial for curvature calculation as it affects the accuracy and stability of curvature. By adjusting the coefficients in the distance function, we can better control the calculation of curvature, ensuring the accuracy and stability of filling rates. Therefore, despite the lower initial cell volume in lattice structures, the adjustment of coefficients in the distance function leads to similar filling trends as TPMS structures.
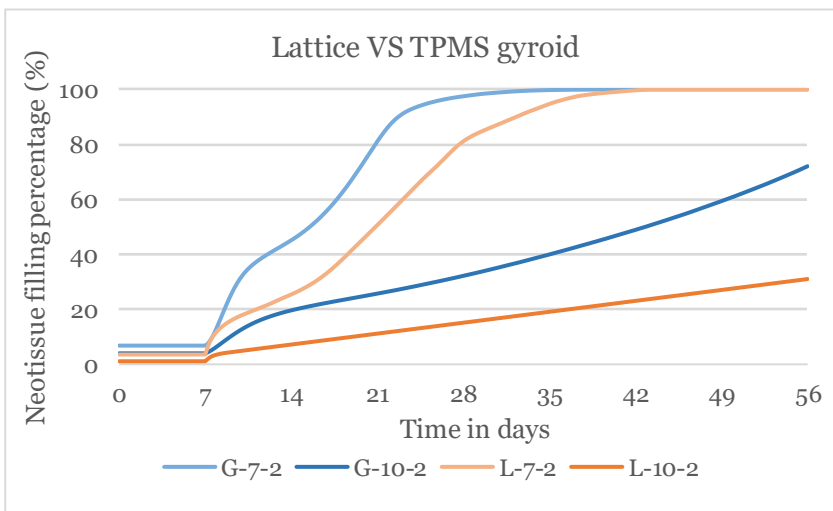
Figure 5.8: The filling results of large and small pore lattice structures over 8 weeks compared to the gyroid results. The filling rate of the lattice structure is slower than that of the gyroid. The lattice structure with a small pore size (0.7mm) reaches a filling percentage of almost 80% within 8 weeks. The lattice structure with a large pore size (1mm) reaches around 30% filling in 8 weeks.

5.4.3 Results for gradient TPMS structure

The results comparing neotissue growth for gradient structures and homogeneous structures are shown in Figure 5.9. Based on the surface area of the scaffold, the TPMS homogeneous structures with similar surface area (similar initial seeded cell volume) were selected as a control for the gradient structures. Compared with homogeneous diamond, the initial filling speed in the gradient diamond structure is higher, which

leads to a larger slope of the filling curve on the gradient structure and a faster increase in filling percentage between days 7 and 14. However, after 14 days, neotissue growth slowed down, dropping below that of the homogeneous diamond. The latter is growing rapidly until the 28th day, when it reaches 80% filling and then enters the slow growth stage. The filling curve of the gradient diamond structure maintains the same slope until 90% filling to then slow down until reaching complete filling. The time taken for both structures to reach complete filling was also similar, with 100% filling completed at approximately week 7. For large-pore gradient gyroid and homogeneous gyroid, the filling curves of the two structures in the first three weeks basically coincide. Afterward, the filling rate of the gradient gyroid is slightly greater than that of the homogeneous gyroid.
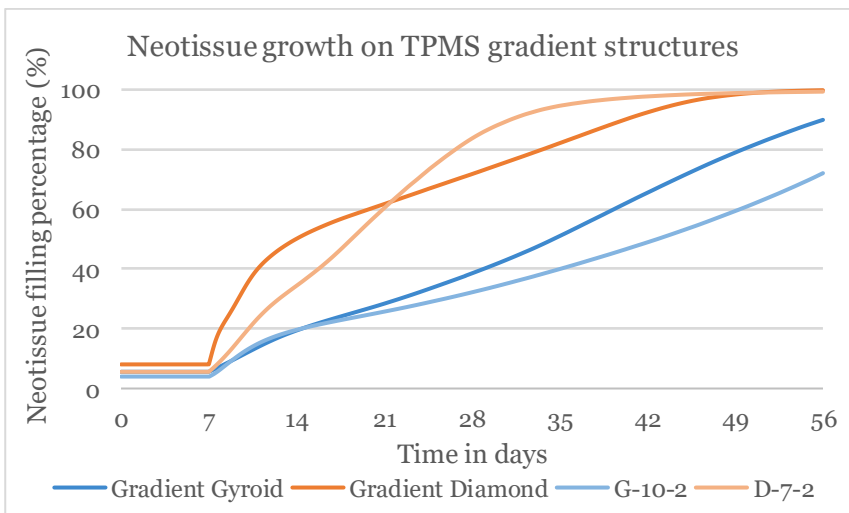
Figure 5.9: The filling results of TPMS gradient structures over 8 weeks. In the gyroid group, the neotissue filling speed in the gradient gyroid structure is slightly faster than that in the homogenous gyroid. In the diamond group, the structures with or without gradient all show a rapid growth period in the first 2 weeks, reaching full filling at almost the same time.

5.4.4 Results of initial seeding gradient cell density in TPMS structure

To understand the potential of the model to capture neotissue ingrowth *in vivo* (rather than just growth), a structure with a gradient in cell seeding density consisting of 6 layers of different initial cell layer thickness was simulated, maintaining a homogeneous latency period of 7 days. From the gyroid filling results of three different pore sizes, we can conclude that scaffolds with a gradient initial cell layer fills faster than those with a uniform initial cell layer. Scaffolds with gradient cell density yield smoother filling curves due to layered seeding, promoting organized spreading and stable growth. This contrasts with uniform density scenarios, avoiding rapid initial growth followed by deceleration. *In vivo*, stratified seeding minimizes cell-cell interactions, while average seeding induces early aggregation and slower growth.
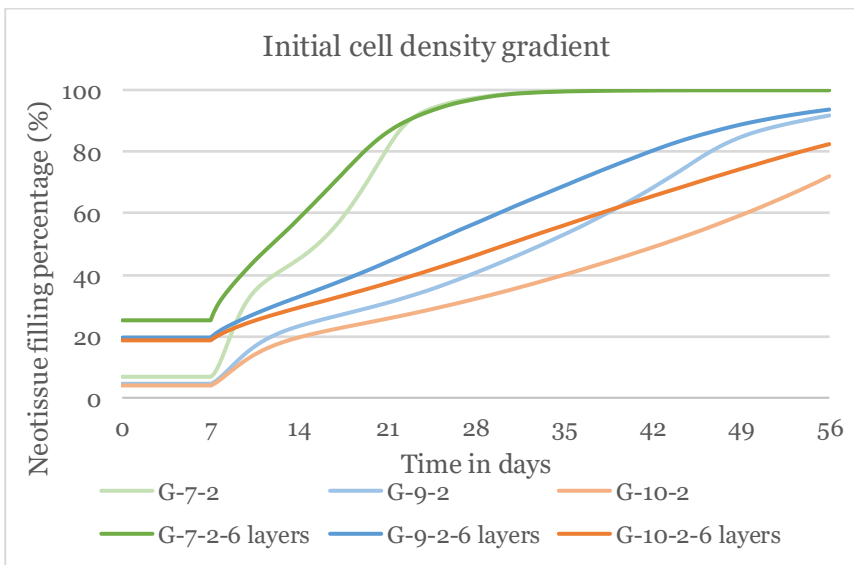
Figure 5.10: The filling demonstration under different initial cell density settings. Among the 3 groups, the structures with gradient initial cell density have a slightly faster filling speed than the structures with average initial cell density. G-7-2 and G-7-2-6 reach full filling in almost the same time, but the filling curve of G-7-2-6 layers is smoother than that of G-7-2.

5.5 Discussion

In summary, the study uncovers diverse growth dynamics within homogeneous TPMS structures, manifested by varied shapes of growth curves reflecting differing topologies, porous distributions, and connectivity. Despite an average curvature of zero, variations in local curvature within TPMS structures influence neotissue growth. Irrespective of structure homogeneity, the filling process follows a similar pattern, transitioning gradually from rapid to slow filling stages. Neotissue growth times in gradient scaffold structures are comparable to non-gradient counterparts, and gradients in initial neotissue layer thickness have negligible effects on growth.

The results of the neotissue growth in homogeneous structures demonstrate different growth dynamics for the different TPMS structures. This is because even though they are all structures with zero average curvature, different TPMS structures have different topologies, porosity distributions, and connectivity. Hence, although the average curvature for the scaffold is zero, the local curvature varies between different TPMS structures. These differences in local curvature lead to differences in neotissue growth curves. Comparing the TPMS and lattice structures, the neotissue growth in the latter is higher than one might expect given that the basic premise of the model is curvature-based growth (which for lattice structures would restrict growth to the strut intersections). In the implementation however, numerical diffusion is added to ensure smoothness of the implementation. This numerical diffusion is responsible for adding neotissue growth that is curvature-independent. Whereas the reason for adding this curvature-independent growth was numerical at the onset, literature does show that although curvature is a strong factor in facilitating neotissue growth, it is not restricted to curved areas. This means that in future work, the curvature-independent neotissue growth should be investigated more carefully in order to include it explicitly in the model.

Whether it is a homogeneous structure or a gradient structure, the filling process will always go through a fast filling stage (preceded by a slow filling stage for S-shaped curves) followed by a slow filling stage, and the closer to 100% filling, the slower the filling speed. This is because, in the initial stages, the geometry provides enough space for the neotissue to expand. As the filling process proceeds, the available space gradually decreases, and factors such as geometry and local curvature limit the filling speed. This simulation result is consistent with the neotissue growth process *in vivo*.

When simulating neotissue growth in gradient scaffold structures, the simulated neotissue growth time to reach complete filling was not much different from the non-gradient cases. This suggests that the reasons to opt for gradient scaffold structures in *in vivo* applications should not be related to the neotissue growth, but more due to the desire to capture physiological gradients in the original tissue structure or capture gradients in the mechanical behaviour. The simulations show that in those cases, neotissue growth will not be heavily impacted by the presence of the gradient.

When simulating gradients in initial neotissue layer thickness as a mimic for the heterogeneity of the initial cell density, no substantial effect on neotissue growth was observed. One limitation of the current implementation is the fact that the latency period was not altered along with the initial thickness, which should probably be the case as the presence of fewer cells on a surface means that the substrate-based growth phase will take longer until confluency has been reached in those areas and 3D growth can start. Regardless, however, the use of gradients in initial layer thickness is a poor representation of the actual process of neotissue ingrowth. If we want a more accurate picture of the process of neotissue ingrowth *in vivo*, we will need to account for the migration of cells into the scaffold. In the current Level-Set implementation it is not possible to capture the migration along the substrate as the model only considers advection of the interface in the direction of the normal to the interface. This means it is not possible to simulate neotissue growth in an

area where there is no initial neotissue layer present. A model extension is required to include also cell migration along the substrate. This cell migration itself is also suggested to be related to curvature (He et al., 2017), along with other factors, such as the formation of blood vessels. This model extension is part of the future work suggested in the final chapter of this thesis.

CHAPTER 6

Conclusions and future perspectives

This chapter includes a summary of the main finding of this PhD research. In Section 6.2, the general discussion of this PhD and its contribution to the field of alveolar bone regeneration is provided. In Section 6.3, some limitations of the current models are pointed out, and possible future research topics are suggested.

6.1 Summary

The first chapter of this thesis introduced the composition, structure, and function of the human skeleton and then described the development, application, and influencing factors of bone formation, bone regeneration, and bone tissue engineering. In addition, it also summarized the experimental and mathematical studies that have been applied in this research field modelling method.

Chapter 2 briefly introduced the two assumptions of this doctoral project. The first objective was to verify the effectiveness of the curvature-driven neotissue growth model on calcium phosphate scaffold materials through *in vitro* experiments, in order to prove the applicability of the model under different conditions. The second objective was to explore how the model could optimize scaffold design for alveolar bone regeneration. This objective aimed to improve the model by adjusting the scaffold's gradient structure and initial cell concentration gradient to better capture the cell growth process inside the scaffold. This optimization process aimed to make the model more realistic for practical application in clinical settings. The chapter ended with a short summary of the different research methodologies used in this PhD project.

Chapter 3 used a combined experimental modelling approach to express a curvature-driven model of regenerative cell growth. The latter was developed to simulate neotissue growth on a three-dimensional scaffolds by calculating curvature changes. Some model parameters were determined based on *in vitro* experiments, some from reference documents, and some through scientific estimation. Bayesian optimization was performed by comparing the experimental results with the model predictions. Limitations of the model and possible suggestions for improvement were also discussed.

In Chapter 4, the model developed in chapter 3 was used to design a 3D scaffold for bone regeneration in a maxillofacial animal model. The design should balance the desire for rapid neotissue growth (captured in the model through the curvature-based growth mechanism) with the desire of

having sufficient living tissue inside the scaffold (to provide a better environment to place a dental implant). In addition, the range of possibilities was restricted by the accuracy and feasibility of the manufacturing process. The chosen design was implanted and the biological results were analysed after 4 and 8 weeks. A comparison with the clinical gold standard and a lattice design showed the superiority of the gyroid design, both in terms of volume of bone formed and penetration depth of that bone inside the scaffold.

In Chapter 5, the curvature-driven cell regeneration simulation model (Chapter 3) was applied to simulate neotissue growth in different TPMS and lattice structures. In addition, different initial cell layer configurations were analysed, in order to understand the capacity of the current model to capture the ingrowth of neotissue observed *in vivo* in situations where scaffolds are implanted without cells seeded onto them. Finally, the influence of gradient structures in the scaffold design on the neotissue growth was investigated, showing that gradient structures had little influence on the neotissue growth rate. These results pointed towards a number of limitation of the current modelling framework when simulating *in vivo* conditions or non-TPMS structures.

6.2   General discussion and contributions

This PhD used *in vivo* and *in vitro* experiments to understand the neotissue growth behaviour on Calcium Phosphate scaffolds and to calibrate an *in silico* model capturing the studied behaviour. This model was then used to design effective scaffold structures, which can be used in the future to optimise personalised scaffold designs in clinics. Chapter 3 confirmed the validity of the curvature-based model to capture neotissue growth in Calcium Phosphate scaffold, through dedicated *in vitro* experiments. The parameter settings of the model were fixed on the cell types and scaffold materials used in this project. Chapter 4 demonstrated through *in vivo* animal experiments that the synthetic additively manufactured Calcium Phosphate-based scaffolds with model-based optimized internal design outperformed the clinical gold standard and the

lattice control. Chapter 5 proposed a broader application of model and studied the capabilities of the model to capture specific elements of *in vivo* tissue formation such as ingrowth and gradient properties. It identified areas for improvement in order for the model to provide a more effective and efficient strategy in the field of alveolar bone regeneration and optimize patients' treatment plans.

PhD questions?
- How to validate and apply curvature-driven neotissue growth model in CaP scaffold?
- How to optimize 3D implant structural design for clinical applications in dental bone regeneration?

Chapter 1   General introduction

Chapter 2   Objectives and methodology

In vitro

Chapter 3

Validation of Level-Set neotissue growth model in calcium-phosphate-based scaffolds

In vivo

Chapter 4

In silico model application to optimize macrostructure enhances bone formation *in vivo*

In silico

Chapter 5

Optimization of 3D scaffold design for better capture of *in vivo* application

Chapter 6   Conclusions and future perspectives
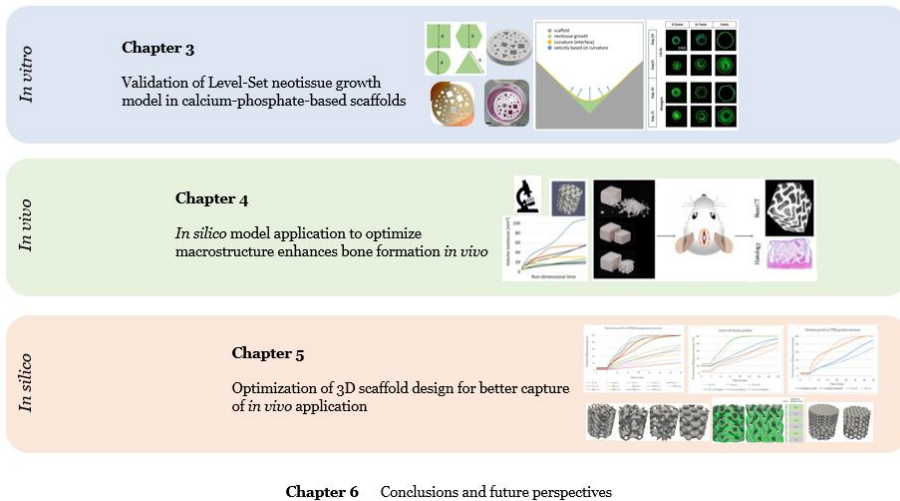
Figure 6.1: Schematic overview of the thesis contributions.

A large number of *in vivo* and *in vitro* studies have shown that there is a relationship between surface shape, and cell growth and cell migration (Alias et al., 2017; Callens et al., 2023; Schamberger et al., 2023; Baptista et al., 2019; Werner et al., 2017). The rate of neotissue growth is curvature-dependent (Nelson et al., 2005; Rumpler et al., 2008; Bidan et al., 2012; Bidan et al., 2013; Jin et al., 2018), with the velocity being proportional to the local curvature (Rumpler et al., 2008; Bidan et al., 2012; Guyot et al., 2014; Sanaei et al., 2019). Some studies explore the use of TPMS

structures for regeneration in greater depth, detailing how this structure is designed and generated (Hsieh et al., 2020; Jones et al., 2021; Feng et al., 2021; AI-Ketan et al., 2020 al., 2021; Blanquer et al., 2017), as well as its advantages in the field of bone regeneration scaffolds (Ambu et al., 2019; Vijayavenkataraman et al., 2018; Lv et al., 2022; Poltue et al., 2021; Pugliese et al., 2023; Han et al., 2018). The experimental results observed in this thesis are consistent with the conclusions of the latter papers. However, none of those studies established numerical simulation models. In addition, some studies on cell growth and migration include numerical simulations (Carlier et al., 2015; Webster et al., 2011; Pivonka et al., 2012; Mustafa et al., 2021; Waters et al., 2021), but these models are not based on calcium phosphate materials. Calcium phosphate scaffolds have been widely used in dental bone tissue regeneration (Alsahafi et al., 2021; Mohd et al., 2022; Hoornaert et al., 2020; Cheah et al., 2021; Alsahafi et al., 2021), and have broad clinical application prospects. However, no to the author's knowledge, there are no studies that follow the integrated *in vitro-in vivo-in silico* approach followed in this thesis to optimize Calcium Phosphate based biomaterials for alveolar bone regeneration.

The integrated approach followed in this thesis allows to deepen our understanding of cell-protein-scaffold interactions, providing a basis for designing more effective scaffolds. In Chapter 3, the level set-based computational framework was shown to be able to predict cell growth on scaffolds in a static environment *in vitro*. In Chapter 4, the model's applicability on 3D scaffolds was corroborated by comparing simulation results with experimental results obtained *in vivo*. Assessing the validity of the curvature-driven neotissue growth model provided across materials and cell sources allows researchers to use this concept when building simulation models that suit their specific applications, including different cell types, scaffold materials and scaffold designs. This *in silico* tool could be used to optimize the design of scaffolds, improve production efficiency, and even introduce innovative biomaterials. The use of models can also reduce the cost and time of experiments. In Chapter 5, the wide application of the model was investigated and suggestions were formulated for further model improvement.

The model validation and application strategies in this PhD involved the interaction of multiple disciplines, such as *in vitro* experiments, *in vivo* animal experiments, new biomaterials, bioprinting technology and bone regeneration scaffold design. This PhD thesis could not have delivered its results without bringing together biology, engineering, and computational science, and apply their tools and concepts on bone regeneration applications. This project is an example of how interdisciplinary research can advance the development of the field.

6.3   Limitations and future perspectives

Figure 6.2 shows the schematic overview of bringing new scaffolds to the patient. This PhD projects focused on the first two steps of this process, involving the initial stages of validating mathematical models to clinical applications. Subsequent steps include clinical validation of the bone formation capacity of the developed scaffolds, followed by regulatory review. During this process, the simulation results can provide digital evidence that is complementary to the *in vitro* and *in vivo* evidence. However, for this digital evidence to be considered by regulatory authorities, a rigorous verification, validation and uncertainty quantification (VVUQ) commensurate with the weight carried by the digital evidence in the overall process (U.S. Food and Drug Administration., 2021). The uncertainty quantification allows to quantify the impact on the simulation outcomes of the assumptions made during the model creation phase as well as the uncertainty on model parameter values. Although the simulation results have been compared to *in vitro* and *in vivo* experimental data, the comparison was mostly qualitative rather than quantitative, Given the current context, though crucial in the early R&D process, the digital evidence is not likely to be included in the dossier. For the additive manufacturing process itself, dedicated standards exist, such as the ASME Y14.46 (American Society of Mechanical Engineers., 2022). Cerhum, one of the research partners in this project, has received approval in Europe for its 3D-printed bone to treat patients with severe facial deformities. The process is the first

commercially available 3D printed bone graft authorized under the Medical Device Regulation 2017/745 (MDR), registered with the Belgium Competent Authority (FAMHP, registration number BE/CA01/1-72228) and ISO 13485 certified.
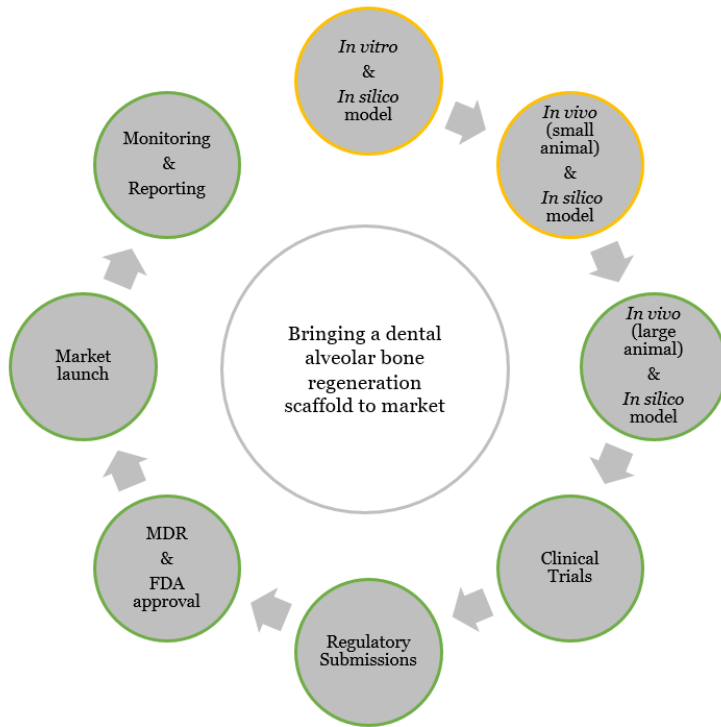
Figure 6.2: Schematic overview of bringing new scaffolds to the patient. The yellow border indicates the phases of research addressed in this PhD. The green border indicates the ongoing and next phases of the wider research project.

For the future development of the model, we can start by incorporating more detailed biological factors and, through further research on the biological mechanism of bone regeneration, consider more biological factors that will affect the growth of new tissue and integrate these mechanisms into computer models. Future developments in modelling could include several detailed aspects such as using piecewise linear functions to describe the impact of shear stress on cell growth, and employing the Michaelis-Menten equation to represent how oxygen and

glucose concentrations affect growth velocity. The effect of pH on cell growth could also be modelled using a piecewise linear function, addressing how acidic environments influence cellular activity (Guyot et al., 2016). Additionally, a comprehensive model predicting calcium ion release from calcium phosphate (CaP) scaffolds could account for dissolution, diffusion, and scaffold characteristics. Both ectopic and orthotopic bone formation models could explore the effects of BMP-2 delivery systems and various CaP-BMP-cell combinations, validated against experimental data (Varun et al., 2017). Multiscale modelling captures interactions between cellular, molecular, and tissue-level processes. This will help improve the accuracy of the predictive model. In the future, computer models will be more integrated with biology, medicine, engineering, and other disciplines and use the advantages of each discipline to build more comprehensive and accurate models. For example, experts in biology and medicine can provide computer models with more detailed physiological data. In the future, computer models may also be integrated with patient-specific data to develop personalized bone regeneration growth models that can be used to guide clinical decision-making. In addition to being used for neotissue prediction, this model will be more widely used in various fields of bone tissue regeneration, such as fracture healing, bone defect repair, and implant development.

6.3.1 *In silico* modelling perspectives

Bone formation is a complex multiscale process involving multiple cell types, molecular signals, and extracellular matrix types playing out over multiple time and length scales. The computational model developed in this PhD does not capture these complex interactions. For example, growth factors, cytokines, and other signalling factors affecting neotissue growth are not present in the current version of the *in silico* model. In addition, the model is not able simulate the process of tissue ingrowth not a porous structure and requires an initial cell layer to be present throughout the structure. Capturing ingrowth requires the addition of cell

migration along the structure's surface, which is dependent on cellular and biomaterial properties, as well as local curvature. Increasing model complexity will also increase the computational cost. FreeFem++ has several options for parallelisation, as described in Chapter 3, which helps to alleviate concerns related to computational cost. Finally, when moving towards personalised implants, biological and anatomical differences among individuals will need to be accounted for in order for the model to predict changes in bone tissue growth accurately.

For the future development of the model, we can start by incorporating more detailed descriptions of the biological mechanisms involved in bone regeneration, and including additional variables related to those mechanisms. Multiscale models allow to actions of, and interactions between, molecular, cellular, and tissue-level processes. In addition to being used for neotissue predictions, such extended model could be used more widely in various fields of bone tissue regeneration, such as fracture healing, bone defect repair, and implant development. In addition to being a multiscale process, tissue growth is also a multi-physics and multi-factorial process, including mechanical, chemical, and biological aspects. To improve existing models, one could consider aspects such as physical aspects of mechanical loading (Guyot et al., 2016), the influence of growth factors such as BMP-2 (Ribeiro et al., 2015), the use of specific biomaterials (Perier-Metz et al., 2022), the effect of surface roughness (Dalby et al., 2004; Biggs et al., 2009; Ponsonnet et al., 2002;), diffusion of calcium ions and phosphorus ions (Manhas et al., 2017), precipitation and dissolution (Ostapienko et al., 2019;), angiogenesis (Sun et al., 2013;), oxygen release (Zhang et al., 2016;), pH and temperature (Barrere et al., 2006;) etc.

6.3.2 *In vitro* and *in vivo* experimental perspectives

Many countries have formulated strict laws and regulations for developing, testing and marketing *medicinal product*s, including regulatory standards for animal experiments and clinical trials. These regulations are designed to ensure the safety and effectiveness of marketed products to protect the

rights and interests of patients. In this context, animal experiments and clinical trials remain indispensable, as they assess the performance and effectiveness of products in situations that are closer to real human situations. Many research groups work on finding alternatives to animal testing through the combination of computer models and *in vitro* experiments. Though advances are made and many regulatory dossiers include digital evidence, they still cannot completely replace *in vivo* animal experiments and clinical trials in most cases. This fact arises from multiple reasons that involve not only scientific and technical limitations but also regulatory and ethical considerations. Although *in vitro* experiments have the advantage of being controlled and quantitative, they still suffer from a significant limitation: their inability to fully simulate the complex multicellular systems in the human body. Within the human body, complex interactions and signalling pathways exist between cells and tissues, which are critical for tissue regeneration and the performance of medicinal products.

In animal experiments, researchers can better observe and evaluate the scaffold's behaviour upon implantation. This includes the material's degradation process, biocompatibility, metabolic and immunological response, as well as possible side effects. This systemic information is critical for formulating safe medicinal products and computer models and *in vitro* experiments typically do not provide this information. In addition, there are differences among human individuals, due to elements such as genetics, lifestyle, and disease history. Animal experiments and clinical trials allow studies to be conducted in diverse populations and set-ups, to better to understand the impact of population variability and diversity on treatment outcomes. This is crucial for developing a more precise treatment plan.

Bone regeneration and tissue engineering treatments usually require consideration of long-term effects, such as many years or even the lifetime. Animal experiments and clinical trials can track and evaluate these long-term effects, including scaffold durability, biocompatibility, and patient quality of life. Computer models and *in vitro* experiments cannot provide

this kind of long-term observation. However, depending on the application, in silico models can be used to augment the *in vivo* data by providing an additional long-term time point beyond the duration of the experiments after using the *in vivo* data for model calibration.

In summary, although computer models and *in vitro* experiments play an essential role in bone tissue engineering, they are complementary to *in vivo* animal experiments and clinical trials. Only through the combined application of these three approaches (*in vitro, in vivo, in silico*) can we more comprehensively understand and evaluate new medicinal products and treatments to ensure their safety and effectiveness in clinical practice. This comprehensive approach will advance the field of bone regeneration, allowing patients to receive better treatment and care.

Future research directions will include delving into personalized medical solutions and using 3D structural data to formulate highly personalized oral bone tissue engineering scaffolds to maximize treatment outcomes (Figure 6.3). The partners in the project that this PhD research is part of, are expanding the scope of the (large) animal experiments to more comprehensively evaluate the feasibility and safety of personalised treatment options. In addition, they will focus on long-term tracking of treatment effects and understand the long-term biocompatibility of the scaffold and the patient's quality of life after implantation. These data will then also be used to further optimise the computational model in a new model development iteration.
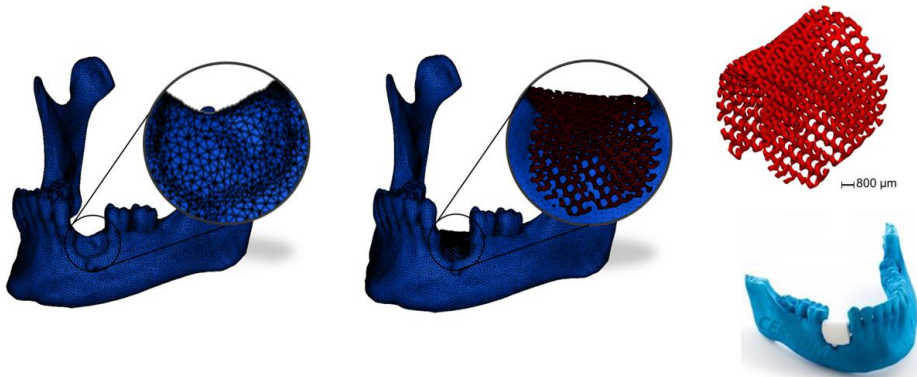
Figure 6.3: The concept of a personalized TPMS scaffolds for alveolar bone regeneration. Image courtesy of Fernando Perez-Boerema.

Finally, the long-term goal of the research performed in this PhD is to translate the findings on optimal scaffold design to human patients in the field of oral medicine. We will continue to promote interdisciplinary cooperation across multiple fields such as biology, engineering, clinical medicine, and materials science, promote the exchange of knowledge and technology, and provide a broader perspective for the further development of the bone tissue engineering field.

References

Abbasi, N., Hamlet, S., Love, R. M., & Nguyen, N. T. (2020). Porous scaffolds for bone regeneration. *Journal of science: advanced materials and devices*, *5*(1), 1-9.

Adachi, T., Osako, Y., Tanaka, M., Hojo, M., & Hollister, S. J. (2006). Framework for optimal design of porous scaffold microstructure by computational simulation of bone regeneration. *Biomaterials, 27*(21), 3964-3972.

Aerssens, J., Boonen, S., Lowet, G., & Dequeker, J. (1998). Interspecies differences in bone composition, density, and quality: potential implications for *in vivo* bone research. *Endocrinology, 139*(2), 663-670.

Afshar, M., Anaraki, A. P., Montazerian, H., & Kadkhodapour, J. (2016). Additive manufacturing and mechanical characterization of graded porosity scaffolds designed based on triply periodic minimal surface architectures. *Journal of the mechanical behaviour of biomedical materials*, *62*, 481-494.

Ahrens, J., Geveci, B., Law, C., Hansen, C., & Johnson, C. (2005). 36-paraview: An end-user tool for large-data visualization. *The visualization handbook*, *717*, 50038-1.

Akter, F. and Ibanez, J., 2016. Bone and cartilage tissue engineering. *In Tissue Engineering Made Easy* (77-97). Academic Press.

Alaribe, F. N., Manoto, S. L., & Motaung, S. C. (2016). Scaffolds from biomaterials: advantages and limitations in bone and tissue engineering. *Biologia, 71*(4), 353-366.

Albrektsson, T., & Wennerberg, A. (2004). Oral implant surfaces: Part 1--review focusing on topographic and chemical properties of different surfaces and *in vivo* responses to them. *International Journal of Prosthodontics*, *17*(5).

Alias, M. A., & Buenzli, P. R. (2017). Modelling the effect of curvature on the collective behaviour of cells growing new tissue. *Biophysical Journal*, *112*(1), 193-204.

Al-Ketan, O., & Abu Al-Rub, R. K. (2021). MSLattice: A free software for generating uniform and graded lattices based on triply periodic minimal surfaces. *Material Design & Processing Communications, 3*(6), e205.

Alsahafi, R. A., Mitwalli, H. A., Balhaddad, A. A., Weir, M. D., Xu, H. H., & Melo, M. A. S. (2021). Regenerating craniofacial dental defects with calcium phosphate cement scaffolds: Current status and innovative scope review. *Frontiers in Dental Medicine, 2*, 743065.

Alsahafi, R. A., Mitwalli, H. A., Balhaddad, A. A., Weir, M. D., Xu, H. H., & Melo, M. A. S. (2021). Regenerating craniofacial dental defects with calcium phosphate cement scaffolds: Current status and innovative scope review. *Frontiers in Dental Medicine, 2*, 743065.

Alt, V., Nawab, A., & Seligson, D. (1999). Bone grafting from the proximal tibia. *Journal of Trauma and Acute Care Surgery*, *47*(3), 555-557.

Ambu, R., & Morabito, A. E. (2019). Modelling, assessment, and design of porous cells based on schwartz primitive surface for bone scaffolds. *The Scientific World Journal,* 2019.

American Society of Mechanical Engineers, *Product Definition for Additive Manufacturing*, Standard Y14.46-2022, 2022. [Online]. Available: https://www.asme.org/codes-standards/find-codes-standards/y14-46-product-definition-additive-manufacturing-(1)/2022/pdf

Amestoy, P. R., Duff, I. S., L'Excellent, J. Y., & Koster, J. (2000, June). MUMPS: a general purpose distributed memory sparse solver. In *International Workshop on Applied Parallel Computing* (121-130). Berlin, Heidelberg: Springer Berlin Heidelberg.

An, S. Y., Lee, Y. J., Neupane, S., Jun, J. H., Kim, J. Y., Lee, Y., ... & Kim, J. Y. (2017). Effects of vascular formation during alveolar bone process morphogenesis in mice. *Histochemistry and Cell Biology*, *148*, 435-443.

Andrukhov, O., Huber, R., Shi, B., Berner, S., Rausch-Fan, X., Moritz, A., ... & Schedle, A. (2016). Proliferation, behaviour , and differentiation of osteoblasts on surfaces of different microroughness. *Dental materials*, *32*(11), 1374-1384.

Ansari, M., 2019. Bone tissue regeneration: biology, strategies and interface studies. *Progress in biomaterials, 8*(4), 223-237.

Antoni, D., Burckel, H., Josset, E., & Noel, G. (2015). Three-dimensional cell culture: a breakthrough *in vivo*. *International journal of molecular sciences*, *16*(3), 5517-5527.

Artzi, Z., Nemcovsky, C. E., & Dayan, D. (2002). Bovine-HA spongiosa blocks and immediate implant placement in sinus augmentation procedures: Histopathological and histomorphometric observations on different histological stainings in 10 consecutive patients. *Clinical Oral Implants Research*, *13*(4), 420-427.

Babensee, J.E., McIntire, L.V. and Mikos, A.G., 2000. Growth factor delivery for tissue engineering. *Pharmaceutical research, 17*(5), 497-504.

Bailon-Plaza, A., & Van Der Meulen, M. C. (2001). A mathematical framework to study the effects of growth factor influences on fracture healing. *Journal of Theoretical Biology, 212*(2), 191-209.

Bal, Z., Kaito, T., Korkusuz, F., & Yoshikawa, H. (2020). Bone regeneration with hydroxyapatite-based biomaterials. *Emergent Materials*, *3*, 521-544.

Baldwin, P., Li, D. J., Auston, D. A., Mir, H. S., Yoon, R. S., & Koval, K. J. (2019). Autograft, allograft, and bone graft substitutes: clinical evidence and indications for use in the setting of orthopaedic trauma surgery. *Journal of orthopaedic trauma*, *33*(4), 203-213.

Baptista, D., Teixeira, L., van Blitterswijk, C., Giselbrecht, S., & Truckenmüller, R. (2019). Overlooked? Underestimated? Effects of substrate curvature on cell behaviour . *Trends in biotechnology, 37*(8), 838-854.

Barrère, F., van Blitterswijk, C. A., & de Groot, K. (2006). Bone regeneration: molecular and cellular interactions with calcium phosphate ceramics. *International journal of nanomedicine, 1*(3), 317.

Barzegari, M., & Geris, L. (2021). An open source crash course on parameter estimation of computational models using a Bayesian optimization approach. *Journal of Open Source Education*, *4*(40).

Bath-Balogh, M., & Fehrenbach, M. J. (2014). *Illustrated Dental Embryology, Histology, and Anatomy-E-Book*. Elsevier Health Sciences.

Bedada, F.B., Günther, S., Kubin, T. and Braun, T., 2006. Differentiation versus plasticity: fixing the fate of undetermined adult stem cells. *Cell Cycle, 5*(3), 223-226.

Betz, R. R. (2002). Limitations of autograft and allograft: new synthetic solutions. *Orthopedics*, *25*(5), S561-S570.

Bidan, C. M., Kommareddy, K. P., Rumpler, M., Kollmannsberger, P., Fratzl, P., & Dunlop, J. W. (2013). Geometry as a factor for tissue growth: towards shape optimization of tissue engineering scaffolds. *Advanced healthcare materials*, *2*(1), 186-194.

Bidan, C. M., Kommareddy, K. P., Rumpler, M., Kollmannsberger, P., Bréchet, Y. J., Fratzl, P., & Dunlop, J. W. (2012). How linear tension converts to curvature: geometric control of bone tissue growth. *PloS one*, *7*(5), e36336.

Bielby, R., Jones, E. and McGonagle, D., 2007. The role of mesenchymal stem cells in maintenance and repair of bone. *Injury, 38*(1), S26-S32.

Biggs, M. J., Richards, R. G., Gadegaard, N., McMurray, R. J., Affrossman, S., Wilkinson, C. D., ... & Dalby, M. J. (2009). Interactions with nanoscale topography: adhesion quantification and signal transduction in cells of osteogenic and multipotent lineage. *Journal of Biomedical Materials Research Part A: An Official Journal of The Society for Biomaterials, The Japanese Society for Biomaterials, and The Australian Society for Biomaterials and the Korean Society for Biomaterials, 91*(1), 195-208.

Bilezikian, J.P., Raisz, L.G. and Martin, T.J. eds., 2008. *Principles of bone biology*. Academic press.

Blanquer, S. B., Werner, M., Hannula, M., Sharifi, S., Lajoinie, G. P., Eglin, D., ... & Grijpma, D. W. (2017). Surface curvature in triply-periodic minimal surface architectures as a distinct design parameter in preparing advanced tissue engineering scaffolds. *Biofabrication*, *9*(2), 025001.

Boccaccio, A., Uva, A. E., Fiorentino, M., Mori, G., & Monno, G. (2016). Geometry design optimization of functionally graded scaffolds for bone tissue engineering: A mechanobiological approach. *PloS one*, *11*(1), e0146935.

Bone|Definition, Anatomy, & Composition|Britannica. Available online: https://www.britannica.com/science/bone-anatomy

Bosch, P., Musgrave, D.S., Lee, J.Y., Cummins, J., Shuler, F., Ghivizzani, S.C., Evans, C., Robbins, P.D. and Huard, J., 2000. *Osteoprogenitor cells within skeletal muscle. Journal of Orthopaedic Research, 18*(6), 933-944.

Bottaro, D. P., LIEBMANN-VINSON, A. N. D. R. E. A., & Heidaran, M. A. (2002). Molecular signalling in bioengineered tissue microenvironments. *Annals of the New York Academy of Sciences*, *961*(1), 143-153.

Bouakaz, I., Dehkord, E. S., Meille, S., Schrijnemakers, A., Boschini, F., Preux, N., ... & Dupret-Bories, A. (2024). 3D printed triply periodic minimal surfaces calcium phosphate bone substitute: The effect of porosity design on mechanical properties. *Ceramics International*, *50*(2), 2623-2636.

Buenzli, P. R., Lanaro, M., Wong, C. S., McLaughlin, M. P., Allenby, M. C., Woodruff, M. A., & Simpson, M. J. (2020). Cell proliferation and migration explain pore bridging dynamics in 3D printed scaffolds of different pore size. *Acta Biomaterialia*, *114*, 285-295.

Byrne, D. P., Lacroix, D., Planell, J. A., Kelly, D. J., & Prendergast, P. J. (2007). Simulation of tissue differentiation in a scaffold as a function of porosity, Young's modulus and dissolution rate: application of mechanobiological models in tissue engineering. *Biomaterials, 28*(36), 5544-5554.

Callens, S. J., Fan, D., van Hengel, I. A., Minneboo, M., Díaz-Payno, P. J., Stevens, M. M., ... & Zadpoor, A. A. (2023). Emergent collective organization of bone cells in complex curvature fields. *Nature Communications*, *14*(1), 855.

Callens, S. J., Fan, D., van Hengel, I. A., Minneboo, M., Díaz-Payno, P. J., Stevens, M. M., ... & Zadpoor, A. A. (2023). Emergent collective organization of bone cells in complex curvature fields. *Nature Communications, 14*(1), 855.

Callens, S. J., Uyttendaele, R. J., Fratila-Apachitei, L. E., & Zadpoor, A. A. (2020). Substrate curvature as a cue to guide spatiotemporal cell and tissue organization. *Biomaterials*, *232*, 119739.

Carlier, A., Chai, Y. C., Moesen, M., Theys, T., Schrooten, J., Van Oosterwyck, H., & Geris, L. (2011). Designing optimal calcium phosphate scaffold–cell combinations using an integrative model-based approach. *Acta Biomaterialia, 7*(10), 3573-3585.

Carlier, A., Geris, L., Bentley, K., Carmeliet, G., Carmeliet, P., & Van Oosterwyck, H. (2012). MOSAIC: a multiscale model of osteogenesis and sprouting angiogenesis with lateral inhibition of endothelial cells.

Carlier, A., Geris, L., Lammens, J., & Van Oosterwyck, H. (2015). Bringing computational models of bone regeneration to the clinic. *Wiley Interdisciplinary Reviews: Systems Biology and Medicine, 7*(4), 183-194.

Carlier, A., Lammens, J., Van Oosterwyck, H., & Geris, L. (2015). Computational modelling of bone fracture non-unions: four clinically relevant case studies. *In silico Cell and Tissue Science*, *2*, 1-12.

Carrel, J. P., Wiskott, A., Scherrer, S., & Durual, S. (2016). Large bone vertical augmentation using a three-dimensional printed TCP/HA bone graft: A pilot study in dog mandible. *Clinical implant dentistry and related research*, *18*(6), 1183-1192.

Carter, D. R., Beaupré, G. S., Giori, N. J., & Helms, J. A. (1998). Mechanobiology of skeletal regeneration. *Clinical Orthopaedics and Related Research (1976-2007), 355*, S41-S55.

Chakka, J.L., Acri, T., Laird, N.Z., Zhong, L., Shin, K., Elangovan, S. and Salem, A.K., 2021. Polydopamine functionalized VEGF gene-activated 3D printed scaffolds for bone regeneration. *RSC Advances, 11*(22), 13282-13291.

Champion, E. (2013). Sintering of calcium phosphate bioceramics. *Acta biomaterialia*, *9*(4), 5855-5875.

Charles-Harris, M., del Valle, S., Hentges, E., Bleuet, P., Lacroix, D., & Planell, J. A. (2007). Mechanical and structural characterisation of completely degradable polylactic acid/calcium phosphate glass scaffolds. *Biomaterials, 28*(30), 4429-4438.

Cheah, C. W., Al-Namnam, N. M., Lau, M. N., Lim, G. S., Raman, R., Fairbairn, P., & Ngeow, W. C. (2021). Synthetic material for bone, periodontal, and dental tissue regeneration: Where are we now, and where are we heading next?. *Materials, 14*(20), 6123.

Chen, Y., Wu, X., Li, J., Jiang, Y., Xu, K., & Su, J. (2022). Bone-targeted nanoparticle drug delivery system: an emerging strategy for bone-related disease. *Frontiers in pharmacology, 13*, 909408.

Cheng, M. Q., Wahafu, T., Jiang, G. F., Liu, W., Qiao, Y. Q., Peng, X. C., ... & Liu, X. Y. (2016). A novel open-porous magnesium scaffold with controllable microstructures and properties for bone regeneration. Sci Rep 6: 24134.

Cho, M. I., & Garant, P. R. (2000). Development and general structure of the periodontium. *Periodontology 2000*, *24*(1).

Claes, L. E., & Heigele, C. A. (1999). Magnitudes of local stress and strain along bony surfaces predict the course and type of fracture healing. *Journal of biomechanics, 32*(3), 255-266.

Coelho, P. G., Hollister, S. J., Flanagan, C. L., & Fernandes, P. R. (2015). Bioresorbable scaffolds for bone tissue engineering: optimal design, fabrication, mechanical testing and scale-size effects analysis. *Medical engineering & physics*, *37*(3), 287-296.

Collins, C., & Nelson, W. J. (2015). Running with neighbors: coordinating cell migration and cell–cell adhesion. *Current opinion in cell biology*, *36*, 62-70.

Collins, M. N., Ren, G., Young, K., Pina, S., Reis, R. L., & Oliveira, J. M. (2021). Scaffold fabrication technologies and structure/function properties in bone tissue engineering. *Advanced functional materials*, *31*(21), 2010609.

Cun, X., & Hosta-Rigau, L. (2020). Topography: a biophysical approach to direct the fate of mesenchymal stem cells in tissue engineering applications. *Nanomaterials*, *10*(10), 2070.

Dalby, M. J., Riehle, M. O., Johnstone, H., Affrossman, S., & Curtis, A. S. G. (2004). Investigating the limits of filopodial sensing: a brief report using SEM to image the interaction between 10 nm high nano-topography and fibroblast filopodia. *Cell biology international, 28*(3), 229-236.

Dapogny, C., & Frey, P. (2012). Computation of the signed distance function to a discrete contour on adapted triangulation. *Calcolo*, *49*, 193-219.

De Carvalho, B., Rompen, E., Lecloux, G., Schupbach, P., Dory, E., Art, J. F., & Lambert, F. (2019). Effect of sintering on *in vivo* biological performance of chemically deproteinized bovine hydroxyapatite. *Materials*, *12*(23), 3946.

De Wild, M., Ghayor, C., Zimmermann, S., Rüegg, J., Nicholls, F., Schuler, F., ... & Weber, F. E. (2019). Osteoconductive lattice microarchitecture for optimized bone regeneration. *3D Printing and Additive Manufacturing*, *6*(1), 40-49.

Dehkord, E. S., De Carvalho, B., Ernst, M., Albert, A., Lambert, F., & Geris, L. (2024). Influence of physicochemical characteristics of calcium phosphate-based biomaterials in cranio-maxillofacial bone regeneration. A systematic literature review and meta-analysis of preclinical models. *Materials Today Bio*, 101100.

Dennis, S.C., Berkland, C.J., Bonewald, L.F. and Detamore, M.S., 2015. Endochondral ossification for enhancing bone regeneration: converging native extracellular matrix biomaterials and developmental engineering *in vivo*. *Tissue Engineering Part B: Reviews, 21*(3), 247-266.

Denry, I., & Kuhn, L. T. (2016). Design and characterization of calcium phosphate ceramic scaffolds for bone tissue engineering. *Dental Materials*, *32*(1), 43-53.

Dias, M. R., Guedes, J. M., Flanagan, C. L., Hollister, S. J., & Fernandes, P. R. (2014). Optimization of scaffold design for bone tissue engineering: A

computational and experimental study. *Medical engineering & physics*, *36*(4), 448-457.

Dimitriou, R., Jones, E., McGonagle, D., & Giannoudis, P. V. (2011). Bone regeneration: current concepts and future directions. *BMC medicine*, *9*, 1-10.

Djomehri, S. I., Candell, S., Case, T., Browning, A., Marshall, G. W., Yun, W., ... & Ho, S. P. (2015). Mineral density volume gradients in normal and diseased human tissues. *PloS one*, *10*(4), e0121611.

Dong, Z., & Zhao, X. (2021). Application of TPMS structure in bone regeneration. *Engineered Regeneration*, *2*, 154-162.

Dorozhkin, S. V., & Epple, M. (2002). Biological and medical significance of calcium phosphates. *Angewandte Chemie International Edition*, *41*(17), 3130-3146.

Egan, P. F. (2019). Integrated design approaches for 3D printed tissue scaffolds: Review and outlook. *Materials*, *12*(15), 2355.

El-Rashidy, A. A., Roether, J. A., Harhaus, L., Kneser, U., & Boccaccini, A. R. (2017). Regenerating bone with bioactive glass scaffolds: A review of *in vivo* studies in bone defect models. *Acta biomaterialia*, *62*, 1-28.

Erdemir, A., Mulugeta, L., Ku, J. P., Drach, A., Horner, M., Morrison, T. M., ... & Myers Jr, J. G. (2020). Credible practice of modelling and simulation in healthcare: ten rules from a multidisciplinary perspective. *Journal of translational medicine*, *18*(1), 369.

Erices, A., Conget, P. and Minguell, J.J., 2000. Mesenchymal progenitor cells in human umbilical cord blood. *British journal of haematology, 109*(1), 235-242.

Faul, F., Erdfelder, E., Lang, A. G., & Buchner, A. (2007). G* Power 3: A flexible statistical power analysis program for the social, behaviour al, and biomedical sciences. *Behaviour research methods*, *39*(2), 175-191.

Fellah, B. H., Gauthier, O., Weiss, P., Chappard, D., & Layrolle, P. (2008). Osteogenicity of biphasic calcium phosphate ceramics and bone autograft in a goat model. *Biomaterials*, *29*(9), 1177-1188.

Feng, J., Liu, B., Lin, Z., & Fu, J. (2021). Isotropic porous structure design methods based on triply periodic minimal surfaces. *Materials & Design*, *210*, 110050.

Feng, P., Zhao, R., Tang, W., Yang, F., Tian, H., Peng, S., ... & Shuai, C. (2023). Structural and functional adaptive artificial bone: materials, fabrications, and properties. *Advanced Functional Materials*, *33*(23), 2214726.

Fernandes, H. R., Gaddam, A., Rebelo, A., Brazete, D., Stan, G. E., & Ferreira, J. M. (2018). Bioactive glasses and glass-ceramics for healthcare applications in bone regeneration and tissue engineering. *Materials, 11*(12), 2530.

Figliuzzi, M., Mangano, F. G., Fortunato, L., De Fazio, R., Macchi, A., Iezzi, G., ... & Mangano, C. (2013). Vertical ridge augmentation of the atrophic posterior mandible with custom-made, computer-aided design/computer-aided manufacturing porous hydroxyapatite scaffolds. *Journal of Craniofacial Surgery*, *24*(3), 856-859.

Foreman, M. A., Gu, Y., Howl, J. D., Jones, S., & Publicover, S. J. (2005). Group III metabotropic glutamate receptor activation inhibits Ca2+ influx and nitric oxide synthase activity in bone marrow stromal cells. *Journal of cellular physiology*, *204*(2), 704-713.

Gamsjäger, E., Bidan, C. M., Fischer, F. D., Fratzl, P., & Dunlop, J. W. C. (2013). Modelling the role of surface stress on the kinetics of tissue growth in confined geometries. *Acta biomaterialia*, *9*(3), 5531-5543.

García-Aznar, J. M., Nasello, G., Hervas-Raluy, S., Pérez, M. Á., & Gómez-Benito, M. J. (2021). Multiscale modelling of bone tissue mechanobiology. *Bone*, *151*, 116032.

Gariboldi, M. I., & Best, S. M. (2015). Effect of ceramic scaffold architectural parameters on biological response. *Frontiers in bioengineering and biotechnology*, *3*, 151.

Garot, C., Bettega, G., & Picart, C. (2021). Additive manufacturing of material scaffolds for bone regeneration: toward application in the clinics. *Advanced functional materials*, *31*(5), 2006967.

Garot, C., Bettega, G., & Picart, C. (2021). Additive manufacturing of material scaffolds for bone regeneration: toward application in the clinics. *Advanced functional materials*, *31*(5), 2006967.

Gennarelli, T.A. and Thibault, L.E., 1982. Biomechanics of acute subdural hematoma. *The Journal of trauma, 22*(8), 680-686.

Geris, L., Gerisch, A., Vander Sloten, J., Weiner, R., & Van Oosterwyck, H. (2008). Angiogenesis in bone fracture healing: a bioregulatory model. *Journal of theoretical biology, 251*(1), 137-158.

Geris, L., Vandamme, K., Naert, I., Vander Sloten, J., Duyck, J., & Van Oosterwyck, H. (2008). Application of mechanoregulatory models to simulate peri-implant tissue formation in an *in vivo* bone chamber. *Journal of biomechanics,* 41(1), 145-154.

Giuliani, A., Manescu, A., Mohammadi, S., Mazzoni, S., Piattelli, A., Mangano, F., ... & Mangano, C. (2016). Quantitative kinetics evaluation of blocks versus granules of biphasic calcium phosphate scaffolds (HA/β-TCP 30/70) by synchrotron radiation x-ray microtomography: a human study. *Implant Dentistry*, *25*(1), 6-15.

Goffard, R., Sforza, T., Clarinval, A., Dormal, T., Boilet, L., Hocquet, S., & Cambier, F. (2013). Additive manufacturing of biocompatible ceramics. *Adv. Prod. Eng. Manag*, *8*, 96-106.

Goffard, R., Sforza, T., Clarinval, A., Dormal, T., Boilet, L., Hocquet, S., & Cambier, F. (2013). Additive manufacturing of biocompatible ceramics. *Adv. Prod. Eng. Manag*, *8*, 96-106.

Goldberg, M. (2022). The Alveolar Bone Provides Support to Teeth and Other Functions: A Review. *Med. Sci. Monit*, *3*, 1-17.

Gómez-Benito, M. J., García-Aznar, J. M., Kuiper, J. H., & Doblaré, M. (2005). Influence of fracture gap size on the pattern of long bone healing: a computational study. *Journal of theoretical biology, 235*(1), 105-119.

Greco, R. S., Prinz, F. B., & Smith, R. L. (Eds.). (2004). *Nanoscale technology in biological systems*. CRC press.

Griffith, L. G., & Swartz, M. A. (2006). Capturing complex 3D tissue physiology *in vitro*. *Nature reviews Molecular cell biology*, *7*(3), 211-224.

Griffith, L.G., 2002. Emerging design principles in biomaterials and scaffolds for tissue engineering. *Annals of the New York Academy of Sciences, 961*(1), 83-95.

Groeneveldt, L. C., Knuth, C., Witte-Bouma, J., O'Brien, F. J., Wolvius, E. B., & Farrell, E. (2014). Enamel matrix derivative has no effect on the chondrogenic differentiation of mesenchymal stem cells. *Frontiers in Bioengineering and Biotechnology*, *2*, 29.

Guyot, Y., Papantoniou, I., Chai, Y. C., Van Bael, S., Schrooten, J., & Geris, L. (2014). A computational model for cell/ECM growth on 3D surfaces using the

level set method: a bone tissue engineering case study. *Biomechanics and modelling in mechanobiology*, *13*, 1361-1371.

Guyot, Y., Papantoniou, I., Luyten, F. P., & Geris, L. (2016). Coupling curvature-dependent and shear stress-stimulated neotissue growth in dynamic bioreactor cultures: a 3D computational model of a complete scaffold. *Biomechanics and modelling in mechanobiology*, *15*, 169-180.

Guyot, Y., Papantoniou, I., Luyten, F.P. and Geris, L., (2016). Coupling curvature-dependent and shear stress-stimulated neotissue growth in dynamic bioreactor cultures: a 3D computational model of a complete scaffold. *Biomechanics and modelling in mechanobiology, 15*(1), pp.169-180.

Habibovic, P., Sees, T. M., van den Doel, M. A., van Blitterswijk, C. A., & de Groot, K. (2006). Osteoinduction by biomaterials—physicochemical and structural influences. *Journal of Biomedical Materials Research Part A: An Official Journal of The Society for Biomaterials, The Japanese Society for Biomaterials, and The Australian Society for Biomaterials and the Korean Society for Biomaterials*, *77*(4), 747-762.

Habibovic, P., Yuan, H., Van Der Valk, C. M., Meijer, G., van Blitterswijk, C. A., & De Groot, K. (2005). 3D microenvironment as essential element for osteoinduction by biomaterials. *Biomaterials*, *26*(17), 3565-3575.

Han, L., & Che, S. (2018). An overview of materials with triply periodic minimal surfaces and related geometry: from biological structures to self-assembled systems. *Advanced Materials, 30*(17), 1705708.

Han, Y., Wei, Q., Chang, P., Hu, K., Okoro, O. V., Shavandi, A., & Nie, L. (2021). Three-dimensional printing of hydroxyapatite composites for biomedical application. *Crystals*, *11*(4), 353.

Harding, I. S., Rashid, N., & Hing, K. A. (2005). Surface charge and the effect of excess calcium ions on the hydroxyapatite surface. *Biomaterials*, *26*(34), 6818-6826.

Hayashi, K., Kishida, R., Tsuchiya, A., & Ishikawa, K. (2023). Superiority of triply periodic minimal surface gyroid structure to strut-based grid structure in both strength and bone regeneration. *ACS Applied Materials & Interfaces*, *15*(29), 34570-34577.

He, X., & Jiang, Y. (2017). Substrate curvature regulates cell migration. *Physical biology, 14*(3), 035006.

Hecht, F. (2012). New development in FreeFem++. *Journal of numerical mathematics*, *20*(3-4), 251-266.

Helal, M. H., Hendawy, H. D., Gaber, R. A., Helal, N. R., & Aboushelib, M. N. (2019). Osteogenesis ability of CAD-CAM biodegradable polylactic acid scaffolds for reconstruction of jaw defects. *The Journal of Prosthetic Dentistry*, *121*(1), 118-123.

Herzog, E.L., Chai, L. and Krause, D.S., 2003. Plasticity of marrow-derived stem cells. *Blood, 102*(10), 3483-3493.

Hoornaert, A., & Layrolle, P. (2020). Bone regenerative issues related to bone grafting biomaterials. *Dental Implants and Bone Grafts*, 207-215.

Hou, X., Zhang, L., Zhou, Z., Luo, X., Wang, T., Zhao, X., ... & Zheng, L. (2022). Calcium phosphate-based biomaterials for bone repair. *Journal of functional biomaterials*, *13*(4), 187.

Hsieh, M. T., & Valdevit, L. (2020). Minisurf–A minimal surface generator for finite element modelling and additive manufacturing. *Software Impacts, 6*, 100026.

Huang, Y. C., Kaigler, D., Rice, K. G., Krebsbach, P. H., & Mooney, D. J. (2005). Combined angiogenic and osteogenic factor delivery enhances bone marrow stromal cell-driven bone regeneration. *Journal of bone and mineral research*, *20*(5), 848-857.

Hulbert, S., Young, F. A., Mathews, R. S., Klawitter, J. J., Talbert, C. D., & Stelling, F. H. (1970). Potential of ceramic materials as permanently implantable skeletal prostheses. *Journal of biomedical materials research*, *4*(3), 433-456.

Hutmacher, D.W., 2001. Scaffold design and fabrication technologies for engineering tissues—state of the art and future perspectives. *Journal of Biomaterials Science, Polymer Edition, 12*(1), 107-124.

Inzana, J. A., Olvera, D., Fuller, S. M., Kelly, J. P., Graeve, O. A., Schwarz, E. M., ... & Awad, H. A. (2014). 3D printing of composite calcium phosphate and collagen scaffolds for bone regeneration. *Biomaterials*, *35*(13), 4026-4034.

Isaksson, H., 2012. Recent advances in mechanobiological modelling of bone regeneration. *Mechanics Research Communications, 42*, 22-31.

Jacotti, M., Barausse, C., & Felice, P. (2014). Posterior atrophic mandible rehabilitation with onlay allograft created with CAD-CAM procedure: a case report. *Implant dentistry*, *23*(1), 22-28.

Jensen, C., & Teng, Y. (2020). Is it time to start transitioning from 2D to 3D cell culture?. *Frontiers in molecular biosciences*, *7*, 33.

Jeong, J., Kim, J. H., Shim, J. H., Hwang, N. S., & Heo, C. Y. (2019). Bioactive calcium phosphate materials and applications in bone regeneration. *Biomaterials research, 23*(1), 1-11.

Jeong, J., Kim, J. H., Shim, J. H., Hwang, N. S., & Heo, C. Y. (2019). Bioactive calcium phosphate materials and applications in bone regeneration. *Biomaterials research*, *23*(1), 4.

Jiang, Y., Jahagirdar, B.N., Reinhardt, R.L., Schwartz, R.E., Keene, C.D., Ortiz-Gonzalez, X.R., Reyes, M., Lenvik, T., Lund, T., Blackstad, M. and Du, J., 2002. Pluripotency of mesenchymal stem cells derived from adult marrow. *Nature, 418*(6893), 41-49.

Jin, W., Lo, K. Y., Chou, S. E., McCue, S. W., & Simpson, M. J. (2018). The role of initial geometry in experimental models of wound closing. *Chemical Engineering Science, 179*, 221-226.

Jones, A. C., Arns, C. H., Hutmacher, D. W., Milthorpe, B. K., Sheppard, A. P., & Knackstedt, M. A. (2009). The correlation of pore morphology, interconnectivity and physical properties of 3D ceramic scaffolds with bone ingrowth. *Biomaterials*, *30*(7), 1440-1451.

Jones, A., Leary, M., Bateman, S., & Easton, M. (2021). TPMS Designer: A tool for generating and analyzing triply periodic minimal surfaces. *Software Impacts, 10*, 100167.

Jones, J.R. and Hench, L.L., 2003. Regeneration of trabecular bone using porous ceramics. *Current Opinion in Solid State and Materials Science, 7*(4-5), 301-307.

Kaigler, D., Cirelli, J.A. and Giannobile, W.V., 2006. Growth factor delivery for oral and periodontal tissue engineering. *Expert opinion on drug delivery, 3*(5), 647-662.

Kanwar, S., & Vijayavenkataraman, S. (2022). 3D printable bone-mimicking functionally gradient stochastic scaffolds for tissue engineering and bone implant applications. *Materials & Design*, *223*, 111199.

Kapfer, S. C., Hyde, S. T., Mecke, K., Arns, C. H., & Schröder-Turk, G. E. (2011). Minimal surface scaffold designs for tissue engineering. *Biomaterials*, *32*(29), 6875-6882.

Kashikar-Zuck, S., Goldschneider, K.R., Powers, S.W., Vaught, M.H. and Hershey, A.D., 2001. Depression and functional disability in chronic pediatric pain. *The Clinical journal of pain, 17*(4), 341-349.

Kerckhofs, G., Chai, Y. C., Luyten, F. P., & Geris, L. (2016). Combining microCT-based characterization with empirical modelling as a robust screening approach for the design of optimized CaP-containing scaffolds for progenitor cell-mediated bone formation. *Acta biomaterialia*, *35*, 330-340.

Kern, S., Eichler, H., Stoeve, J., Klüter, H. and Bieback, K., 2006. Comparative analysis of mesenchymal stem cells from bone marrow, umbilical cord blood, or adipose tissue. *Stem cells, 24*(5), 1294-1301.

Kilkenny, C., Browne, W. J., Cuthill, I. C., Emerson, M., & Altman, D. G. (2012). Improving bioscience research reporting: the ARRIVE guidelines for reporting animal research. *Osteoarthritis and cartilage*, *20*(4), 256-260.

Kim, Y. J., & Henkin, J. (2015). Micro-computed tomography assessment of human alveolar bone: bone density and three-dimensional micro-architecture. *Clinical implant dentistry and related research*, *17*(2), 307-313.

Klenke, F. M., Liu, Y., Yuan, H., Hunziker, E. B., Siebenrock, K. A., & Hofstetter, W. (2008). Impact of pore size on the vascularization and osseointegration of ceramic bone substitutes *in vivo*. *Journal of Biomedical Materials Research Part A: An Official Journal of The Society for Biomaterials, The Japanese Society for Biomaterials, and The Australian Society for Biomaterials and the Korean Society for Biomaterials*, *85*(3), 777-786.

Kommareddy, K. P., Lange, C., Rumpler, M., Dunlop, J. W., Manjubala, I., Cui, J., ... & Fratzl, P. (2010). Two stages in three-dimensional *in vitro* growth of tissue generated by osteoblastlike cells. *Biointerphases*, *5*(2), 45-52.

Kumar, A., & Han, S. S. (2021). Enhanced mechanical, biomineralization, and cellular response of nanocomposite hydrogels by bioactive glass and halloysite nanotubes for bone tissue regeneration. *Materials Science and Engineering: C, 128*, 112236.

Lacroix, D. A., & Prendergast, P. J. (2002). A mechano-regulation model for tissue differentiation during fracture healing: analysis of gap size and loading. *Journal of biomechanics*, *35*(9), 1163-1171.

Lacroix, D., Planell, J. A., & Prendergast, P. J. (2009). Computer-aided design and finite-element modelling of biomaterial scaffolds for bone tissue

engineering. *Philosophical Transactions of the Royal Society A: Mathematical, Physical and Engineering Sciences, 367*(1895), 1993-2009.

Lamalice, L., Le Boeuf, F., & Huot, J. (2007). Endothelial cell migration during angiogenesis. *Circulation research, 100*(6), 782-794.

Lambert, F., Bacevic, M., Layrolle, P., Schüpbach, P., Drion, P., & Rompen, E. (2017). Impact of biomaterial microtopography on bone regeneration: comparison of three hydroxyapatites. *Clinical oral implants research*, *28*(10), e201-e207.

Lanza, R., Langer, R., Vacanti, J.P. and Atala, A. eds., 2020. *Principles of tissue engineering*. Academic press.

Lasanianos, N. G., Kanakaris, N. K., & Giannoudis, P. V. (2010). Current management of long bone large segmental defects. *Orthopaedics and Trauma*, *24*(2), 149-163.

Le Guéhennec, L., Van Hede, D., Plougonven, E., Nolens, G., Verlée, B., De Pauw, M. C., & Lambert, F. (2020). *In vitro* and *in vivo* biocompatibility of calcium-phosphate scaffolds three-dimensional printed by stereolithography for bone regeneration. *Journal of Biomedical Materials Research Part A*, *108*(3), 412-425.

Leong, K. F., Chua, S. C., Sudarmadji, N., & Yeong, W. Y. (2008). Engineering functionally graded tissue engineering scaffolds. *Journal of the mechanical behavior of biomedical materials*, *1*(2), 140-152.

Li, J., Wu, C., Chu, P. K., & Gelinsky, M. (2020). 3D printing of hydrogels: Rational design strategies and emerging biomedical applications. *Materials Science and Engineering: R: Reports*, *140*, 100543.

Li, Y., Li, J., Jiang, S., Zhong, C., Zhao, C., Jiao, Y., ... & Shen, M. (2023). The design of strut/TPMS-based pore geometries in bioceramic scaffolds guiding osteogenesis and angiogenesis in bone regeneration. *Materials Today Bio*, *20*, 100667.

Li, Z., Chen, Z., Chen, X., & Zhao, R. (2022). Effect of surface curvature on the mechanical and mass-transport properties of additively manufactured tissue scaffolds with minimal surfaces. *ACS Biomaterials Science & Engineering*, *8*(4), 1623-1643.

Liao, S. S., Cui, F. Z., Zhang, W., & Feng, Q. L. (2004). Hierarchically biomimetic bone scaffold materials: nano-HA/collagen/PLA composite. *Journal of Biomedical Materials Research Part B: Applied Biomaterials: An Official*

Journal of The Society for Biomaterials, The Japanese Society for Biomaterials, and The Australian Society for Biomaterials and the Korean Society for Biomaterials, *69*(2), 158-165.

Lin, K., Sheikh, R., Romanazzo, S., & Roohani, I. (2019). 3D printing of bioceramic scaffolds—barriers to the clinical translation: from promise to reality, and future perspectives. *Materials*, *12*(17), 2660.

Liu, L., Shi, Q., Chen, Q., & Li, Z. (2019). Mathematical modelling of bone in-growth into undegradable porous periodic scaffolds under mechanical stimulus. *Journal of Tissue Engineering, 10*, 2041731419827167.

Liu, X. and Ma, P.X., 2004. Polymeric scaffolds for bone tissue engineering. *Annals of biomedical engineering, 32*(3), 477-486.

Liu, X., Rahaman, M. N., & Fu, Q. (2013). Bone regeneration in strong porous bioactive glass (13-93) scaffolds with an oriented microstructure implanted in rat calvarial defects. *Acta biomaterialia*, *9*(1), 4889-4898.

Loeffler, M. and Roeder, I., 2002. Tissue stem cells: definition, plasticity, heterogeneity, self-organization and models—a conceptual approach. *Cells Tissues Organs, 171*(1), 8-26.Miwa, H., Hashimoto, Y.

Loh, Q. L., & Choong, C. (2013). Three-dimensional scaffolds for tissue engineering applications: role of porosity and pore size.

Long, J. P., Hollister, S. J., & Goldstein, S. A. (2012). A paradigm for the development and evaluation of novel implant topologies for bone fixation: *in vivo* evaluation. *Journal of biomechanics*, *45*(15), 2651-2657.

Luo, D., Rong, Q., & Chen, Q. (2017). Finite-element design and optimization of a three-dimensional tetrahedral porous titanium scaffold for the reconstruction of mandibular defects. *Medical Engineering & Physics*, *47*, 176-183.

Luo, X., Yang, B., Sheng, L., Chen, J., Li, H., Xie, L., ... & Tian, W. (2015). CAD based design sensitivity analysis and shape optimization of scaffolds for bio-root regeneration in swine. *Biomaterials*, *57*, 59-72.

Lv, Y., Wang, B., Liu, G., Tang, Y., Liu, J., Wei, G., & Wang, L. (2022). Design of bone-like continuous gradient porous scaffold based on triply periodic minimal surfaces. *Journal of Materials Research and Technology, 21,* 3650-3665.

Malik, N., & Jaypee Brothers (Jaypeedigital). (2016). *Textbook of oral and maxillofacial surgery* (4/e).

Mangano, F., Macchi, A., Shibli, J. A., Luongo, G., Iezzi, G., Piattelli, A., ... & Mangano, C. (2014). Maxillary ridge augmentation with custom-made CAD/CAM scaffolds. A 1-year prospective study on 10 patients. *Journal of Oral Implantology*, *40*(5), 561-569.

Manhas, V., 2017. *In silico* modelling of bone formation under the influence of calcium phosphate-based biomaterials and osteochondrogenic growth factors (Doctoral dissertation, Université de Liège, Liège, Belgique).

Manhas, V., Guyot, Y., Kerckhofs, G., Chai, Y. C., & Geris, L. (2017). Computational modelling of local calcium ions release from calcium phosphate-based scaffolds. *Biomechanics and modelling in mechanobiology, 16*(2), 425-438.

Mason, C. and Dunnill, P., 2008. A brief definition of regenerative medicine.

Mason, D., 1998. A very high level of crossreactivity is an essential feature of the T-cell receptor. Immunology today, 19(9), 395-404.

Mauney, J.R., Volloch, V. and Kaplan, D.L., 2005. Role of adult mesenchymal stem cells in bone tissue engineering applications: current status and future prospects. *Tissue engineering, 11*(5-6), 787-802.

Mealy, J., & O'Kelly, K. (2015). Cell response to hydroxyapatite surface topography modulated by sintering temperature. *Journal of Biomedical Materials Research Part A*, *103*(11), 3533-3538.

Mehdizadeh, M., & Yang, J. (2013). Design strategies and applications of tissue bioadhesives. *Macromolecular bioscience, 13*(3), 271-288.

Mehrian, M., Guyot, Y., Papantoniou, I., Olofsson, S., Sonnaert, M., Misener, R., & Geris, L. (2018). Maximizing neotissue growth kinetics in a perfusion bioreactor: an *in silico* strategy using model reduction and Bayesian optimization. *Biotechnology and bioengineering*, *115*(3), 617-629.

Meijer, G.J., de Bruijn, J.D., Koole, R. and van Blitterswijk, C.A., 2007. Cell-based bone tissue engineering. *PLoS Med, 4*(2), p.e9.

Melchels, F. P., Barradas, A. M., Van Blitterswijk, C. A., De Boer, J., Feijen, J., & Grijpma, D. W. (2010). Effects of the architecture of tissue engineering scaffolds on cell seeding and culturing. *Acta biomaterialia*, *6*(11), 4208-4217.

Melchels, F. P., Tonnarelli, B., Olivares, A. L., Martin, I., Lacroix, D., Feijen, J., ... & Grijpma, D. W. (2011). The influence of the scaffold design on the distribution of adhering cells after perfusion cell seeding. *Biomaterials, 32*(11), 2878-2884.

Melsen, B., 1999. Biological reaction of alveolar bone to orthodontic tooth movement. *The Angle Orthodontist, 69*(2), 151-158.

Metallo, C. M., Mohr, J. C., Detzel, C. J., de Pablo, J. J., Van Wie, B. J., & Palecek, S. P. (2007). Engineering the stem cell microenvironment. *Biotechnology progress*, *23*(1), 18-23.

Milazzo, M., Contessi Negrini, N., Scialla, S., Marelli, B., Farè, S., Danti, S., & Buehler, M. J. (2019). Additive manufacturing approaches for hydroxyapatite-reinforced composites. *Advanced Functional Materials*, *29*(35), 1903055.

Misch, C. M. (1999). Use of a surgical template for autologous bone grafting of alveolar defects. *Journal of Prosthodontics*, *8*(1), 47-52.

Mockus, J. (2012). *Bayesian Approach to Global Optimization: Theory and Applications* (Vol. 37). Springer Science & Business Media.

Mohammadi, H., Sepantafar, M., Muhamad, N., & Bakar Sulong, A. (2021). How does scaffold porosity conduct bone tissue regeneration?. *Advanced Engineering Materials*, *23*(10), 2100463.

Mohd, N., Razali, M., Ghazali, M. J., & Abu Kasim, N. H. (2022). 3D-printed hydroxyapatite and tricalcium phosphates-based scaffolds for alveolar bone regeneration in animal models: A scoping review. *Materials, 15*(7), 2621.

Mustafa, N. S., Akhmal, N. H., Izman, S., Ab Talib, M. H., Shaiful, A. I. M., Omar, M. N. B., ... & Illias, S. (2021). Application of computational method in designing a unit cell of bone tissue engineering scaffold: a review. *Polymers, 13*(10), 1584.

Nakahara, H., Dennis, J.E., Bruder, S.P., Haynesworth, S.E., Lennon, D.P. and Caplan, A.I., 1991. *In vitro* differentiation of bone and hypertrophic cartilage from periosteal-derived cells. *Experimental cell research, 195*(2), 492-503.

Nelson, C. M., Jean, R. P., Tan, J. L., Liu, W. F., Sniadecki, N. J., Spector, A. A., & Chen, C. S. (2005). Emergent patterns of growth controlled by multicellular form and mechanics. *Proceedings of the National Academy of Sciences, 102*(33), 11594-11599.

Nicholas, J.G., Watkins, L.E. and Voytik-Harbin, S.L., 2016. Bone tissue engineering: scalability and optimization of densified collagen-fibril bone graft substitute materials.

Noordin, N. N. F. N. M., Ahmad, N., Jaafar, M., Yahaya, B. H., Sulaiman, A. R., & Hamid, Z. A. A. (2022). A review of bioceramics scaffolds for bone defects in different types of animal models: HA and β-TCP. *Biomedical Physics & Engineering Express*, *8*(5), 052002.

Nöth, U., Osyczka, A. M., Tuli, R., Hickok, N. J., Danielson, K. G., & Tuan, R. S. (2002). Multilineage mesenchymal differentiation potential of human trabecular bone- derived cells. *Journal of Orthopaedic Research, 20*(5), 1060-1069.

Osher, S., & Sethian, J. A. (1988). Fronts propagating with curvature-dependent speed: Algorithms based on Hamilton-Jacobi formulations. *Journal of computational physics*, *79*(1), 12-49.

Ostapienko, B. I., Lopez, D., & Komarova, S. V. (2019). Mathematical modelling of calcium phosphate precipitation in biologically relevant systems: scoping review. *Biomechanics and modelling in mechanobiology, 18*, 277-289.

Ostrowska, B., Di Luca, A., Moroni, L. and Swieszkowski, W., 2016. Influence of internal pore architecture on biological and mechanical properties of three-dimensional fiber deposited scaffolds for bone regeneration. *Journal of biomedical materials research Part A, 104*(4), 991-1001.

Osyczka, A., Nagashima, K.V., Sogabe, S., Miki, K., Shimada, K. and Matsuura, K., 2001. Different Mechanisms of the Binding of Soluble Electron Donors to the Photosynthetic Reaction Center ofRubrivivax gelatinosus and Blastochloris viridis. *Journal of Biological Chemistry, 276*(26), 24108-24112.

Ozasa, R., Matsugaki, A., Isobe, Y., Saku, T., Yun, H.S. and Nakano, T., 2018. Construction of human induced pluripotent stem cell- derived oriented bone matrix microstructure by using *in vitro* engineered anisotropic culture model. *Journal of Biomedical Materials Research Part A, 106*(2), 360-369.

Pampaloni, F., Reynaud, E. G., & Stelzer, E. H. (2007). The third dimension bridges the gap between cell culture and live tissue. *Nature reviews Molecular cell biology*, *8*(10), 839-845.

Papantoniou, I., Hall, G. N., Loverdou, N., Lesage, R., Herpelinck, T., Mendes, L., & Geris, L. (2021). Turning Nature's own processes into design strategies for living bone implant biomanufacturing: a decade of Developmental Engineering. *Advanced Drug Delivery Reviews*, *169*, 22-39.

Park, S.Y., Ki, C.S., Park, Y.H., Jung, H.M., Woo, K.M. and Kim, H.J., 2010. Electrospun silk fibroin scaffolds with macropores for bone regeneration: an *in vitro* and *in vivo* study. *Tissue Engineering Part A, 16*(4), 1271-1279.

Pathmanathan, P., Cordeiro, J. M., & Gray, R. A. (2019). Comprehensive uncertainty quantification and sensitivity analysis for cardiac action potential models. *Frontiers in physiology*, *10*, 721.

Patterson, E. A., & Whelan, M. P. (2017). A framework to establish credibility of computational models in biology. *Progress in biophysics and molecular biology*, *129*, 13-19.

Patterson, J., Siew, R., Herring, S. W., Lin, A. S., Guldberg, R., & Stayton, P. S. (2010). Hyaluronic acid hydrogels with controlled degradation properties for oriented bone regeneration. *Biomaterials*, *31*(26), 6772-6781.

Peacock, M. (2010). Calcium metabolism in health and disease. *Clinical Journal of the American society of nephrology*, *5*(Supplement_1), S23-S30.

Peate, I. (2018). Anatomy and physiology, 5. The musculoskeletal system. British Journal of Healthcare Assistants, 12(1), 6-9.

Perez, R. A., & Mestres, G. (2016). Role of pore size and morphology in musculo-skeletal tissue regeneration. *Materials Science and Engineering: C*, *61*, 922-939.

Perez-Boerema, F., Barzegari, M., & Geris, L. (2022). A flexible and easy-to-use open-source tool for designing functionally graded 3D porous structures. *Virtual and Physical Prototyping*, *17*(3), 682-699.

Perier-Metz, C., Duda, G. N., & Checa, S. (2020). Mechano-biological computer model of scaffold-supported bone regeneration: effect of bone graft and scaffold structure on large bone defect tissue patterning. *Frontiers in bioengineering and biotechnology*, *8*, 585799.

Perier-Metz, C., Duda, G. N., & Checa, S. (2020). Mechano-biological computer model of scaffold-supported bone regeneration: effect of bone graft and scaffold structure on large bone defect tissue patterning. *Frontiers in bioengineering and biotechnology*, *8*, 585799.

Pieuchot, L., Marteau, J., Guignandon, A., Dos Santos, T., Brigaud, I., Chauvy, P. F., ... & Anselme, K. (2018). Curvotaxis directs cell migration through cell-scale curvature landscapes. *Nature communications*, *9*(1), 3995.

Pilipchuk, S.P., Plonka, A.B., Monje, A., Taut, A.D., Lanis, A., Kang, B. and Giannobile, W.V., 2015. Tissue engineering for bone regeneration and osseointegration in the oral cavity. *Dental Materials, 31*(4), 317-338.

Pires, T. H., Dunlop, J. W., Castro, A. P., & Fernandes, P. R. (2022). Wall shear stress analysis and optimization in tissue engineering TPMS scaffolds. *Materials*, *15*(20), 7375.

Pivonka P, Dunstan CR. Role of mathematical modelling in bone fracture healing. *BoneKEy reports*. 2012;1.

Poltue, T., Karuna, C., Khrueaduangkham, S., Seehanam, S., & Promoppatum, P. (2021). Design exploration of 3D-printed triply periodic minimal surface scaffolds for bone implants. *International Journal of Mechanical Sciences, 211,* 106762.

Polyanin, A. D., Zaitsev, V. F., & Moussiaux, A. (2001). *Handbook of first-order partial differential equations*. CRC Press.

Ponsonnet, L., Comte, V., Othmane, A., Lagneau, C., Charbonnier, M., Lissac, M., & Jaffrezic, N. (2002). Effect of surface topography and chemistry on adhesion, orientation and growth of fibroblasts on nickel–titanium substrates. *Materials Science and Engineering: C, 21*(1-2), 157-165.

Prasadh, S., Ratheesh, V., Manakari, V., Parande, G., Gupta, M., & Wong, R. (2019). The potential of magnesium based materials in mandibular reconstruction. *Metals, 9*(3), 302.

Prendergast, P. J. (1997). Finite element models in tissue mechanics and orthopaedic implant design. *Clinical Biomechanics, 12*(6), 343-366.

PROLO, D. J., & RODRIGO, J. J. (1985). Contemporary bone graft physiology and surgery. *Clinical Orthopaedics and Related Research (1976-2007), 200*, 322-342.

Pugliese, R., & Graziosi, S. (2023). Biomimetic scaffolds using triply periodic minimal surface-based porous structures for biomedical applications. *SLAS technology*, *28*(3), 165-182.

Puppi, D., Chiellini, F., Piras, A. M., & Chiellini, E. (2010). Polymeric materials for bone and cartilage repair. *Progress in polymer Science, 35*(4), 403-440.

Qiu, N., Wan, Y., Shen, Y., & Fang, J. (2023). Experimental and numerical studies on mechanical properties of TPMS structures. *International Journal of Mechanical Sciences*, 108657.

Raggatt, L. J., & Partridge, N. C. (2010). Cellular and molecular mechanisms of bone remodelling. *Journal of biological chemistry*, *285*(33), 25103-25108.

Ramselaar, M. M. A., Driessens, F. C. M., Kalk, W., De Wijn, J. R., & Van Mullem, P. J. (1991). Biodegradation of four calcium phosphate ceramics; *in vivo* rates and tissue interactions. *Journal of Materials Science: Materials in Medicine*, *2*, 63-70.

Ratner, B. D. (2019). Biomaterials: been there, done that, and evolving into the future. *Annual review of biomedical engineering*, *21*, 171-191.

Ravi, M., Paramesh, V., Kaviya, S. R., Anuradha, E., & Solomon, F. P. (2015). 3D cell culture systems: advantages and applications. *Journal of cellular physiology*, *230*(1), 16-26.

Ribeiro, F. O., Gómez-Benito, M. J., Folgado, J., Fernandes, P. R., & García-Aznar, J. M. (2015). *In silico* mechano-chemical model of bone healing for the regeneration of critical defects: the effect of BMP-2. *PloS one, 10*(6), e0127722.

Ribes, A., & Caremoli, C. (2007, July). Salome platform component model for numerical simulation. In *31st annual international computer software and applications conference (COMPSAC 2007)* (Vol. 2, 553-564). IEEE.

Riddle, R. C., Taylor, A. F., Genetos, D. C., & Donahue, H. J. (2006). MAP kinase and calcium signalling mediate fluid flow-induced human mesenchymal stem cell proliferation. *American Journal of Physiology-Cell Physiology*, *290*(3), C776-C784.

Rider, P., Kačarević, Ž. P., Alkildani, S., Retnasingh, S., Schnettler, R., & Barbeck, M. (2018). Additive manufacturing for guided bone regeneration: A perspective for alveolar ridge augmentation. *International journal of molecular sciences*, *19*(11), 3308.

Robey, P.G. and Boskey, A.L., 2008. The composition of bone. *Primer on the metabolic bone diseases and disorders of mineral metabolism, 7*, 32-38.

Robinson, P. G., Abrams, G. D., Sherman, S. L., Safran, M. R., & Murray, I. R. (2020). Autologous bone grafting. *Operative Techniques in Sports Medicine*, *28*(4), 150780.

Robling, A. G., Castillo, A. B., & Turner, C. H. (2006). Biomechanical and molecular regulation of bone remodelling. *Annu. Rev. Biomed. Eng., 8*, 455-498.

Rodriguez, R. U., Kemper, N., Breathwaite, E., Dutta, S. M., Huber, A., Murchison, A., ... & Francis, M. P. (2016). Demineralized bone matrix fibers formable as general and custom 3D printed mold-based implants for promoting bone regeneration. *Biofabrication*, *8*(3), 035007.

Roosa, S. M. M., Kemppainen, J. M., Moffitt, E. N., Krebsbach, P. H., & Hollister, S. J. (2010). The pore size of polycaprolactone scaffolds has limited influence on bone regeneration in an *in vivo* model. *Journal of Biomedical Materials Research Part A: An Official Journal of The Society for Biomaterials, The Japanese Society for Biomaterials, and The Australian Society for Biomaterials and the Korean Society for Biomaterials*, *92*(1), 359-368.

Roseti, L., Parisi, V., Petretta, M., Cavallo, C., Desando, G., Bartolotti, I. and Grigolo, B., 2017. Scaffolds for bone tissue engineering: state of the art and new perspectives. *Materials Science and Engineering: C, 78,* 1246-1262.

Roseti, L., Parisi, V., Petretta, M., Cavallo, C., Desando, G., Bartolotti, I., & Grigolo, B. (2017). Scaffolds for bone tissue engineering: state of the art and new perspectives. *Materials Science and Engineering: C*, *78*, 1246-1262.

Rossi, G., Manfrin, A., & Lutolf, M. P. (2018). Progress and potential in organoid research. *Nature Reviews Genetics*, *19*(11), 671-687.

Rouahi, M., Champion, E., Gallet, O., Jada, A., & Anselme, K. (2006). Physico-chemical characteristics and protein adsorption potential of hydroxyapatite particles: influence on *in vitro* biocompatibility of ceramics after sintering. *Colloids and surfaces B: Biointerfaces*, *47*(1), 10-19.

Rubert, M., Vetsch, J. R., Lehtoviita, I., Sommer, M., Zhao, F., Studart, A. R., ... & Hofmann, S. (2021). Scaffold pore geometry guides gene regulation and bone-like tissue formation in dynamic cultures. *Tissue Engineering Part A*, *27*(17-18), 1192-1204.

Rumpler, M., Woesz, A., Dunlop, J. W., Van Dongen, J. T., & Fratzl, P. (2008). The effect of geometry on three-dimensional tissue growth. *Journal of the Royal Society Interface*, *5*(27), 1173-1180.

Sakkas, A., Wilde, F., Heufelder, M., Winter, K., & Schramm, A. (2017). Autogenous bone grafts in oral implantology—is it still a "gold standard"? A consecutive review of 279 patients with 456 clinical procedures. *International journal of implant dentistry*, *3*, 1-17.

Saleh, F. A., & Genever, P. G. (2011). Turning round: multipotent stromal cells, a three-dimensional revolution?. *Cytotherapy*, *13*(8), 903-912.

Salgado, A. J., Coutinho, O. P., Reis, R. L., & Davies, J. E. (2007). *In vivo* response to starch-based scaffolds designed for bone tissue engineering applications. *Journal of Biomedical Materials Research Part A*, *80*(4), 983-989.

Sanaei, P., Cummings, L. J., Waters, S. L., & Griffiths, I. M. (2019). Curvature- and fluid-stress-driven tissue growth in a tissue-engineering scaffold pore. *Biomechanics and modelling in mechanobiology, 18*, 589-605.

Sandino Velásquez, C. I. (2010). Simulation of mechanoregulation and tissue differentiation in calcium phosphate scaffolds for tissue engineering.

Sandino, C., & Lacroix, D. (2011). A dynamical study of the mechanical stimuli and tissue differentiation within a CaP scaffold based on micro-CT finite element models. *Biomechanics and modelling in mechanobiology*, *10*, 565-576.

Sandino, C., Checa, S., Prendergast, P. J., & Lacroix, D. (2010). Simulation of angiogenesis and cell differentiation in a CaP scaffold subjected to compressive strains using a lattice modelling approach. *Biomaterials*, *31*(8), 2446-2452.

Sandino, C., Checa, S., Prendergast, P. J., & Lacroix, D. (2010). Simulation of angiogenesis and cell differentiation in a CaP scaffold subjected to compressive strains using a lattice modelling approach. *Biomaterials*, *31*(8), 2446-2452.

Sanz-Herrera, J. A., Garcia-Aznar, J. M., & Doblare, M. (2008). A mathematical model for bone tissue regeneration inside a specific type of scaffold. *Biomechanics and modelling in mechanobiology, 7*(5), 355-366.

Sanz-Herrera, J. A., García-Aznar, J. M., & Doblaré, M. (2009). On scaffold designing for bone regeneration: a computational multiscale approach. *Acta Biomaterialia*, *5*(1), 219-229.

Sawada, K., Nakahara, K., Haga-Tsujimura, M., Iizuka, T., Fujioka-Kobayashi, M., Igarashi, K., & Saulacic, N. (2018). Comparison of three block bone substitutes for bone regeneration: long-term observation in the beagle dog. *Odontology*, *106*, 398-407.

Schamberger, B., Ziege, R., Anselme, K., Ben Amar, M., Bykowski, M., Castro, A. P., ... & Dunlop, J. W. (2023). Curvature in biological systems: its quantification, emergence, and implications across the scales. *advanced materials*, *35*(13), 2206110.

Schamberger, B., Ziege, R., Anselme, K., Ben Amar, M., Bykowski, M., Castro, A. P., ... & Dunlop, J. W. (2023). Curvature in Biological Systems: Its Quantification, Emergence, and Implications across the Scales. *Advanced Materials, 35*(13), 2206110.

Schieker, M., Seitz, H., Drosse, I., Seitz, S., & Mutschler, W. (2006). Biomaterials as scaffold for bone tissue engineering. *European journal of trauma*, *32*, 114-124.

Schilling, A. F., Linhart, W., Filke, S., Gebauer, M., Schinke, T., Rueger, J. M., & Amling, M. (2004). Resorbability of bone substitute biomaterials by human osteoclasts. *Biomaterials, 25*(18), 3963-3972.

Schmidt, A. H. (2021). Autologous bone graft: Is it still the gold standard?. *Injury*, *52*, S18-S22.

Schneider, C. A., Rasband, W. S., & Eliceiri, K. W. (2012). NIH Image to ImageJ: 25 years of image analysis. *Nature methods*, *9*(7), 671-675.

Serrano-Bello, J., Cruz-Maya, I., Suaste-Olmos, F., González-Alva, P., Altobelli, R., Ambrosio, L., ... & Alvarez-Perez, M. A. (2020). *In vivo* regeneration of mineralized bone tissue in anisotropic biomimetic sponges. *Frontiers in Bioengineering and Biotechnology*, *8*, 587.

Setiawati, R. and Rahardjo, P., 2019. Bone development and growth. *Osteogenesis and bone regeneration, 10.*

Shahlaie, M., Gantes, B., Schulz, E., Riggs, M., & Crigger, M. (2003). Bone density assessments of dental implant sites: 1. Quantitative computed tomography. *International Journal of Oral & Maxillofacial Implants*, *18*(2).

Sheikh, Z., Hamdan, N., Ikeda, Y., Grynpas, M., Ganss, B., & Glogauer, M. (2017). Natural graft tissues and synthetic biomaterials for periodontal and alveolar bone reconstructive applications: a review. *Biomaterials research*, *21*(1), 9.

Solheim, E., 1998. Growth factors in bone. *International orthopaedics, 22(*6), 410-416.

Son, C., Choi, M. S., & Park, J. C. (2020). Different Responsiveness of Alveolar Bone and Long Bone to Epithelial Mesenchymal Interaction Related Factor. *Journal of Bone and Mineral Research Plus*, *4*(8), e10382.

Spin-Neto, R., Stavropoulos, A., Coletti, F. L., Pereira, L. A., Marcantonio Jr, E., & Wenzel, A. (2015). Remodelling of cortical and corticocancellous fresh-frozen allogeneic block bone grafts—a radiographic and histomorphometric

comparison to autologous bone grafts. *Clinical oral implants research*, *26*(7), 747-752.

Stewart, S. K. (2019). Fracture non-union: a review of clinical challenges and future research needs. *Malaysian orthopaedic journal*, *13*(2), 1.

Sun, J., & Tan, H. (2013). Alginate-based biomaterials for regenerative medicine applications. *Materials, 6*(4), 1285-1309.

Sun, X., Kang, Y., Bao, J., Zhang, Y., Yang, Y., & Zhou, X. (2013). Modelling vascularized bone regeneration within a porous biodegradable CaP scaffold loaded with growth factors. *Biomaterials*, *34*(21), 4971-4981.

Tavoni, M., Dapporto, M., Tampieri, A., & Sprio, S. (2021). Bioactive calcium phosphate-based composites for bone regeneration. *Journal of Composites Science*, *5*(9), 227.

Tayalia, P. and Mooney, D.J., 2009. Controlled growth factor delivery for tissue engineering. *Advanced materials, 21*(32- 33), 3269-3285.

Tortora, G.J. and Derrickson, B.H., 2018. *Principles of anatomy and physiology*. John Wiley & Sons.

Tuan, H. S., & Hutmacher, D. W. (2005). Application of micro CT and computation modelling in bone tissue engineering. *Computer-Aided Design*, *37*(11), 1151-1161.

Urban, I.A. and Monje, A., 2019. Guided Bone Regeneration in Alveolar Bone Reconstruction. *Oral and maxillofacial surgery clinics of North America, 31*(2), 331-338.

U.S. Food and Drug Administration. (2021). *Technical Considerations for Additive Manufactured Medical Devices*. Retrieved from https://www.fda.gov/media/154985/download

Vacanti, J. P., & Langer, R. (1999). Tissue engineering: the design and fabrication of living replacement devices for surgical reconstruction and transplantation. *The lancet, 354*, S32-S34.

Van Bael, S., Chai, Y. C., Truscello, S., Moesen, M., Kerckhofs, G., Van Oosterwyck, H., ... & Schrooten, J. J. A. B. (2012). The effect of pore geometry on the *in vitro* biological behaviour of human periosteum-derived cells seeded on selective laser-melted Ti6Al4V bone scaffolds. *Acta biomaterialia*, *8*(7), 2824-2834.

Van Bael, S., Chai, Y. C., Truscello, S., Moesen, M., Kerckhofs, G., Van Oosterwyck, H., ... & Schrooten, J. J. A. B. (2012). The effect of pore geometry on the *in vitro* biological behaviour of human periosteum-derived cells seeded on selective laser-melted Ti6Al4V bone scaffolds. *Acta biomaterialia*, *8*(7), 2824-2834.

Van Hede, D., Liang, B., Anania, S., Barzegari, M., Verlée, B., Nolens, G., ... & Lambert, F. (2022). 3D-printed synthetic hydroxyapatite scaffold with *in silico* optimized macrostructure enhances bone formation *in vivo*. *Advanced Functional Materials*, *32*(6), 2105002.

Velard, F., Braux, J., Amedee, J., & Laquerriere, P. (2013). Inflammatory cell response to calcium phosphate biomaterial particles: an overview. *Acta biomaterialia*, *9*(2), 4956-4963.

Venet, L., Perriat, M., Mangano, F. G., & Fortin, T. (2017). Horizontal ridge reconstruction of the anterior maxilla using customized allogeneic bone blocks with a minimally invasive technique-a case series. *BMC Oral Health*, *17*, 1-8.

Vijayavenkataraman, S., Zhang, L., Zhang, S., Hsi Fuh, J. Y., & Lu, W. F. (2018). Triply periodic minimal surfaces sheet scaffolds for tissue engineering applications: An optimization approach toward biomimetic scaffold design. *ACS Applied Bio Materials, 1*(2), 259-269.

Wakitani, S., Goto, T., Pineda, S.J., Young, R.G., Mansour, J.M., Caplan, A.I. and Goldberg, V.M., 1994. Mesenchymal cell-based repair of large, full-thickness defects of articular cartilage. *The Journal of bone and joint surgery. American volume, 76*(4), 579-592.

Wang, M., Yang, N., & Wang, X. (2017). A review of computational models of bone fracture healing. *Medical & biological engineering & computing*, *55*, 1895-1914.

Waters, S. L., Schumacher, L. J., & El Haj, A. J. (2021). Regenerative medicine meets mathematical modelling: developing symbiotic relationships. *npj Regenerative Medicine, 6*(1), 24.

Webster, D., & Müller, R. (2011). *In silico* models of bone remodelling from macro to nano—from organ to cell. *Wiley Interdisciplinary Reviews: Systems Biology and Medicine, 3*(2), 241-251.

Werner, M., Blanquer, S. B., Haimi, S. P., Korus, G., Dunlop, J. W., Duda, G. N., ... & Petersen, A. (2017). Surface curvature differentially regulates stem cell migration and differentiation via altered attachment morphology and nuclear deformation. *Advanced science*, *4*(2), 1600347.

Werner, M., Blanquer, S. B., Haimi, S. P., Korus, G., Dunlop, J. W., Duda, G. N., ... & Petersen, A. (2017). Surface curvature differentially regulates stem cell migration and differentiation via altered attachment morphology and nuclear deformation. *Advanced science, 4*(2), 1600347.

Whitaker, M.J., Quirk, R.A., Howdle, S.M. and Shakesheff, K.M., 2001. Growth factor release from tissue engineering scaffolds. *Journal of Pharmacy and Pharmacology, 53*(11), 1427-1437.

Wickham, M.Q., Erickson, G.R., Gimble, J.M., Vail, T.P. and Guilak, F., 2003. Multipotent stromal cells derived from the infrapatellar fat pad of the knee. *Clinical Orthopaedics and Related Research®, 412*, 196-212.

Wilk-Blaszczak, M., 2018. Lab 2: Bones and Bone Markings. *Human Anatomy Lab Manual.*

Williams, D. F. (2008). On the mechanisms of biocompatibility. *Biomaterials, 29*(20), 2941-2953.

Winning, L., Robinson, L., Boyd, A. R., El Karim, I. A., Lundy, F. T., & Meenan, B. J. (2017). Osteoblastic differentiation of periodontal ligament stem cells on non-stoichiometric calcium phosphate and titanium surfaces. *Journal of biomedical materials research Part A*, *105*(6), 1692-1702.

Xu, X., Farach-Carson, M. C., & Jia, X. (2014). Three-dimensional *in vitro* tumor models for cancer research and drug evaluation. *Biotechnology advances*, *32*(7), 1256-1268.

Xiao, Y., Liang, Q., Zhou, L., He, X., Lv, L., Chen, J., ... & Lin, L. (2022). Construction of a new automatic grading system for jaw bone mineral density level based on deep learning using cone beam computed tomography. *Scientific reports*, *12*(1), 12841.

Yang, K., Han, Q., Chen, B., Zheng, Y., Zhang, K., Li, Q. and Wang, J., 2018. Antimicrobial hydrogels: promising materials for medical application. *International journal of nanomedicine, 13*, p.2217.

Yang, Y., Xu, T., Bei, H. P., Zhang, L., Tang, C. Y., Zhang, M., ... & Zhao, X. (2022). Gaussian curvature–driven direction of cell fate toward osteogenesis with triply periodic minimal surface scaffolds. *Proceedings of the National Academy of Sciences*, *119*(41), e2206684119.

Yazdanpanah, Z., Johnston, J. D., Cooper, D. M., & Chen, X. (2022). 3D bioprinted scaffolds for bone tissue engineering: State-of-the-art and

emerging technologies. *Frontiers in bioengineering and biotechnology*, *10*, 824156.

Young, H. E., Steele, T. A., Bray, R. A., Hudson, J., Floyd, J. A., Hawkins, K., ... & Black Jr, A. C. (2001). Human reserve pluripotent mesenchymal stem cells are present in the connective tissues of skeletal muscle and dermis derived from fetal, adult, and geriatric donors. *The Anatomical Record: An Official Publication of the American Association of Anatomists*, *264*(1), 51-62.

Zadpoor, A. A. (2015). Bone tissue regeneration: the role of scaffold geometry. *Biomaterials science*, *3*(2), 231-245.

Zamani, Y., Amoabediny, G., Mohammadi, J., Seddiqi, H., Helder, M. N., Zandieh-Doulabi, B., ... & Koolstra, J. H. (2020). 3D-printed poly (Ɛ-caprolactone) scaffold with gradient mechanical properties according to force distribution in the mandible for mandibular bone tissue engineering. *Journal of the mechanical behaviour of biomedical materials*, *104*, 103638.

Zhang, L., Qiao, M., Gao, H., Hu, B., Tan, H., Zhou, X., & Li, C. M. (2016). Investigation of mechanism of bone regeneration in a porous biodegradable calcium phosphate (CaP) scaffold by a combination of a multi-scale agent-based model and experimental optimization/validation. *Nanoscale, 8*(31), 14877-14887.

Zhen, W., Jiang, C., Feng, B., Xiaojiang, S., Jianxi, L., Li, L., ... & Rong, D. (2010). Role of the porous structure of the bioceramic scaffolds in bone tissue engineering. *Nature Precedings*, 1-1.

Zhu, Z., Ng, D. W. H., Park, H. S., & McAlpine, M. C. (2021). 3D-printed multifunctional materials enabled by artificial-intelligence-assisted fabrication technologies. *Nature Reviews Materials*, *6*(1), 27-47.

Appendices

A. Convergence (Chapter 3)

Convergence testing is the process of determining whether the mesh density used in a numerical simulation is sufficiently detailed to ensure that further mesh refinement will not significantly change the simulation results. Very high-density meshes require substantial computing resources, so often a trade-off is made between accuracy and computational cost based on the results of the convergence test.

In the convergence test of this model, we set the model to reach convergence when the relative error in results after 2 days of running is less than 6%. The relative error is calculated as $|N2 - N1|/N2$, with $N1$ and $N2$ being increasing mesh sizes in the convergence test. Here, we used a gyroid scaffold of 6mm diameter and height, with 1mm pore size and 0.2mm wall thickness. According to the results in Figure A.1 and Table A.1, when the mesh size is greater than 130,000 elements, the model has reached convergence. In all 3D structures used in this thesis, a similar or higher mesh density was applied.
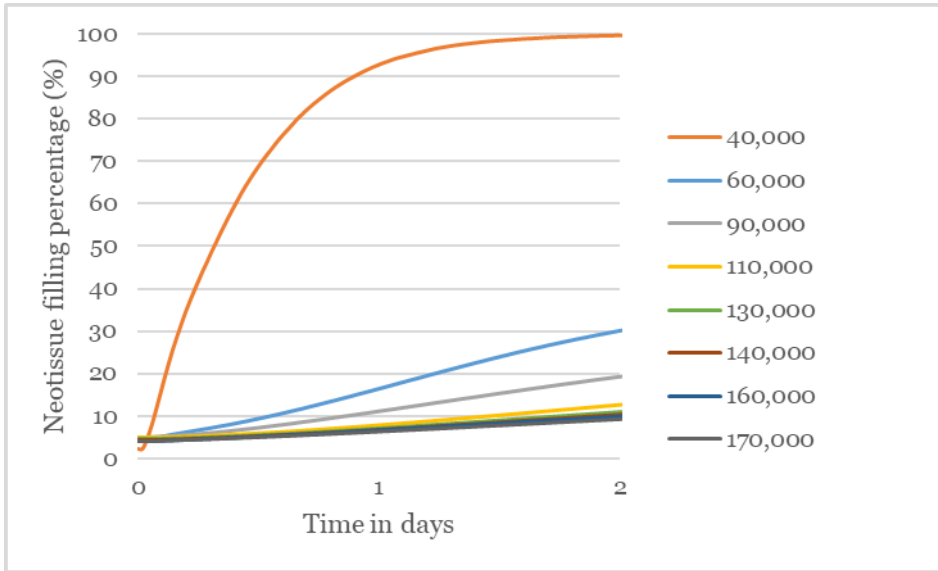
Figure A1. Convergence analysis. The graph shows the neotissue formation (expressed in % of free volume filled) calculated after 2 days, for different sizes of the mesh. The legends shows the number of elements used to mesh a 3D cylindrical gyroid scaffold of 6mm height and diameter, 1mm pore size and 0.2mm wall thickness.

Number of elements	Neotissue filling (%) after 2 days	Relative Error (%)
40,000	99,52	228,23
60,000	30,32	55,97
90,000	19,44	52,23
110,000	12,77	15,99
130,000	11,01	6,07
140,000	10,38	4,43
160,000	9.94	5,19
170,000	9,45	

Table A1. Relative error results for different mesh sizes used in the convergence test.

B. Raw numbers of *in vitro* study (Chapter 3)

[%]	S1	S2	S3	average	S1	S2	S3	average	S1	S2	S3	average	S1	S2	S3	average
	HAp-C500				HAp-C700				HAp-C1000							
day 10	43	35	38	38,67	37	31	33	33,67	34	35	25	31,33				
day 21	97	91	100	96,00	97	95	93	95,00	86	75	67	76,00				
	HAp-H500				HAp-H700				HAp-H1000							
day 10	62	66	76	68,00	24	20	23	22,33	18	24	18	20,00				
day 21	100	96	100	98,67	93	90	91	91,33	75	81	85	80,33				
					HAp-S700				HAp-S1000				HAp-S2000			
day 10					51	39	42	44,00	19	25	22	22,00	5	5	6	5,33
day 21					96	91	89	92,00	53	67	35	51,67	15	11	11	12,33
					HAp-T700				HAp-T1000				HAp-T2000			
day 10					59	46	51	52,00	49	41	50	46,67	26	23	17	22,00
day 21					93	100	93	95,33	98	100	100	99,33	34	18	29	27,00
	TCP-C500				TCP-C700				TCP-C1000							
day 10	63	69	68	66,67	53	44	57	51,33	30	24	26	26,67				
day 21	93	93	92	92,67	69	68	92	76,33	32	70	35	45,67				
	TCP-H500				TCP-H700				TCP-H1000							
day 10	63	87	73	74,33	57	53	55	55,00	26	33	27	28,67				
day 21	96	100	100	98,67	86	92	88	88,67	90	73	85	82,67				
					TCP-S700				TCP-S1000				TCP-S2000			
day 10					40	50	44	44,67	36	32	32	33,33	7	5	5	5,67
day 21					85	94	84	87,67	41	82	56	59,67	21	27	23	23,67
					TCP-T700				TCP-T1000				TCP-T2000			
day 10					36	49	57	47,33	35	50	50	45,00	20	22	25	22,33
day 21					92	100	90	94,00	88	88	92	89,33	35	36	39	36,67
	BCP-C500				BCP-C700				BCP-C1000							
day 10	46	30	34	36,67	12	9	11	10,67	10	11	10	10,33				
day 21	63	65	65	64,33	33	43	38	38,00	41	37	25	34,33				
	BCP-H500				BCP-H700				BCP-H1000							
day 10	45	52	50	49,00	21	22	17	20,00	13	14	19	15,33				
day 21	65	80	63	69,33	69	49	63	60,33	26	27	27	26,67				
					BCP-S700				BCP-S1000				BCP-S2000			
day 10					20	16	13	16,33	17	20	10	15,67	3	9	4	5,33
day 21					79	44	66	63,00	42	60	45	49,00	13	11	9	11,00
					BCP-T700				BCP-T1000				BCP-T2000			
day 10					57	41	45	47,67	23	27	31	27,00	9	10	14	11,00
day 21					85	65	84	78,00	84	78	85	82,33	21	16	15	17,33
[%]	S1	S2	S3	average	S1	S2	S3	average	S1	S2	S3	average	S1	S2	S3	average
	HAp-C500				HAp-C700				HAp-C1000							

day 10	43 35 38 *38,67*	37 31 33 *33,67*	34 35 25 *31,33*	
day 21	97 91 100 *96,00*	97 95 93 *95,00*	86 75 67 *76,00*	
	HAp-H500	**HAp-H700**	**HAp-H1000**	
day 10	62 66 76 *68,00*	24 20 23 *22,33*	18 24 18 *20,00*	
day 21	100 96 100 *98,67*	93 90 91 *91,33*	75 81 85 *80,33*	
		HAp-S700	**HAp-S1000**	**HAp-S2000**
day 10		51 39 42 *44,00*	19 25 22 *22,00*	5 5 6 *5,33*
day 21		96 91 89 *92,00*	53 67 35 *51,67*	15 11 11 *12,33*
		HAp-T700	**HAp-T1000**	**HAp-T2000**
day 10		59 46 51 *52,00*	49 41 50 *46,67*	26 23 17 *22,00*
day 21		93 100 93 *95,33*	98 100 100 *99,33*	34 18 29 *27,00*
	TCP-C500	**TCP-C700**	**TCP-C1000**	
day 10	63 69 68 *66,67*	53 44 57 *51,33*	30 24 26 *26,67*	
day 21	93 93 92 *92,67*	69 68 92 *76,33*	32 70 35 *45,67*	
	TCP-H500	**TCP-H700**	**TCP-H1000**	
day 10	63 87 73 *74,33*	57 53 55 *55,00*	26 33 27 *28,67*	
day 21	96 100 100 *98,67*	86 92 88 *88,67*	90 73 85 *82,67*	
		TCP-S700	**TCP-S1000**	**TCP-S2000**
day 10		40 50 44 *44,67*	36 32 32 *33,33*	7 5 5 *5,67*
day 21		85 94 84 *87,67*	41 82 56 *59,67*	21 27 23 *23,67*
		TCP-T700	**TCP-T1000**	**TCP-T2000**
day 10		36 49 57 *47,33*	35 50 50 *45,00*	20 22 25 *22,33*
day 21		92 100 90 *94,00*	88 88 92 *89,33*	35 36 39 *36,67*
	BCP-C500	**BCP-C700**	**BCP-C1000**	
day 10	46 30 34 *36,67*	12 9 11 *10,67*	10 11 10 *10,33*	
day 21	63 65 65 *64,33*	33 43 38 *38,00*	41 37 25 *34,33*	
	BCP-H500	**BCP-H700**	**BCP-H1000**	
day 10	45 52 50 *49,00*	21 22 17 *20,00*	13 14 19 *15,33*	
day 21	65 80 63 *69,33*	69 49 63 *60,33*	26 27 27 *26,67*	
		BCP-S700	**BCP-S1000**	**BCP-S2000**
day 10		20 16 13 *16,33*	17 20 10 *15,67*	3 9 4 *5,33*
day 21		79 44 66 *63,00*	42 60 45 *49,00*	13 11 9 *11,00*
		BCP-T700	**BCP-T1000**	**BCP-T2000**
day 10		57 41 45 *47,67*	23 27 31 *27,00*	9 10 14 *11,00*
day 21		85 65 84 *78,00*	84 78 85 *82,33*	21 16 15 *17,33*

Table B1. Raw numbers and averages of the neotissue filling percentages for the different time points (10 & 21), materials (HAp, TCP, BCP), channel shapes (C: circle; H: hexagon; S: square; T: triangle) and channel sizes (500: 0.5mm; 700: 0.7mm; 1000: 1mm; 2000: 2mm).

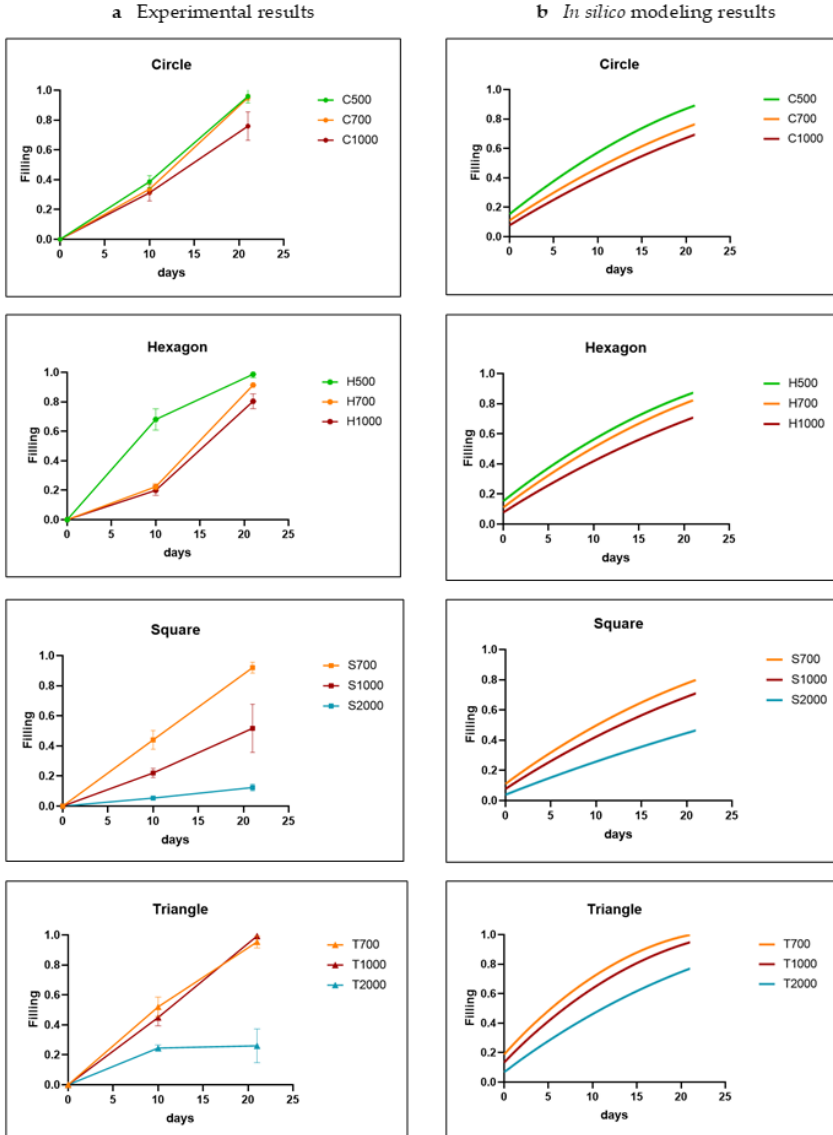# C. Comparison between experimental results and *in silico* results for TCP disks (Chapter 3)

Figure C1. Comparison between experimental results (a) and *in silico* results (b) for all channel shapes for TCP disks. The parameter A was fixed at 0.01 during Bayesian optimisation). The shapes are labelled by a letter (T: Triangle, S: Square, H: hexagon; C: circle) and a number indicating the channel diameter in micrometer. The experimental data are shown as mean ± SD.
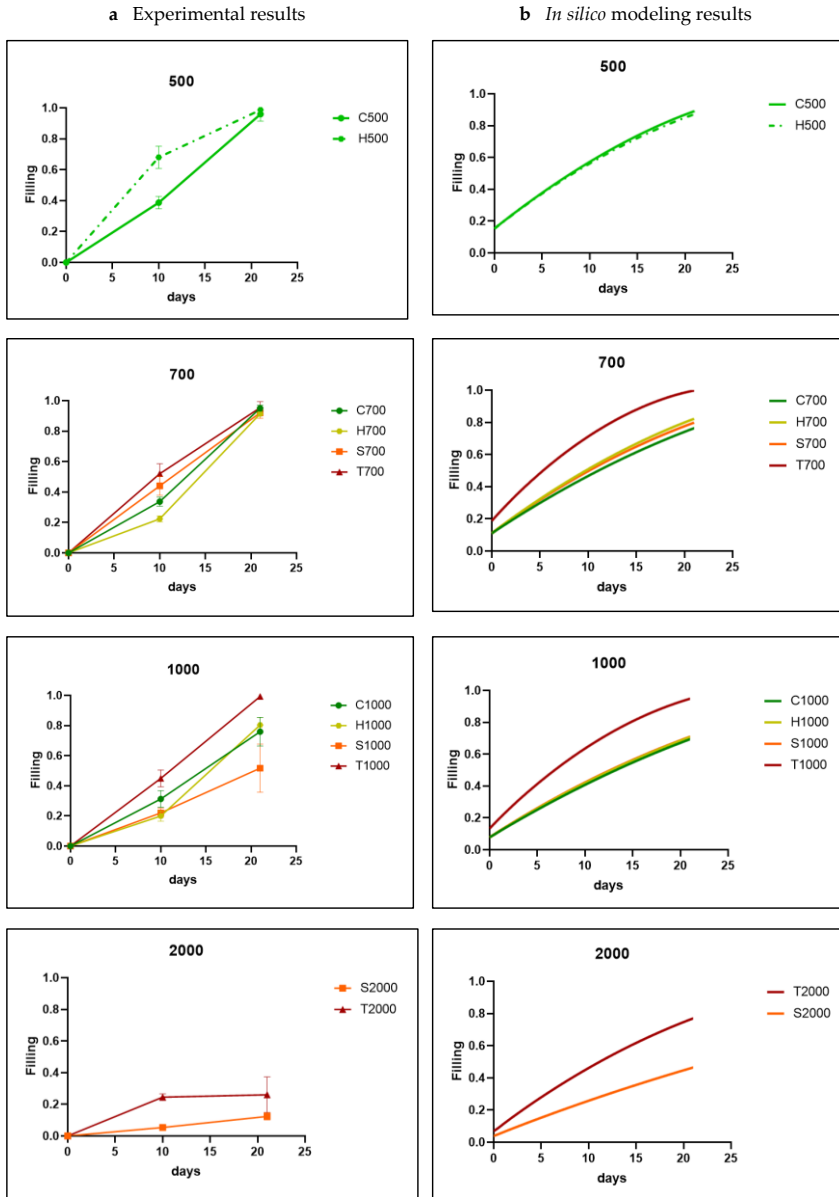
Figure C2. Comparison between experimental results (a) and *in silico* results (b) for all channel sizes for TCP disks. The parameter A was fixed at 0.01 during Bayesian optimisation). The shapes are labelled by a letter (T: Triangle, S: Square, H: hexagon; C: circle) and a number indicating the channel diameter in micrometer. The experimental data are shown as mean ± SD.
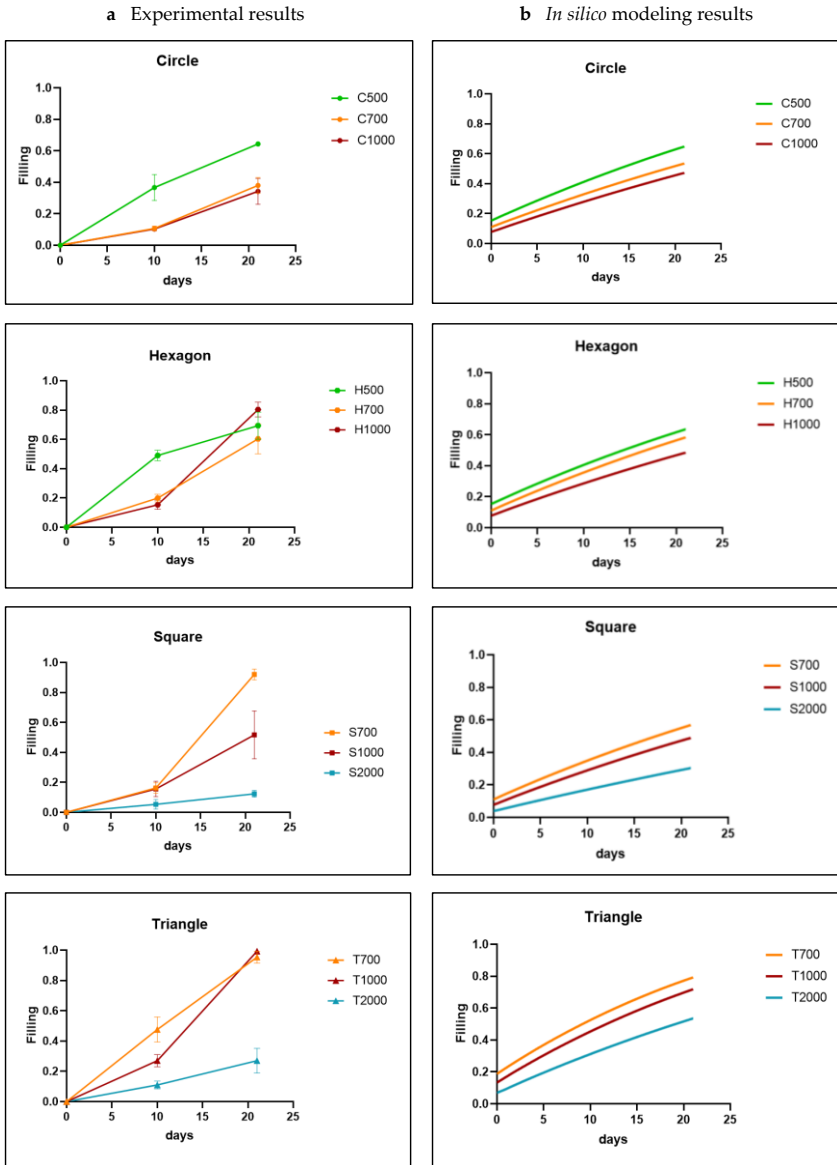
Figure C3. Comparison between experimental results (a) and *in silico* results (b) for all channel sizes for BCP disks. The parameter A was fixed at 0.001 during Bayesian optimisation). The shapes are labelled by a letter (T: Triangle, S: Square, H: hexagon; C: circle) and a number indicating the channel diameter in micrometer. The experimental data are shown as mean ± SD.
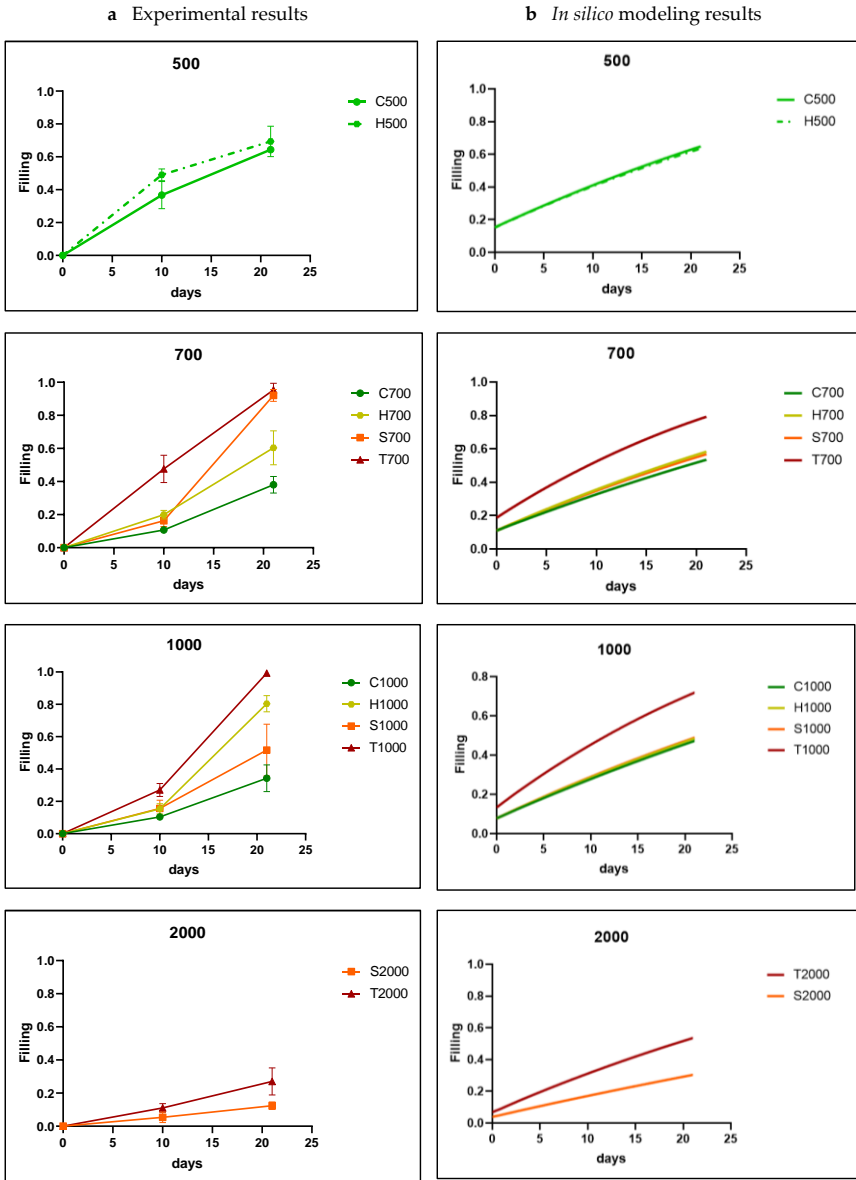
Figure C4. Comparison between experimental results (a) and *in silico* results (b) for all channel sizes for BCP disks. The parameter A was fixed at 0.001 during Bayesian optimisation). The shapes are labelled by a letter (T: Triangle, S: Square, H: hexagon; C: circle) and a number indicating the channel diameter in micrometer. The experimental data are shown as mean ± SD.

D. Additional physico-chemical characterization (Chapter 4)

In addition to the XRD and SEM analyses, several physico-chemical characterizations were conducted.

Compression strength test was performed on Orthogonal and Gyroid 3D-printed scaffolds (n=6 for each) following the ISO 13175 (ShimadzuAG-XPlus/100kN) and showed compressive strengths of 22.73 ± 1.9 and 6.26 ± 0.99 MPa respectively. Although the compressive strength of the Gyroid design was highly reduced compared to the Orthogonal design, its remains in the compressive strength range observed for spongy bone (1.9 – 7.0 MPa).

The specific surface area was measured by N2 adsorption according to the Brunauer–Emmett–Teller (BET) method on an ASAP2020 PLUS equipment (Micromeritics, Norcross, GA, USA). Prior to the measurements, the samples were degassed 3 hours under vacuum at 150 °C. Optimization and data selection were processed according to the BET surface area Rouquerol's criteria. The 3D-printed Orthogonal and Gyroid scaffolds obtained similar value (0.75 ± 0.04 and 0.77 ± 0.04 m2/g) whereas the Granules sample displayed a specific surface area of 81.5 ±0.04. These results indicated that the 3D-printed scaffolds are dense materials with less microporosities compared to the Granules.

Finally, a degradation test, adapted from the ISO 10993-14, was performed by immersing the different materials in Tris-HCl buffer (pH of 7.4) at 37°C for 1 (n=3), 2 (n=3) and 3 (n=3) weeks and under constant agitation. Materials were weighted before the experiment and after each time point after being dried (6 hrs at 100°C). For all materials, weight loss was minor (less than 0.3 % in average for all time points) as expected since the solubility of hydroxyapatite is known to be very low in physiological environments (Ramselaar et al., 1991).

E. Additional methodologies and output measures for newly formed bone quantification (Chapter 4)

In addition to the calculation of the bone volume inside the VOI1 (Total volume inside the shells), the percentage of bone volume inside the VOI2 (the empty volume inside the shells) were obtained as follows:

$$\text{Bone within VOI2 (\%)} = \frac{\text{Volume of Bone}}{\text{VOI2}} \times 100 \tag{E1}$$

However, as the VOI2 were not equivalent between the three groups (Table E1), the bone volume was finally normalized using the VOI2 of the Granules as a reference:

$$\text{Bone within Normalized VOI2 (\%)} = \frac{\text{Volume of Bone}}{\text{VOI2}} \times \frac{\text{VOI2 granules}}{\text{VOI2 Insert}} \times 100 \tag{E2}$$

The corresponding results are presented in Figure E1 and Table E1.
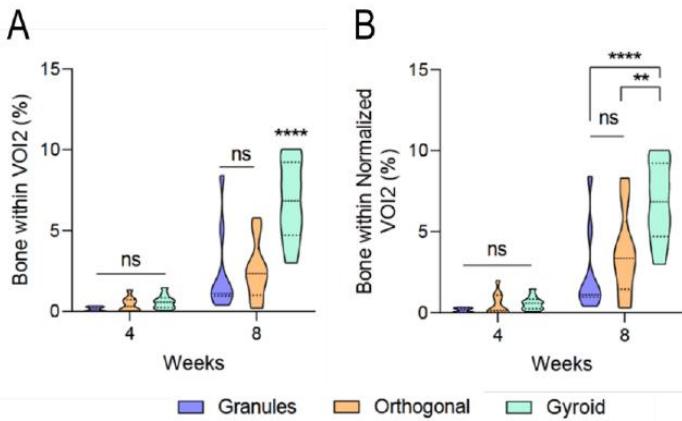

Figure E1. Bone regeneration analysis by Nano-CT. The percentages of newly formed bone between the Granules, the Orthogonal and the Gyroid groups were determined within the VOI2 (A, Equation (E1)) and the normalized VOI2 (B, Equation (E2)) at 4 and 8 weeks. ns = not significant; * = p < 0.05; ** = p< 0.01; **** = p < 0.0001.

PARAMETER	TIME POINT (WEEKS)	GROUP			P-VALUE BETWEEN GROUPS
		Granules	Orthogonal	Gyroid	
Biomaterial Volume (%)	4	39 ± 2.13 *	59.27 ± 1.49	38.72 ± 1.11	Orthogonal : p < 0.0001
Empty Volume (%)	4	61 ± 2.13 *	40.73 ± 1.49	61.28 ± 1.11	Orthogonal : p < 0.0001
Bone within VOI1 (% ± SD)	4	0.1 ± 0.08	0.18 ± 0.19	0.37 ± 0.26	ns
	8	1.45 ± 1.62	1.08 ± 0.79	4.16 ± 1.48	Gyroid : p < 0.0001
	p-values between Time points	p < 0.05	ns	p < 0.0001	-
Bone within VOI2 (% ± SD) Equation (1)	4	0.17 ± 0.13	0.44 ± 0.47	0.60 ± 0.43	ns
	8	2.38 ± 2.65	2.55 ± 1.86	6.83 ± 2.43	Gyroid : p < 0.0001
	p-values between Time points	p < 0.05	p < 0.05	p < 0.0001	-
Bone within Normalized VOI2 (% ± SD) Equation (2)	4	0.27 ± 0.21	1.06 ± 1.14	0.98 ± 0.71	ns
	8	3.90 ± 4.35	6.01 ± 4.38	11.22 ± 4.00	Gyroid vs Granules: p < 0.0001 Gyroid vs Orthogonal : p < 0.01
	p-values between Time points	p < 0.05	p < 0.01	p < 0.0001	-
Highest point of Bone (% ± SD)	4	5.52 ± 4.54	21.72 ± 3.92	15.71 ± 9.2	p < 0.05 between Granules and Orthogonal
	8	15.6 ± 5.67	31.83 ± 14.57	75.69 ± 23.29	p < 0.05 between Granules and Orthogonal p < 0.0001 for Gyroid
	p-values between Time points	ns	ns	p < 0.0001	-

Table E1. Data obtained from the Nano-CT analysis and their statistical significance. Statistical analysis was performed to compare values between groups for each time point and to compare values between time points for each group. * mean values obtained from 4 samples at 4 weeks without bone regeneration; values presented as mean ± standard deviation; ns = not significant.
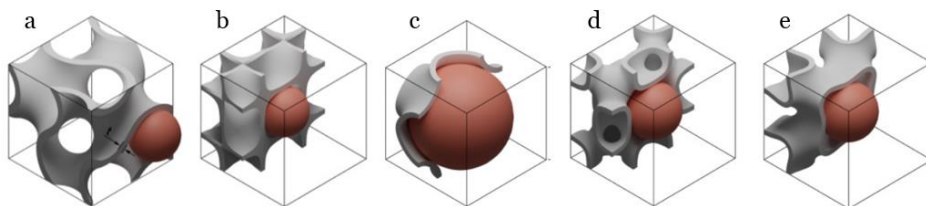
F. Pore size measurement (Chapter 5)

Figure F1. shows the pore size measurement of TPMs structure. The correlation between porosity, pore size and surface area is provided by Poltue et al (a. Gyroid; b. Diamond ; c. Primitive; d. F-RD; e. IWP).

Curriculum Vitae

Personal data

Name: Bingbing Liang

Date of birth: 2nd November 1991

Place of birth: Shandong, China

Address: Dublin, Ireland

Tel: +32 497 11 69 01

Email: bingbingliang1102@gmail.com

Education

2017 – 2024: PhD

      University of Liège, Liège, Belgium

      Department of Aerospace and Mechanical Engineering

      Biomechanics Research Unit

2015 – 2016: Master of Science (MSc) in Mechanical Engineering

      Newcastle University, Newcastle, UK

      Faculty of Science, Agriculture and Engineering

2011 – 2014: Bachelor of Mechanical Design, Manufacturing, and Automation

      Central South University of Forestry and Technology, Hunan, China

      School of Mechanical and Electrical Engineering

List of publications

Bingbing Liang, Ehsan Sadeghian Dehkord, Dorien Van Hede, Mojtaba Barzegari, Bruno Verlée , Justine Pirson, Grégory Nolens, France Lambert*, Liesbet Geris*. Model-Based Design to Enhance Neotissue Formation in Additively Manufactured Calcium Phosphate-based Scaffolds. Journal of Functional Biomaterials, 2023 Dec 3;14(12):563. doi: 10.3390/jfb14120563

Dorien Van Hede, Bingbing Liang, Sandy Anania, Mojtaba Barzegari, Bruno Verlée, Grégory Nolens, Justine Pirson, Liesbet Geris*, and France Lambert*. 3D-Printed Synthetic Hydroxyapatite Scaffold With *In silico* Optimized Macrostructure Enhances Bone Formation *In vivo*, 2022, 32(6): 2105002. Doi: 10.1002/adfm.202105002

Scientific conferences

- 6th world congress of the Tissue Engineering and Regenerative Medicine International Society (TERMIS), Maastricht, Netherlands, 2021

  Abstract title: Optimisation of bone formation in 3D-printed Calcium Phosphate scaffolds for dental applications: from *in silico* design to *in vivo* validation

  Bingbing Liang, Dorien Van Hede, Ehsan Sadeghian, France Lambert, Liesbet Geris

- 11th World Biomaterial Congress Virtual (WBC), 2020

  Abstract title: *In silico* design and *in vivo* validation of bone formation in 3D-printed Calcium Phosphate scaffolds for dental applications

  Bingbing Liang, Dorien Van Hede, Ehsan Sadeghian, France Lambert, Liesbet Geris

- Belgian symposium on tissue engineering, Hasselt, Belgium, 2019

Abstract title : Model-based design of 3D-printed Calcium Phosphate based biomaterials for dental applications

<u>Bingbing Liang</u>, Ehsan Sadeghian, Dorien Van Hede, France Lambert, Liesbet Geris

- ESBiomech Conference, Vienna, Austria, 2019

Abstract title: *In silico* design of 3D-printed Calcium Phosphate based dental biomaterials

<u>Bingbing Liang</u>, Ehsan Sadeghian, Dorien Van Hede, France Lambert, Liesbet Geris

- National day on biomedical engineering, Brussels, Belgium, 2018

Abstract title: Model assisted design of 3D printed Calcium phosphate for optimized bone regeneration

<u>Bingbing Liang</u>, Varun Manhas, Liesbet Geris

- Virtual Physiological Human Conference- VPH for *In silico* Medicine, Zaragoza, Spain, 2018

Abstract title: Model-based design of 3D-printed Calcium Phosphate based biomaterials for dental applications

<u>Bingbing Liang</u>, Varun Manhas, Liesbet Geris

Scientific award

HANDS-ON AWARD of the 3rd VPH summer school, 2018

Presentation title: Model assisted design of 3D printed biomaterials for optimized bone regeneration in alveolar bone

<u>Bingbing Liang</u>, Varun Manhas, Dorien Van Hede, France Lambert, Liesbet Geris